



Konda, Pavan Chandra (2018) Multi-Aperture Fourier Ptychographic Microscopy: development of a high-speed gigapixel coherent computational microscope. PhD thesis.

<http://theses.gla.ac.uk/9015/>

Copyright and moral rights for this work are retained by the author

A copy can be downloaded for personal non-commercial research or study, without prior permission or charge

This work cannot be reproduced or quoted extensively from without first obtaining permission in writing from the author

The content must not be changed in any way or sold commercially in any format or medium without the formal permission of the author

When referring to this work, full bibliographic details including the author, title, awarding institution and date of the thesis must be given

Enlighten:Theses
<http://theses.gla.ac.uk/>
theses@gla.ac.uk

Multi-Aperture Fourier Ptychographic Microscopy: Development of a high-speed gigapixel coherent computational microscope

Pavan Chandra Konda

Submitted in fulfilment of the requirements for the degree of *Doctor of
Philosophy*



University of Glasgow

School of Physics and Astronomy
College of Science and Engineering

October 2017

Abstract

Medical research and clinical diagnostics require imaging of large sample areas with sub-cellular resolution. Conventional imaging techniques can provide either high-resolution or wide field-of-view (FoV) but not both. This compromise is conventionally defeated by using a high NA objective with a small FoV and then mechanically scan the sample in order to acquire separate images of its different regions. By stitching these images together, a larger effective FoV is then obtained. This procedure, however, requires precise and expensive scanning stages and prolongs the acquisition time, thus rendering the observation of fast processes/phenomena impossible. A novel imaging configuration termed Multi-Aperture Fourier Ptychographic Microscopy (MA-FPM) is proposed here based on Fourier ptychography (FP), a technique to achieve wide-FoV and high-resolution using time-sequential synthesis of a high-NA coherent illumination. MA-FPM configuration utilises an array of objective lenses coupled with detectors to increase the bandwidth of the object spatial-frequencies captured in a single snapshot. This provides high-speed data-acquisition with wide FoV, high-resolution, long working distance and extended depth-of-field.

In this work, a new reconstruction method based on Fresnel diffraction forward model was developed to extend FP reconstruction to the proposed MA-FPM technique. MA-FPM was validated experimentally by synthesis of a 3x3 lens array system from a translating objective-detector system. Additionally, a calibration procedure was also developed to register dissimilar images from multiple cameras and successfully implemented on the experimental data. A nine-fold improvement in captured data-bandwidth was demonstrated.

Another experimental configuration was proposed using the Scheimpflug condition to correct for the aberrations present in the off-axis imaging systems. An experimental setup was built for this new configuration using 3D printed parts to minimise the cost. The design of this setup is discussed along with robustness analysis of the low-cost detectors used in this setup. A reconstruction model for the Scheimpflug configuration FP was developed and applied to the experimental

data. Preliminary experimental results were found to be in agreement with this reconstruction model. Some artefacts were observed in these results due to the calibration errors in the experiment. These can be corrected by using the self-calibration algorithm proposed in the literature, which is left as a future work. Extensions to this work can include implementing multiplexed illumination for further increasing the data acquisition speed and diffraction tomography for imaging thick samples.

Table of Contents

Abstract	ii
Table of Contents	iv
List of Figures.....	vii
Acknowledgements	xi
Declaration	xii
Abbreviations	xiii
Publications	xiv
Chapter 1 Introduction.....	1
1.1 Motivation	1
1.2 Conventional imaging techniques.....	3
1.2.1 Motorized scanning	3
1.2.2 Super-resolution techniques	4
1.2.3 Mesolens.....	4
1.2.4 Flatbed scanner with CCTV lens	5
1.2.5 Pixel super-resolution	6
1.2.6 Gigapixel monocentric multi-scale camera	7
1.2.7 Aperture-synthesis imaging.....	7
1.2.8 Spatial ptychography	9
1.2.9 Fourier ptychography.....	10
1.3 Objectives of the research	11
1.4 Thesis layout.....	12
Chapter 2 Fourier ptychography review.....	14

2.1	Theory	14
2.1.1	Space-Bandwidth product	18
2.2	FP reconstruction algorithms.....	20
2.2.1	FP optimization problem	20
2.2.2	FP reconstruction procedure	21
2.2.3	FP optimization variations.....	23
2.2.4	Information multiplexing	27
2.2.5	System error estimation algorithms.....	28
2.3	FP robustness analysis.....	30
2.3.1	Fourier space overlap requirement	31
2.3.2	Partial coherence limits	32
2.3.3	Illumination intensity fluctuations	33
2.3.4	Noise tolerance	34
2.3.5	LED position tolerances	35
2.3.6	Pupil errors	36
2.3.7	LED sampling pattern.....	38
2.4	FP experimental configurations.....	39
2.4.1	LED multiplexing with quasi-dome array	39
2.4.2	Oil-immersion condenser	40
2.4.3	Aperture scanning	41
2.4.4	Liquid crystal display (LCD) setup	41
2.4.5	Laser scanning.....	42
2.4.6	Reflective FP setup.....	43
2.4.7	3D FPM.....	44
2.4.8	Raspberry Pi FP setup	44
2.4.9	Macroscopic FP with camera array	45
2.4.10	Single pixel FP	46
2.5	Summary.....	46
Chapter 3	Multi-Aperture FPM.....	48
3.1	MA-FPM Theory	48
3.1.1	MA-FPM design parameters	51
3.2	Fresnel propagations based FPM reconstruction.....	53
3.2.1	Fresnel propagation algorithm	54
3.2.2	Field propagation using Fresnel diffraction integral.....	56
3.2.3	Pupil shift calculations.....	61

<i>Table of Contents</i>	VI
3.2.4 Experimental validation	67
3.2.5 Spatially varying frequency sampling	69
3.3 Summary.....	73
Chapter 4 Multi-Aperture FPM experimental validation.....	74
4.1 Experimental setup	74
4.2 Calibration procedure	77
4.2.1 Aberrations estimation.....	79
4.2.2 Image registration	81
4.2.3 Calibration results	82
4.3 Reconstruction algorithm	84
4.4 Experimental results.....	85
4.5 Summary.....	89
Chapter 5 Scheimpflug MA-FPM	90
5.1 Curved lens array	90
5.2 Scheimpflug principle	91
5.3 Scheimpflug MA-FPM setup	94
5.3.1 SMA-FPM design parameters.....	95
5.3.2 SMA-FPM experimental setup 3D-model	97
5.3.3 SMA-FPM experimental setup	101
5.4 Scheimpflug configuration recovery model	107
5.5 Scheimpflug FPM experiment.....	112
5.6 Summary.....	116
Chapter 6 Conclusion and future work	118
Future work	121
References	125

List of Figures

Figure 1.1 Time-lapse wide FoV phase-contrast imaging of HeLa cells. Taken from [4].	2
Figure 1.2 Thorlabs EV102 - EnVista™ Whole-Slide-Scanning Microscope for bright-field Imaging. Taken from [8].	3
Figure 1.3 Mesolens setup schematics. Taken from [19].	5
Figure 1.4 Flatbed scanner with CCTV lens. Taken from [20].	6
Figure 1.5 Multi-aperture foveated imaging for photography [21]. A prism array shown in (a) is placed on top of a flat camera array to create an assembly as shown in (b) to achieve wide FoV foveated image using pixel super-resolution. Figure provided by Guillem Carles.	6
Figure 1.6 Gigapixel monocentric multi-scale camera. Taken from [26].	7
Figure 1.7 Synthetic-aperture imaging methods. (A) Taken from [29]. SF is the beam expanding optics with a pinhole (B) Taken from [30].	8
Figure 1.8 Spatial ptychography setup schematic. The laser light is cropped using an aperture to create a spot. This spot is reimaged onto the sample plane and the resultant diffracted light is captured using a detector. The sample is mechanically scanned to scan the spot.	9
Figure 1.9 First Fourier ptychography setup demonstrated. Taken from [3].	10
Figure 2.1 A) Ewald sphere representation. Taken from [61]. B) Frequency sampling due to oblique illumination (FP) and SIM. Taken from [62].	16
Figure 2.2 “Wood stem at 3 years cross-section” sample slide image. The scale bar for phase profile goes from -2 to 2.5 radians.	17
Figure 2.3 Flowchart of FP reconstruction algorithm.	22
Figure 2.4 Overlap requirement in Fourier ptychography. Sub-image A is taken from [94].	31
Figure 2.5 Illumination fluctuation errors. Taken from [88].	33
Figure 2.6 Experimental results demonstrating artefacts due to noise subtraction. (A) is reconstructed with no noise subtraction. (B) is reconstructed with offset calculated from the average. (C) is reconstructed with larger offset than the value calculated from the average.	34
Figure 2.7 Reconstruction error due to LED position mismatch. (c1) low-resolution image. (c2) FPM reconstruction with LED position errors. (c3) FPM reconstruction with corrected LED positions. Image taken from [89].	36

Figure 2.8 Reconstruction errors due to error in the estimated pupil. (A) Experimental results with error in pupil aberrations, taken from [88]. (b1-b4) Simulated results with error in pupil shape.	37
Figure 2.9 Simulation results with different sampling patterns. Taken from [101].	38
Figure 2.10 Quasi-dome LED array. Taken from [92].	40
Figure 2.11 Resolution enhanced Fourier ptychography microscope. Taken from [93].	40
Figure 2.12 Aperture scanning Fourier ptychography setup. Taken from [63]. ..	41
Figure 2.13 Liquid crystal display illumination engineering for FP. Taken from [102].	42
Figure 2.14 Laser scanning FP systems. (A) Taken from [91]. (B) Taken from [103]. (C) Taken from [104].	42
Figure 2.15 Reflective FP setups. (A) Taken from [105]. (B) Taken from [106]. .	43
Figure 2.16 FP microscope using Raspberry pi hardware. Taken from [48].	45
Figure 2.17 Macroscopic FP with camera array setup. Taken from [110].	45
Figure 2.18 Single pixel FP setup. Taken from [111].	46
Figure 3.1 MA-FPM theory depiction.	49
Figure 3.2 Sampling differences between FPM and MA-FPM. (a) FPM frequencies sampling for on-axis illumination. (b) FPM frequencies sampling for off-axis illumination. (c) MA-FPM frequencies sampling for on-axis lens and off-axis lens for on-axis illumination.	50
Figure 3.3 MA-FPM experimental design. P_1 - LED array plane. P_2 - Object plane. P_3 - lens array plane. P_4 - Detector array plane. S_s - Separation between LEDs in the array. S_d - Distance between the LED array plane and the object plane. u_c - Distance between the object plane and the lens array plane. v_c - Distance between the lens array plane and the detector array plane. L_s - Centre to centre distance between the lenses in the array. D_s - Centre to centre distance between the detectors in the array.	52
Figure 3.4 Fresnel propagation based reconstruction algorithm.	55
Figure 3.5 Pupil shift depiction. In Fresnel method, the frequencies shift due to the illumination angle is depicted as the apparent aperture shift, shown as the arrow headed dotted lines lens. In Fraunhofer method, frequencies shift is calculated using the angle between the excitation light beam and the light beam recorded by the lens (represented by the arrow headed dashed line). This is shown as θ in the figure. The dotted black line shows the optical axis of the system and the black bold arrow headed line shows the illumination angle of the LED.	64
Figure 3.6 Fresnel vs Fraunhofer pupil position difference	66
Figure 3.7 FPM data reconstruction using the Fresnel method and the Fraunhofer method.	67
Figure 3.8 Spatial frequencies sampling across the FoV	69

Figure 3.9 Bright-field diffraction ring simulation: A flat transparent object with no phase variation is chosen as the object. (a) shows Fraunhofer method simulation where a bright-field ring is not observed, instead the input object profile is seen. (b) shows Fresnel method simulation where a bright-field circle is observed but does not have right dimension since illumination wavefront curvature is not considered. (c) shows Fresnel method simulation where a bright-field circle is observed with right dimensions due to correct illumination wavefront curvature.	70
Figure 3.10 Bright-field diffraction ring experimental validation. Experimental image with a diffraction ring (in purple) is superimposed on the simulated image with a diffraction in green. Two scenarios are demonstrated, one where the illumination is collimated (a) and is a spherical wave from a point LED source (b).	71
Figure 4.1 MA-FPM experimental setup configuration. P_1 : LED array plane. P_2 : Object plane. P_3 : Lens array plane. P_4 : Detector array plane. S_s : Separation between the LEDs. S_d : Distance from the LED array plane to the object plane. u : Distance from the object plane to the lens array plane. v : Distance from the lens array plane to the detector array plane.	75
Figure 4.2 Aberrations and registration errors between the MAFP images from different cameras	77
Figure 4.3 Modelling aberrations in Zemax	80
Figure 4.4 Pupil aberrations. Units on the colour bar are radians.	81
Figure 4.5 Image registration.	81
Figure 4.6 MA-FPM Calibration results.....	83
Figure 4.7 MA-FPM reconstruction algorithm.	84
Figure 4.8 MAFP experimental results of calibration targets. 1951 USAF resolution calibration-target image is shown in (A) and a spokes calibration-target image is shown in (B).	86
Figure 4.9 MA-FPM experimental results. Full FoV reconstruction of a <i>woody dicotyled-stem cross section</i> taken at 3 years. Three segments of the full FoV are shown at the top.	88
Figure 5.1 Planar lens array (a) vs Curved lens array (b).....	91
Figure 5.2 Scheimpflug condition example application.....	93
Figure 5.3 Scheimpflug FP setup geometry showing the positions of the imaging lenses and the detectors. On-axis and off-axis FP systems are shown for comparison. The PSFs of these systems are shown in a1-a3.	94
Figure 5.4 Scheimpflug setup schematics.....	96
Figure 5.5 3D models of the setup parts. (a) Detector array holder (b) Lens array holder (c) Detector case.....	98
Camera 1.....	103
Read noise.....	103
Figure 5.6 Assembled 3D printed experimental setup	105

Figure 5.7 Comparison of distortion and NA variation in the FoV between different imaging systems.	108
Figure 5.8 DoF in a Scheimpflug condition setup. Image taken from [148].	110
Figure 5.9 Raw captured full frame images.	113
Figure 5.10 S-FPM reconstructions of a USAF resolution chart	114
Figure 6.1 Lens array holder designs. (a) and (b) are front and back of the proposed new lens array design. (c) and (d) are front and back of the current lens array design.	122

Acknowledgements

First of all, I would like to thank my first supervisor Prof. Andrew Harvey for providing me the opportunity to conduct my PhD research under his supervision. I am also grateful for his advice and support provided throughout my PhD study. I would also like to acknowledge the supervision support provided by my second supervisor Dr. Jonathan Taylor. His guidance and input helped me throughout the project in tackling several problems.

I am also glad to have wonderful colleagues in the Imaging concepts group. There were several intellectual conversations about optics which improved my understanding of the subject. I would particularly like to thank Dr. Paul Zammit for being a good friend and an amazing office mate who also helped me in debugging several problems within my research and proof read several of my documents. I would like to thank all the good friends I made in Glasgow for making my stay here delightful.

Lastly, I would like to thank my parents and brother for being supportive throughout my life and my career choices. I would like to thank my uncle Shankar Konda for his help in arranging the financial support for my PhD.

Declaration

I hereby declare that except where specific reference is made to the work of others, the contents of this dissertation are original and have not been submitted in whole or in part for consideration for any other degree or qualification in this, or any other university. This dissertation is my own work and contains nothing which is the outcome of work done in collaboration with others, except as specified in the text.

Pavan Chandra Konda
October 2017

Abbreviations

Acronyms / Abbreviations

FoV - Field-of-View

FP - Fourier ptychography

FPM - Fourier ptychographic microscopy

MAFP - Multi-aperture Fourier ptychography

MA-FPM - Multi-aperture Fourier ptychographic microscopy

SMA-FPM - Scheimpflug multi-aperture Fourier ptychographic microscopy

S-FPM - Scheimpflug Fourier ptychographic microscopy

EPRY - Embedded Pupil Recovery

DoF - Depth-of-field

NA - Numerical Aperture

PSF - Point spread function

ATF - Amplitude transfer function

OTF - Optical transfer function

MTF - Modulation transfer function

CDI - Coherent diffractive imaging

PD - Photodiode

SNR - signal-to-noise ratio

GSF - Gerchberg-Saxton-Fienup

FWHM - Full width at half maximum

CMOS - Complementary metal-oxide semiconductor

sCMOS - scientific complementary metal-oxide semiconductor

USAF - United states Airforce

SIM - Structured illumination microscopy

LED - Light emitting diode

PIE - Ptychographic iterative engine

ePIE - extended Ptychographic iterative engine

Publications

Following journal and conference articles have been published or are in the process of preparation from the contents of this thesis.

Journal publications:

- P. C. Konda, J. M. Taylor, and A. R. Harvey, "Multi-aperture Fourier ptychographic microscopy: High-speed gigapixel complex-field imaging microscopy platform", in preparation.
- P. C. Konda, J. M. Taylor, and A. R. Harvey, "Fresnel diffraction forward model for Fourier ptychographic microscopy", in preparation.
- P. C. Konda, T. Aidukas, J. M. Taylor, and A. R. Harvey, "Forward model development for Fourier ptychographic microscopy with Scheimpflug condition in multi-aperture systems", in preparation.

Conference publications:

- P. Konda, J. Taylor, and A. R. Harvey, "Multi-aperture Fourier Ptychography imaging in the near field," in Imaging and Applied Optics 2015, OSA Technical Digest (Online) (Optical Society of America, 2015), Paper CM3E.5.
- P. C. Konda, J. M. Taylor, and A. R. Harvey, "High-resolution microscopy with low-resolution objectives: correcting phase aberrations in Fourier ptychography," in Proc. SPIE 9630, Optical Systems Design 2015: Computational Optics, 96300X (September 23, 2015).
- P. C. Konda, J. M. Taylor, and A. R. Harvey, "Calibration and aberration correction in Multi-Aperture Fourier Ptychography," in Imaging and Applied Optics 2016, OSA Technical Digest (Online) (Optical Society of America, 2016), Paper CT2D.2.

- **P. C. Konda**, J. M. Taylor, and A. R. Harvey, "Scheimpflug multi-aperture Fourier ptychography: coherent computational microscope with gigapixels / s data acquisition rates using 3D printed components," in Proc. SPIE 10076, High-Speed Biomedical Imaging and Spectroscopy: Toward Big Data Instrumentation and Management II, 100760R (February 22, 2017).
- **P. C. Konda**, J. Taylor, and A. R. Harvey, "Fourier ptychography with Scheimpflug optics for multi-aperture applications," in Imaging and Applied Optics 2017 (3D, AIO, COSI, IS, MATH, pcAOP), OSA Technical Digest (online) (Optical Society of America, 2017), paper CW3B.3.

Following articles have been published or are in the process of submission from continuation of this work by Tomas Aidukas, partly supervised by me.

Journal publications:

- T. Aidukas, J. M. Taylor, A. R. Harvey and **P. C. Konda**, "Low-cost miniaturized Fourier ptychographic microscopy using Raspberry Pi camera", in preparation.
- T. Aidukas, **P. C. Konda**, J. M. Taylor, and A. R. Harvey, "High speed computational microscopy using Scheimpflug Multi-aperture Fourier ptychography", in preparation.

Conference publications:

- **P. C. Konda**, T. Aidukas, J. Taylor, and A. R. Harvey, "Miniature Fourier ptychography microscope using Raspberry Pi camera and hardware," in Imaging and Applied Optics 2017 (3D, AIO, COSI, IS, MATH, pcAOP), OSA Technical Digest (online) (Optical Society of America, 2017), paper JTU5A.17.

Chapter 1 Introduction

This chapter describes the motivation behind this work, the imaging challenges and applications. In addition, a brief review of existing microscopy techniques is provided to give an understanding of their limitations and the proposed solution. The last section of this chapter explains how the rest of the thesis is organized.

1.1 Motivation

Digital pathology, haematology and histology often require examination of a large sample area to provide better diagnostic accuracy. This requires imaging a wide field-of-view (FoV) with high resolution. This is also a requirement for research studies involving cell division and in-vitro fertilization treatments. These applications particularly require additional features from the microscope, i.e., large depth-of-field (DoF), phase-contrast imaging and high-speed data acquisition. Conventional microscopes are limited by diffraction to small FoV and narrow DoF. To capture a wide FoV image, a conventional microscope scans the sample, refocuses it at each position and captures the images. These images are then tiled to create a wide FoV image. This often can be very slow, requires expensive high-precision translation stages and well-corrected microscope optics [1]. Tiling images also sometimes results in brightness variations and edge artefacts [2]. To address these issues Fourier ptychography (FP) was developed recently [3]. FP can produce gigapixel resolution images with low-cost components and does not require scanning.

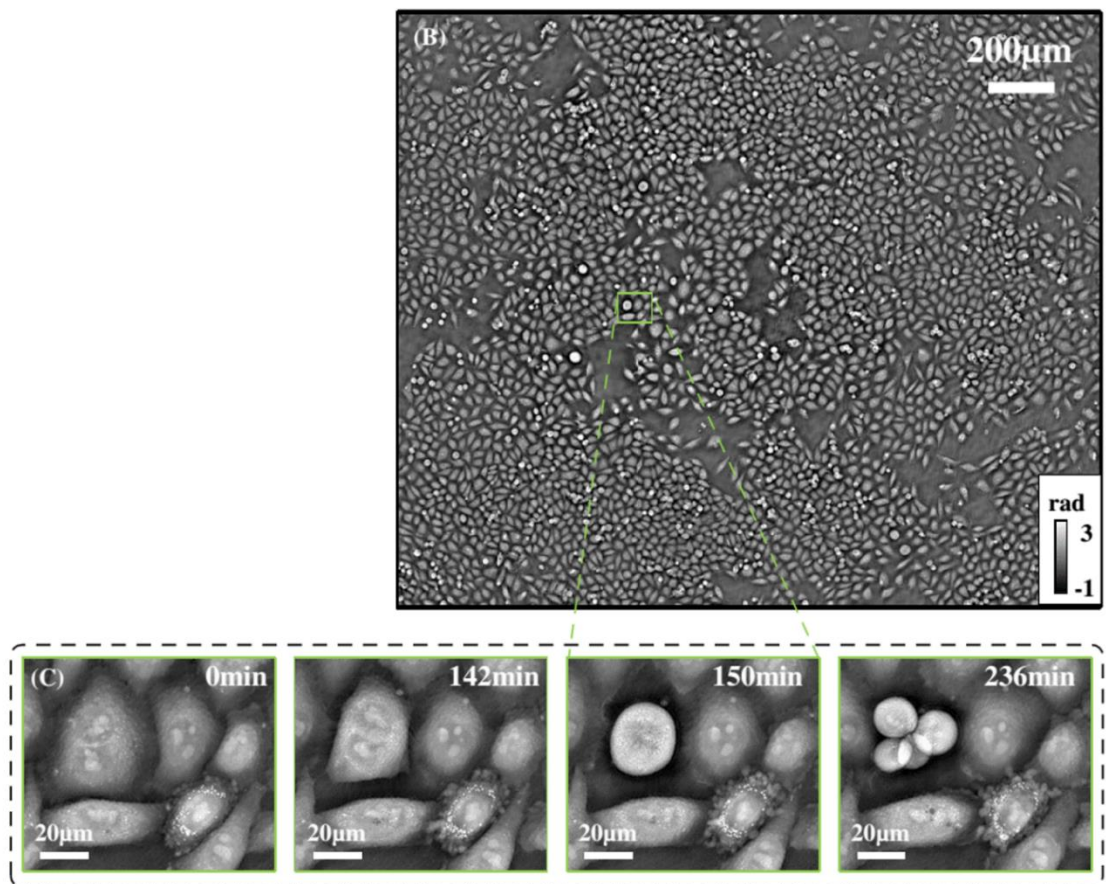


Figure 1.1 Time-lapse wide FoV phase-contrast imaging of HeLa cells. Taken from [4].

An example wide FoV image is shown in Figure 1.1 where a cell culture of HeLa cancer cells was imaged under time-lapse. This image is captured using Fourier ptychographic microscopy (FPM) technique [3,5] with a high-speed sCMOS camera and a custom built bright LED array. FPM provides a wide-FoV coherent image (amplitude and phase distribution) with large DoF using low numerical aperture (NA) lenses and time-sequential synthetic high-NA illumination using a programmable LED array. Due to its time-sequential nature, this is limited to static samples and not suitable for high-bandwidth usage applications like in digital pathology or cell cultures. A custom LED array can be used with an LED multiplexing strategy to improve the speed [5,6] but it requires an expensive high-speed camera, making this a high-cost setup. The proposed multi-aperture Fourier ptychographic microscopy (MA-FPM) technique has all the advantages of FPM; in addition, it provides high-speed imaging at low-cost, which will solve the imaging problems mentioned earlier.

1.2 Conventional imaging techniques

This section discusses various imaging techniques that can achieve wide FoV imaging with high resolution. These techniques are developed for imaging problems similar to the scenario discussed earlier, i.e., large space-bandwidth product (SBP) requirement [7]. A brief description of each of these techniques is given along with their limitations.

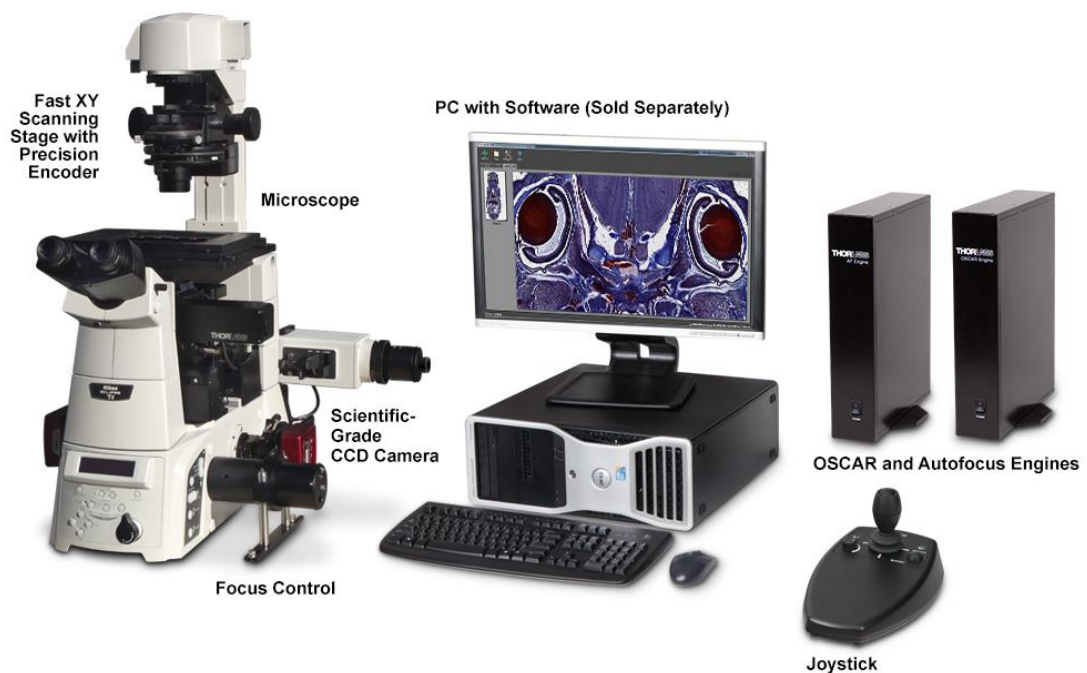


Figure 1.2 Thorlabs EV102 - EnVista™ Whole-Slide-Scanning Microscope for bright-field Imaging. Taken from [8].

1.2.1 Motorized scanning

A conventional bright-field microscope with motorized XY scanning is most commonly used due to the high-quality images offered by the objectives, which are well corrected for aberrations. An example microscope sold by *Thorlabs* is shown in Figure 1.2. These microscopes are often extremely expensive due to the high-quality objectives and high-precision translation stages used (£66,000 for *Thorlabs EV102*). They are still significantly slow: a 10mmx10mm FoV image with 15X magnification takes 35 seconds. This is due to the time required for translating

the object and focusing at each section. Scanning can also be performed on other imaging modalities, such as fluorescence microscopy.

1.2.2 Super-resolution techniques

Super-resolution imaging is performed using fluorescence to study several fundamental sub-cellular biological processes. These techniques can provide extreme resolutions up to 1nm [9]. A general procedure for these techniques involves activating a single fluorophore at a time and localizing its position from centroiding the generated point spread function (PSF). These techniques are limited to the fluorescence modality and require specialized fluorophores as observed in STED [10], STORM [11] and PALM [12,13], which limits their applications.

Structured illumination microscopy (SIM) encodes high-spatial frequency information inside the pass-band of the objective using Moiré fringe patterns [14,15]. This technique involves illuminating the sample using several grating illumination patterns rotated with respect to each other. These images are then stitched using special algorithms. This has also been demonstrated with speckle patterned illuminations [16-18].

These techniques are limited to fluorescence, hence cannot be applied to histological studies where the samples are inspected using bright-field and multi-spectral imaging modalities.

1.2.3 Mesolens

The Mesolens is a recently developed microscope objective to be used for wide FoV imaging of samples embedded inside immersion media using confocal scanning [19]. This objective uses expensive, large, custom-built lenses to correct for the aberrations. A sample of 6mm width, 3mm thickness is imaged at 0.47 NA resolution using this setup resulting in a 400 megapixels image at Nyquist sampling. This objective is specifically developed for imaging thick fluorescent samples in immersion media, which is not a requirement for histology samples.

This objective is also bulky and extremely expensive due to the size of the optical components required and the aberration correction.

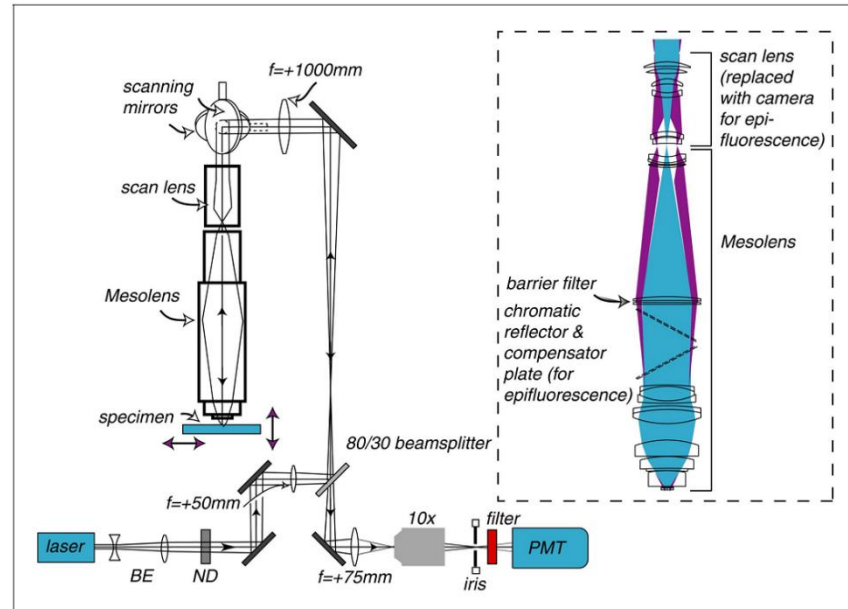


Figure 1.3 Mesolens setup schematics. Taken from [19].

1.2.4 Flatbed scanner with CCTV lens

A microscope setup with a flatbed scanner was proposed in [20] which uses a commercial Pentax CCTV lens C30823KP as a microscope objective. This lens is well corrected for spatially varying aberrations. Hence, it can capture images with 10mm FoV at 1.5 microns resolution resulting in 180 megapixel images at Nyquist sampling. The CCTV lens used in this setup is expensive and it is limited to a single resolution performance. This setup is also quite large due to the use of the flatbed scanner. Phase contrast and dark-field imaging cannot be performed using this setup. This setup also depends on high quality objectives similar to the Mesolens, resulting in expensive and bulky setups.

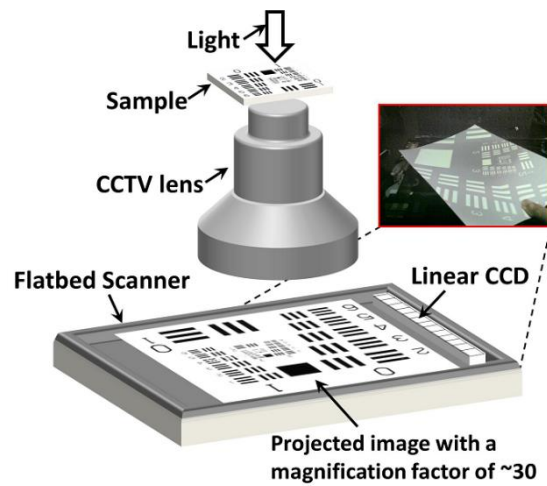


Figure 1.4 Flatbed scanner with CCTV lens. Taken from [20].

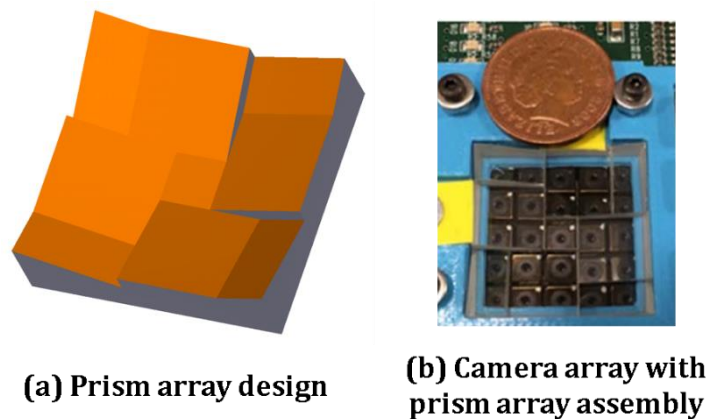


Figure 1.5 Multi-aperture foveated imaging for photography [21]. A prism array shown in (a) is placed on top of a flat camera array to create an assembly as shown in (b) to achieve wide FoV foveated image using pixel super-resolution. Figure provided by Guillem Carles.

1.2.5 Pixel super-resolution

In commercial low-cost mobile phone camera modules, the pixel-size of the sensors is larger than the diffraction spot. Hence the imaging resolution is decreased due to pixel-aliasing. An array of these pixel-aliased cameras are used to super-resolve these images up-to the diffraction limit of the optics [22,23]. In addition, a prism array can be added onto these cameras as shown in Figure 1.5. This will increase the FoV, providing a wide-FoV high-resolution foveal image. This

technique can be useful for surveillance or recording sports [24,25], but cannot be applied to microscopy where the images are not aliased.

1.2.6 Gigapixel monocentric multi-scale camera

An optical system is proposed in [26,27] which is capable of obtaining gigapixel images with the help of an array of microcameras, similar to the previous design. Here a special objective is designed which can relay an extremely wide-FoV image with large F-number onto a curved plane, which can then be reimaged by the microcameras as seen in Figure 1.6. The image is magnified by the objective lens such that the relay image's F-number is matched by the microcameras' F-number, which allows this setup to capture high-resolution wide-FoV images. This design can be adopted for microscopy but the objective design would suffer from short working distances and narrow depth of field.

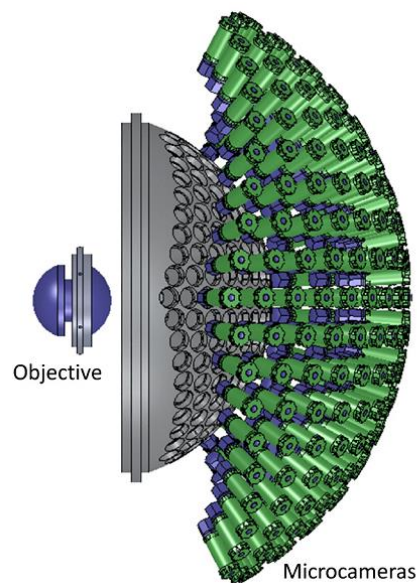


Figure 1.6 Gigapixel monocentric multi-scale camera. Taken from [26].

1.2.7 Aperture-synthesis imaging

Aperture-synthesis is a widely used imaging technique in radio-astronomy [28] and similar techniques have been demonstrated for optical wavelengths. Aperture

synthesis requires phase information to stitch the spatial frequencies; conventionally the phase is recovered using interferometry for optical wavelengths. Two experimental setups have been proposed for gigapixel imaging, as shown in Figure 1.7.

In setup (A), a holographic measurement is performed by using the reference wave from the fibre. The detector is then scanned with 50% overlap between successive captured diffraction pattern sections to create a large synthetic-aperture, which can be used to recover a gigapixel image. This technique, however, suffers from severe speckle artefacts since a laser illumination is required. Stitching of the synthetic aperture is also not an efficient process since the diffraction pattern does not have any good contrast features for image registration [29].

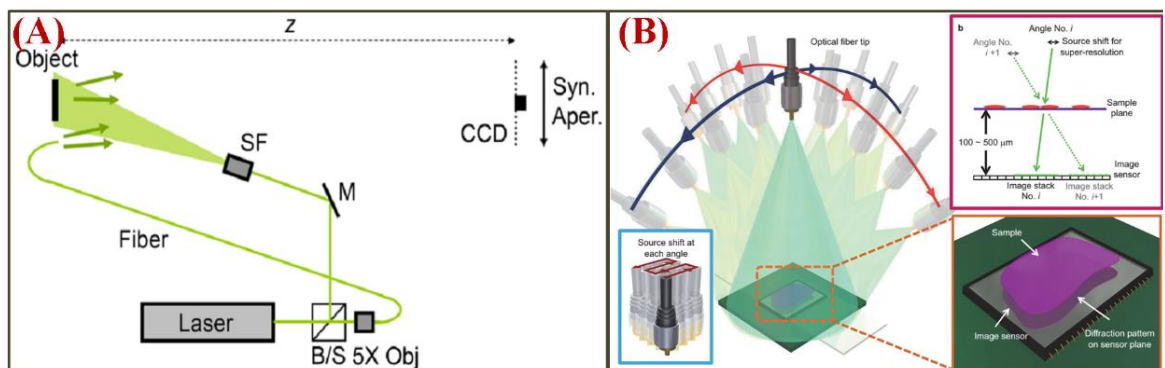


Figure 1.7 Synthetic-aperture imaging methods. (A) Taken from [29]. SF is the beam expanding optics with a pinhole (B) Taken from [30].

Setup (B) uses an on-chip microscope configuration for obtaining a high-NA diffraction field [30,31]. According to Fresnel field propagation, the FoV in a lensless diffraction setup is limited by the pixel-size [7]. A smaller pixel size is required for achieving wide FoV; here this is achieved by performing pixel super-resolution. The illumination angle is changed such that a sub-pixel shift of the diffraction field is produced on the detector. A range of angles is used to achieve much smaller pixel size than the detector pixel size, hence increasing the FoV. The phase reconstruction in this technique is achieved by Gerchberg-Saxton-Fienup algorithm [32]. This algorithm is not robust, hence can be problematic.

This technique also suffers from long data-acquisition time, which cannot be improved by multiplexing schemes [33].

1.2.8 Spatial ptychography

A coherent diffractive imaging (CDI) technique named ptychography was developed for robust phase reconstruction, which also provides wide-FoV imaging [34-41]. The object is illuminated by a spot of known amplitude and phase profile. The light from this spot is diffracted by the object and the corresponding diffraction pattern is recorded by a camera sensor as seen in Figure 1.8. This spot is scanned across the sample and corresponding diffraction patterns are recorded. These diffraction patterns are then stitched using Gerchberg-Saxton-Fienup type algorithms [32,42,43]. These algorithms are not robust and often get stuck at local minima [44,45]. In ptychography, when the illumination spot is scanned across the sample, an overlap of around 60% is maintained between two successive spots. This redundancy in data provides better convergence; also, a large FoV complex-field image is recovered in the process.

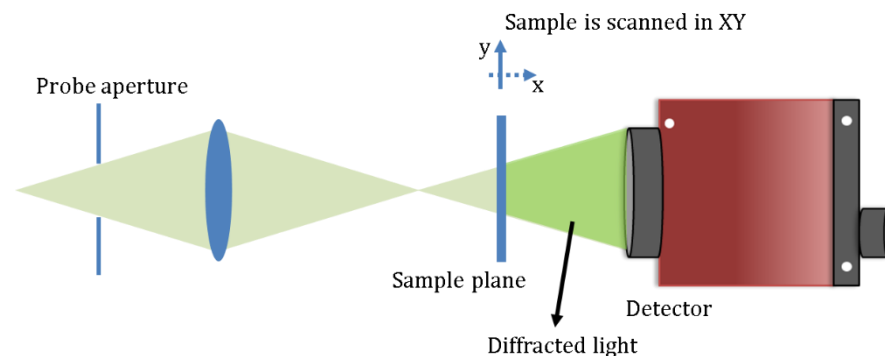


Figure 1.8 Spatial ptychography setup schematic. The laser light is cropped using an aperture to create a spot. This spot is reimaged onto the sample plane and the resultant diffracted light is captured using a detector. The sample is mechanically scanned to scan the spot.

Ptychography satisfies the imaging requirements of the given problem: a wide FoV, extended DoF and phase recovery. However, this technique is slow due to the scanning process.

A variation of ptychography has been proposed with single-shot capability [46] during the development of this thesis. Despite providing all the

imaging requirements, this technique is still expensive due to the high-quality translation stages and detectors required in the setup. The requirement of a high-coherent illumination source increases the speckle noise in the images, hence reducing their image quality. This technique also suffers from the high-dynamic range requirement of the sensors due to the presence of lower and higher diffraction orders at the same time. It also suffers from positioning errors of the scanning spot. Spatial ptychography is ideal for applications such as X-ray imaging or extreme UV imaging, where it is not possible to make lenses since it can work without lenses [47].

1.2.9 Fourier ptychography



Figure 1.9 First Fourier ptychography setup demonstrated. Taken from [3].

Fourier ptychography (FP) is a synthetic aperture technique that is conceptually similar to spatial ptychography, where the object's Fourier spectrum is scanned instead of the object itself. This is achieved by changing the angle of the illumination wavefront using a programmable LED array. FP offers all the advantages of spatial ptychography but does not require a high-coherence light source. Since no moving parts are required and the detector does not require a high dynamic range, the system can be built using extremely low-cost components [48]. Similar to spatial ptychography, this technique is also time-sequential, hence suffers from long data acquisition times. The primary objective

of this thesis is to improve the data-acquisition speeds in FPM by parallelizing data acquisition. The Fourier ptychography principle is explained in detail in the following chapter. The first FPM setup reported is shown in Figure 1.9. This setup was built by adding a low-cost modification to the illumination of a commercial microscope.

1.3 Objectives of the research

As discussed earlier, FPM provides all the necessary features required for the imaging problem at hand - wide FoV, complex field imaging, low-cost setup and extended DoF - except the speed. Hence, the primary objective of this thesis is to improve the speed of FPM setups. We chose the approach to use multiple objective lenses to parallelize the data acquisition. The key objectives of this thesis are as follows:

- Develop theory and experimental configurations for parallelized data acquisition
- Develop suitable calibration procedure for the experimental setup
- Develop reconstruction algorithms for the proposed configuration
- Validate the parallelized data acquisition theory experimentally

During the course of this work, the following original contributions were made:

- Developed Multi-Aperture FPM theory for parallelized data acquisition
- FPM reconstruction algorithm based on Fresnel propagations required for MA-FPM has been developed and implemented successfully
- MA-FPM calibration procedure was developed and implemented successfully
- MA-FPM reconstruction algorithm was developed and implemented successfully
- MA-FPM theory has been validated experimentally
- Scheimpflug MA-FPM experimental configuration was proposed for reducing the aberrations in the captured raw images

- A 3D printed experimental setup was built for SMA-FPM configuration to reduce the cost of the prototype
- The FPM recovery model for Scheimpflug configuration has been proposed and preliminary experimental validation was completed

1.4 Thesis layout

The primary objective of this thesis is to build a high-speed gigapixel coherent microscope using parallel imaging systems based on FPM. This thesis outlines the development of the proposed technique. This chapter introduced the imaging problem at hand and the reason FP was chosen as the suitable candidate.

Chapter 2 describes the fundamental principle and theory of FP. Then various reconstruction algorithms used for FP reconstruction are discussed. FP is a relatively new technique; the first paper was published at the start of this thesis work. Hence, a review on the robustness of FP is discussed along with various experimental implementations developed so far.

Chapter 3 introduces the multi-aperture FPM concept. The problem of using conventional Fraunhofer FP reconstruction algorithms for MA-FPM is discussed and Fresnel FP reconstruction algorithm is proposed. This algorithm is validated on experimental data and its robustness against a conventional algorithm is discussed.

Chapter 4 presents the experimental validation of MA-FPM using a planar lens array setup. The MA-FPM calibration process is described along with the experimental results. The results in this chapter validate the MA-FPM theory.

Chapter 5 presents a curved lens array as a better alternative to planar lens array. Scheimpflug condition based MA-FPM experimental setup is proposed for aberration reduction in the curved lens array configuration. A 3D printed experimental setup is demonstrated to produce a low-cost setup. Theory for Scheimpflug FPM recovery model is proposed and is validated experimentally.

The work presented in this thesis is reviewed in Chapter 6 with some conclusions from the research conducted. Future directions of the current work are then discussed, which includes proposed improvements to the Scheimpflug MA-FPM setup and possible addition of new features to MA-FPM such as 3D FPM.

Chapter 2 Fourier ptychography review

MA-FPM is a variation of FPM technique as discussed in the previous chapter. FP is a relatively new technique and a rapidly growing one - the first paper published in 2013 had 328 citations at the time of this writing. There has been a significant development in the area of reconstruction procedures and experimental methods in this time. Since FP is fundamental to our technique, an extensive review of FP is provided in this chapter along with description of some terminology used in this work. Theory behind the FP principle is discussed first, and space-bandwidth product terms are introduced. FP reconstruction model is discussed and various algorithms are discussed. A robustness analysis is then performed on the parameters involved in the experiment. In the end, various FP experimental setups reported in the literature are discussed.

2.1 Theory

The term ptychography was coined by German scientist Walter Hoppe in 1970s [49]. Ptycho means fold in German and graphy means write, it was used to describe the use of convolution, a mathematical process of folding two functions together. The concept of ptychography was invented by Hoppe, he illuminated the object with multiple scanning spots and recorded their interference patterns [50-52]. The diffraction interference pattern was used to infer the phase information. Unlike the holography setups where a reference beam is required to encode the phase information, here the diffraction patterns from multiple spots in a sample with overlapping areas are interfered with each other. The phase information of the object is recovered from these interference patterns. In the modern day ptychography, the power of computers is exploited to implement an

iterative phase retrieval algorithm to recover the phase [35]. In ptychography, the probe illuminating the sample is scanned with overlap between adjacent scanning positions to provide redundancy in the captured data for robust reconstruction. In FP, the angle of the illumination is tilted instead of scanning the probe to capture higher order diffraction information. The idea of shifting the illumination angle to sample higher spatial frequency information was also proposed by Hoppe in 1971 [53] and later implemented in the electron microscopy setups [54,55]. The concept of FP was reintroduced in 2013 in the context of optical microscopy using partial coherent illumination sources such as LEDs to present low-cost experimental setups. In the modern FP [3], the image of the diffraction pattern using a microscope objective, unlike the electron microscopy setups where the diffraction information is recorded instead. It should be noted that despite recording information in the image plane, the information capture by both real-space ptychography and FP is same due to the reciprocity between the object's complex field and its diffraction information [56]. The theory of FP in the context of aperture synthesis is explained later followed by a review on FP.

FP theory is similar to aperture synthesis, a widely used technique in radio astronomical telescopes [28,57-59]. In radio astronomy, a single telescope captures a discrete spatial frequency component of the Fourier spectrum; an array of these telescopes is used to capture a large set of spatial frequencies. In some cases the rotation of the earth is used to vary the baseline and hence increase the number of measurements using a small number of telescopes [60]. The phase of these individual Fourier components is required to produce an image, which is retrieved electronically for radio waves. In FP, instead of a single Fourier component captured by the telescope, a set of Fourier components (band-passed by the amplitude transfer function (ATF) cut-off) are recorded for each measurement. These Fourier components (spatial frequencies) are shifted by changing the angle of illumination according to the Ewald sphere theory as shown in Figure 2.1. Another crucial difference from radio astronomical telescopes is that, in FP, the images of the band-passed frequencies are recorded rather than the frequencies.

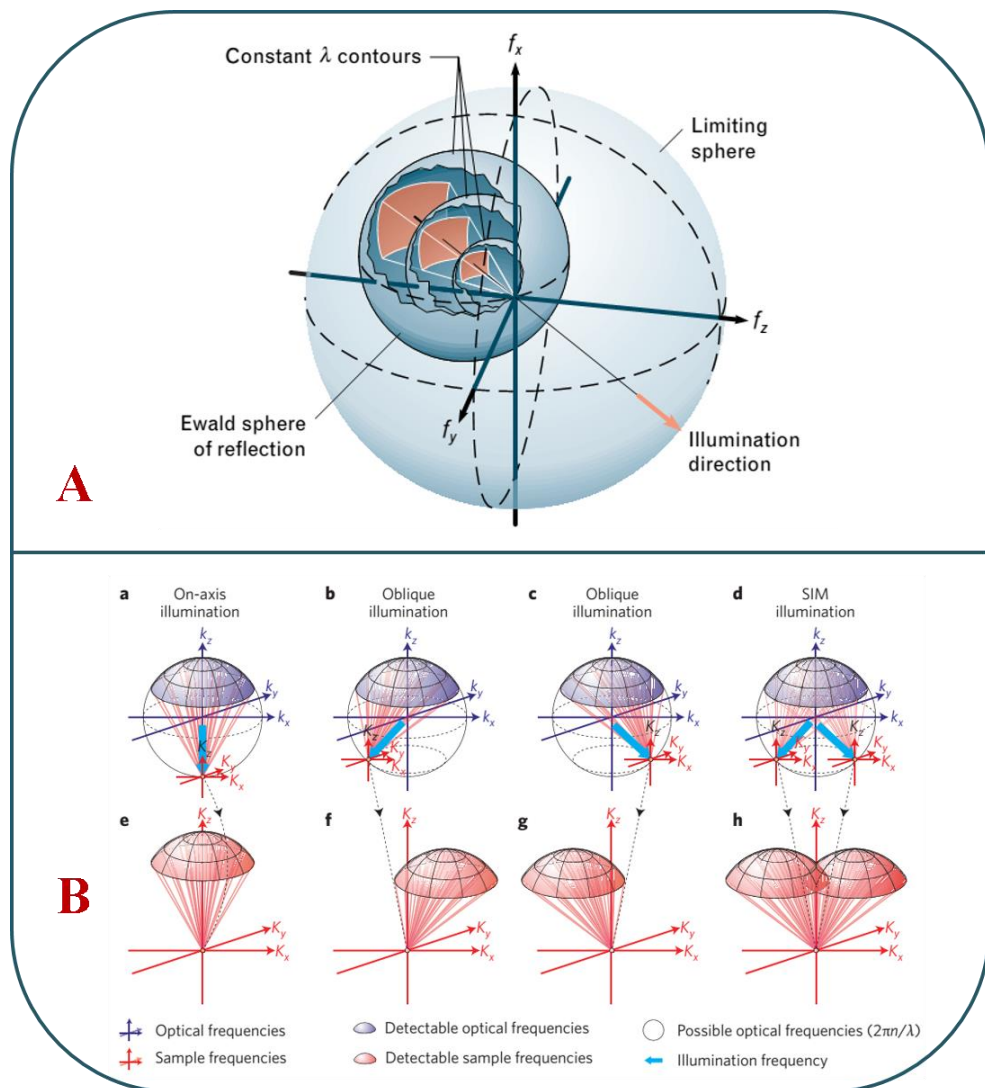


Figure 2.1 A) Ewald sphere representation. Taken from [61]. B) Frequency sampling due to oblique illumination (FP) and SIM. Taken from [62].

The surface of the Ewald sphere gives the region of spatial-frequencies sampled by an imaging system based on the illumination angles [61]. The $2/\lambda$ sphere (the limiting sphere) represents all the set of frequencies that can be recorded in air for a particular wavelength λ . According to this theory, the illumination angle can be changed to sample a distinct set of spatial frequencies (as seen Figure 2.1 B). In FP, this property is exploited by using a programmable LED array to illuminate the sample from various angles. This can also be realized by translating the aperture of the objective-lens or the pupil, similar to aperture synthesis techniques [33,63].

Unlike radio astronomy, the phase of these spatial frequencies cannot be directly recovered electronically for optical waves. Conventionally this is achieved using interferometry techniques, which can be expensive and complicated. Hence Gerchberg-Saxton-Fienup (GSF) type of reconstruction algorithms are used [32,43]. As mentioned in the previous chapter, these algorithms suffer from stagnation problems. This is solved in the spatial ptychography technique by maintaining an overlap in the acquired data; hence similar overlap requirement is used in FP. The principle difference for reconstruction between spatial ptychography and FP lies in the unknown values; amplitude and phase are unknown in the object space for spatial ptychography whereas these are unknown in the frequency space for FP. It should be noted that these techniques work under the thin-sample approximation, advanced algorithms are required to deal with thick samples [38,64-66].

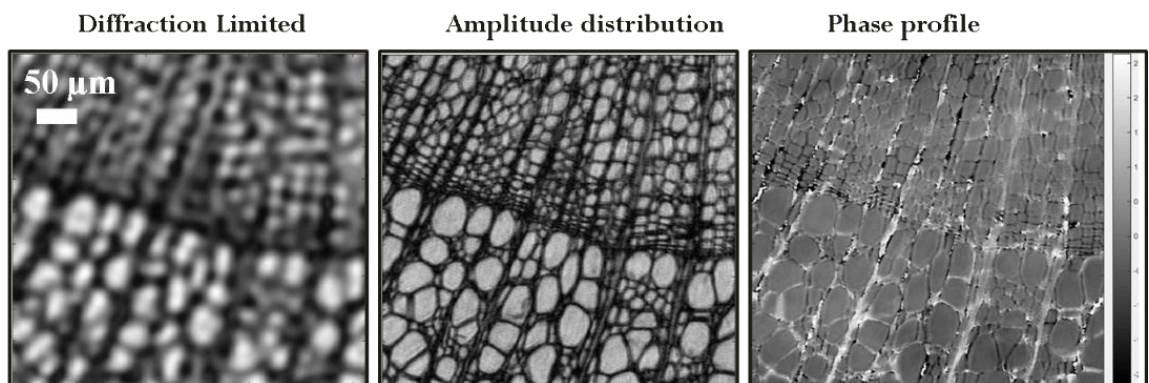


Figure 2.2 “Wood stem at 3 years cross-section” sample slide image. The scale bar for phase profile goes from -2 to 2.5 radians.

An example FPM image generated in this research is shown in Figure 2.2. Here the high-resolution image is recovered from the frequencies captured by using 225 illumination angles. Since phase is reconstructed during the process, the sample can also be inspected using the phase-contrast modality as seen on the right.

2.1.1 Space-Bandwidth product

Space-Bandwidth product (SBP) is a measure of complexity for a given mathematical function [7]. In optical systems, this can be used to measure the amount of maximum information passed through the system. For a bandlimited mathematical function in frequency space, it is possible to show that its Fourier transform (object space) cannot be bandlimited [7]. However, the values of this function in object space fall down to very small values after a certain region - experimentally this is due to the spatially varying aberrations or vignetting. This region (bandlimited space) can produce finite set of bins when sampled at Nyquist condition. The total number of these bins in this bandlimited space is defined as the space-bandwidth product.

SBP can be calculated theoretically when the bandlimited-space borders are provided in the object space. This requires defining a threshold limit for the values in the object to be treated as zeros to create the border, i.e., the threshold below which the object values are considered zero. The SBP of a system can vary depending on the definition of this threshold value. In conventional microscopes, usually the circle of least confusion is considered as the threshold value. For conventional optical systems the SBP is limited to around 30 megapixels [3,20]. Due to the current technology limitations, the experimentally achieved SBP is limited to typically around 5 megapixels - the size of the detector pixel array. In FP, the spatially varying aberrations can be corrected computationally; hence, the threshold value to create bandlimited space borders cannot be defined easily. This requires a rigorous analysis, which has not been reported in the literature yet. Hence, throughout the rest of this thesis SBP is quoted for experimentally achieved values instead of the theoretical maximum values. The SBP for an experimental system can be calculated using the following formula:

$$SBP = \frac{A_{Det}}{M^2 \times (\delta / 2)^2} \quad (2.1)$$

where, A_{Det} is the detector area, M is the system magnification and δ is the Rayleigh resolution limit - $\frac{1.22\lambda}{(NA_{obj} + NA_{illumination})}$. In this equation, the bandlimited space is defined as the FoV area and the bin size is determined by Nyquist sampling at the Rayleigh limit.

It should be noted that in a conventional imaging system the number of degrees of freedom (information captured) is half compared to FP systems, where optical phase is also recovered for every spatial position. Hence in systems where phase is recovered (such as FP), we define the SBP as twice the value calculated in the above equation.

2.1.1.1 Space-Bandwidth-Time product

In FP, time is sacrificed to increase the SBP of the system. Hence, a new term Space-Bandwidth-Time Product (SBTP) was coined [5]. This value defines the amount of information captured in a single snapshot. This is defined as the SBP of an imaging system divided by the number of snapshots required by the system. The SBTP of an FP system remains constant compared to a conventional system and improving this is a key objective of this thesis. This has been improved in [5] by reducing the redundancy in the data captured. In this work, this is achieved by parallelizing the data-acquisition.

2.1.1.2 Space-Bandwidth-Spectral-Time product

FP algorithms have been proposed to capture multiple colour information in a single image by either using a Bayer-filtered colour sensor [48,67] or spectral multiplexing on a monochrome sensor [68,69]. In such situations the spectral information is multiplexed, hence the SBTP when considered for a single wavelength will be small. Here a new term, Space-Bandwidth-Spectral-Time product (SBSTP) is proposed for these cases. SBSTP is a result of SBP multiplied by the number of wavelengths and divided by the total number of snapshots required.

2.2 FP reconstruction algorithms

Fourier ptychography follows a reconstruction procedure similar to that used in spatial ptychography [37] using Gerchberg-Saxton-Fienup principle [42]. These algorithms were first developed in the context of electron microscopy [70,71], later then extended to real-space ptychography and FP. There have been several variations applied in the optical, electron and X-ray imaging modalities [72-76]. They all can be formulated as an optimization model, which can be solved mathematically. There have been several mathematical formulations proposed for the FP model to provide robust convergence. Here the most promising models for FP are discussed in detail along with a brief description of other models and their drawbacks. In addition, procedures reported to correct the calibration errors in the experiment are discussed. Since FP models were inspired from real-space ptychography models, these are highlighted wherever appropriate.

2.2.1 FP optimization problem

The image formation process in FP can be described as follows:

$$I_i = \left| F \{ P \times O(k - k_i) \} \right|^2, \quad (2.2)$$

where I_i is the recorded intensity for the i^{th} illumination angle, F is the Fourier transform operation, P is the pupil transfer function of the imaging system, O is the frequency spectrum of the high-resolution object, k is the coordinate in the frequency plane and k_i is the off-set in the frequency plane corresponding to the shift produced by the i^{th} illumination angle.

In this equation, the unknown variable O can be recovered by rewriting the equation as follows:

$$O(k - k_i) = \tilde{P} \times F^{-1} \{ \sqrt{I_i} \times \exp(1j \times \Theta_i) \}, \quad (2.3)$$

where, \tilde{P} is the complex conjugate of the pupil function, θ_i is the phase of the recorded image amplitude $\sqrt{I_i}$ and F^{-1} is the inverse Fourier transform operation.

To recover O , the phase of $\sqrt{I_i}$ is required. Without the knowledge of the phase information this operation cannot be performed. The phase is estimated using the GSF algorithm but it is not the true value. Hence, this problem is rewritten as an error minimization problem for the estimated phase values as follows:

$$\min \left\| \sqrt{I_i} - F\{P \times O(k - k_i)\} \right\|, \quad (2.4)$$

Here, the object spatial frequencies are the estimated from algorithm similar to the GSF algorithm. This problem can be treated as a regularized optimisation problem [77] and this term which is minimized can be called as the cost function. Based on the definition of this cost function and the optimization procedure implemented, different convergence can be achieved [78]. The reconstruction procedure in most of the cases stays same; however, the object frequency-space update function varies depending on the cost function and the optimization procedure. A generalized reconstruction procedure is described in the next subsection and the update functions for various optimization methods are described later.

2.2.2 FP reconstruction procedure

The flowchart of FP reconstruction procedure is shown in Figure 2.3. Here coordinates r represents the spatial domain and k represents the frequency domain. The reconstruction procedure starts by estimating the spatial-frequencies $O(k)$ of the high-resolution object $I_{h_res}(r)$. This is then shifted according to the illumination angle i and filtered with the pupil function P to generate $O_i(k - k_i)$.

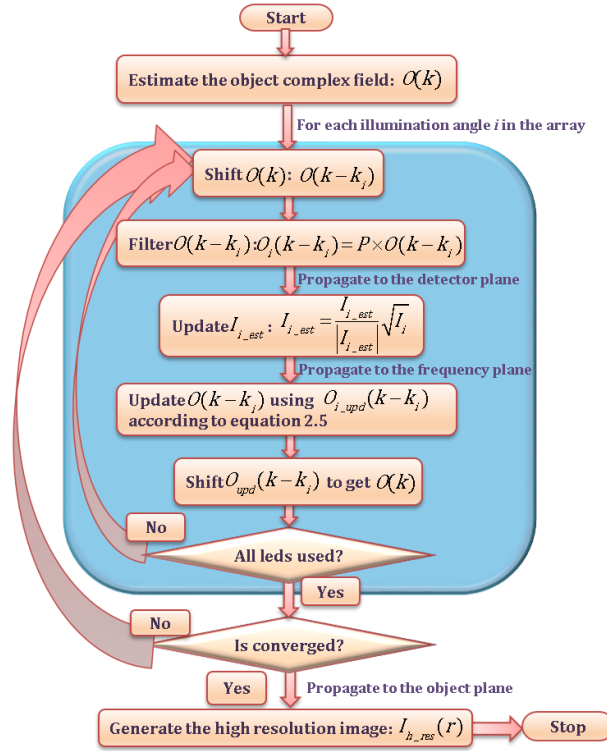


Figure 2.3 Flowchart of FP reconstruction algorithm.

This $O_i(k - k_i)$ is then propagated to the detector plane by using Fraunhofer propagation [7] to generate an estimate of the image formed on the detector I_{i_est} . The amplitude of this estimate is known from the experimentally recorded intensity image I_i . Hence, this amplitude is updated and the resultant new image estimate I_{i_est} is propagated back to the object frequency plane to form an update $O_{i_upd}(k - k_i)$. The shifted object spatial-frequencies $O(k - k_i)$ are updated using these estimates. If we assume a simple GSF based algorithm, the update equation would be:

$$O_{upd}(k - k_i) = O(k - k_i) + \frac{\tilde{P}}{|P|_{\max}^2} (O_{i_upd}(k - k_i) - O_i(k - k_i)), \quad (2.5)$$

This update is based on a simple gradient descent method [78]. This $O_{upd}(k - k_i)$ is shifted back to generate a new estimate $O(k)$. This is now used for the next illumination angle and the whole procedure is repeated until all the illumination

angles are used. This completes one iteration of the reconstruction algorithm. At the end of each iteration, the error in the estimated image is calculated. If this error is greater than the required error limits, then the entire process is repeated. Else, the process is terminated and the final $o(k)$ estimate is inverse Fourier transformed to recover the high-resolution object $I_{h-res}(r)$.

In FP reconstruction, the full FoV is divided into sub-images and processed independently. This is followed due to two primary reasons: partial coherence in the object plane and spatially varying aberrations. LED sources are used in most of the experimental configurations as discussed later in this chapter. These are partially coherent; hence, their effect needs to be considered. This is discussed in the later sections of this chapter. Even highly corrected objective lenses suffer from spatially varying aberration. Dividing the FoV into smaller segments allows FP to correct for these computationally by modifying the pupil function accordingly.

It should be noted that the FPM iterative algorithm is same as the real-space ptychography reconstruction algorithms. The equation (2.4) is same as the update function used in the extended ptychographic iterative engine (ePIE) [37]. The following discussion is performed in the context of FPM; however, it can also be applied to real-space ptychography. Several of the reconstruction methods developed in the context of FPM have already been implemented in the real-space ptychography literature. This is highlighted wherever possible to show the parallels between these techniques.

2.2.3 FP optimization variations

2.2.3.1 Cost functions

FP can be treated as a regularized optimization problem as discussed above. For an optimization problem, a cost function is required. For FP, the cost function can be defined in a few different ways. The most commonly used cost function is:

$$\min_{O(k)} f(O(k)) = \min_{O(k)} \sum_r \left| \sqrt{I_i(r)} - \left| F\{P * O(k - k_i)\} \right| \right|^2, \quad (2.6)$$

where, $f(O(k))$ is the non-convex function for the object spatial frequencies that needs to be minimised, $O(k)$ is the object frequency spectrum, r is the spatial coordinate in the object space, k is the coordinate in the frequency space, $I_i(r)$ is the experimentally recorded object intensity, F is the Fourier transform operation, P is the pupil function, $O(k - k_i)$ is the shifted object frequency spectrum and k_i is the frequency shift due to the illumination angle i .

Here the amplitudes of the estimated and recorded intensity images are minimised. Hence, this cost function is called amplitude-based cost function. Instead of the amplitudes, the intensity difference can also be used to create a cost function:

$$\min_{O(k)} f(O(k)) = \min_{O(k)} \sum_r \left| I_i(r) - \left| F\{P \times O(k - k_i)\} \right|^2 \right|^2, \quad (2.7)$$

This cost function is hence, called as intensity-based cost function. In these cost functions, only a single image is optimized; hence, these are called sequential methods, the frequency space is updated individually for each image within the iteration. Instead, the error in all the recorded images can also be combined together to create a cost function. These will be called global methods; the frequency space is updated at once for all the images at the end of each iteration [78]. The cost function for an amplitude-based global method is given as:

$$\min_{O(k)} f(O(k)) = \min_{O(k)} \sum_i \sum_r \left| \sqrt{I_i(r)} - \left| F\{P \times O(k - k_i)\} \right| \right|^2. \quad (2.8)$$

Similar cost function can also be written for intensity-based global cost function.

A comparison between these cost functions, sequential and global methods has been performed in [78]. In addition, cost functions based on Poisson and Gaussian noise models in the images were also developed. It has been concluded

that the amplitude-based cost function provides better convergence than intensity-based cost function and the amplitude-based cost function is similar to a Poisson noise model cost function. The Gaussian-noise model was found to have a cost function similar to the intensity-based cost function. Since most of the experimental setups in FP are Poisson noise limited, amplitude-based cost function should provide superior performance to the rest. The global methods were proven more robust compared to the sequential methods; however, they suffer from significantly longer computation times [78]. Hence, sequential amplitude-based methods are chosen for FP reconstruction.

2.2.3.2 Cost function optimization methods

The cost functions described above can be optimized using different mathematical frameworks. The simplest optimization method would be gradient descent method: a first order derivative is used to create an update function. For FP this update function is given in the equation 2.5 based on the sequential amplitude-based cost function. Since it is a first order method, this update can be influenced from the noise in the images. A more robust method can be generated by using first-order and second-order derivatives (Newton's method). However, these calculations can be intensive. Hence, approximations are used to create simpler update functions based on quasi-Newton method. For FP, this update function is given as:

$$O_{upd}(k - k_i) = O(k - k_i) + \alpha \frac{|P|}{|P|_{\max}} \frac{\tilde{P}(O_{i_upd}(k - k_i) - O_i(k - k_i))}{|P|^2 + \delta}, \quad (2.9)$$

where, α is the step size of the update function and δ is the regularization parameter. The δ is the wiener deconvolution constant and depends on the noise characteristics of the image. A higher value will result in very slow update of the optimization function and smaller value will result in high-frequencies domination in the image. Hence, δ needs to be chosen carefully [79]. This constant can also be chosen pixel by pixel to address the rapid variations in the intensities in the FPM images. In this thesis, this is chosen as a constant value for the entire reconstruction in a trial and error fashion. It should also be noted that the

equation (2.9) is same as the update function used in the ptychographic iterative engine (PIE) [35,36,80,81]. The only variation is in the plane where the update is being performed, in real-space ptychography it is performed in the object space whereas here it is performed in the frequency space. Hence, o will be the object's complex field in real-space ptychography, whereas it will be the object's Fourier transform in FPM.

A Wirtinger flow algorithm has been applied to the FP problem in [82]. Wirtinger flow uses a first-order derivative with specialized step size and initialization. Since it is still a first order method it is less stable compared to quasi-Newton method described above.

Convex phase-lift optimization methods were applied in [83,84] for both FPM and real-space ptychography. A convex method reframes the optimization problem in a higher-dimensional space to create an optimization problem with a convex convergence profile to ensure a global minimum. In FP, the optimization problem is non-convex, hence can be stuck at a local minimum. The convex optimization would work if the FP problem can be reframed properly, which cannot be achieved in the presence of noise and calibration errors in the system. Hence, quasi-Newton method is preferred which is found to have better convergence [78].

The step-size in update functions such as α in equation 2.9 is generally kept at a constant value. It has been demonstrated that an adaptive step-size strategy provides a better convergence, avoiding the local minima [85].

Various optimization frameworks have been discussed above. Overall, a sequential quasi-Newton method is proven as the most robust and computationally efficient method available. Therefore, this update function as shown in equation 2.9 is used in this work due to its robustness and speed among other variations. In addition, adaptive step-size strategy is also applied in the results shown in the chapter 5 of this thesis, which demonstrated the best convergence.

2.2.4 Information multiplexing

The experimental data in FP requires redundancy to provide a robust convergence as discussed in the later sections. Here information multiplexing is implemented to overcome the redundancy issues and produce faster data-acquisition times. In a single image acquisition, information from either different wavelengths or different LED positions is combined by summing the resultant intensities. This information is then de-multiplexed using modified reconstruction algorithms [6,68]. The major difference is that instead of processing a single illumination-angle or wavelength data at a single instance, multiple illumination angles or wavelengths are processed. The intensity update function is modified accordingly:

$$I_{i_est_upd}(j) = I_{i_est}(j) \sqrt{\frac{I_i}{\sum_j |I_{i_est}(j)|}}, \quad (2.10)$$

where, I_i is the intensity of the image obtained experimentally due to the sum of intensities from different LEDs/colours, $I_{i_est}(j)$ is the estimated intensity from LED/colour sequence number j , $I_{i_est_upd}(j)$ is the updated estimate of $I_{i_est}(j)$ and i is the low-resolution image sequence number. In any single image acquired a maximum of n LEDs/colours are summed, hence j goes from one to n . For e.g., if LED multiplexing is used with four random LEDs switched on at each time, then j denotes these four LEDs sequence from one to four. When wavelength is multiplexed, this j denotes the wavelength number. Details about these reconstruction procedure can be found in [6,68]. Information multiplexing is the key to further increase the SBTP of MA-FPM systems. In this work, however, this was not demonstrated experimentally, but this is proposed as the future work of this thesis. It should be noted that the equation (2.10) is derived from work in real-space ptychography where state mixtures of the imaging system such as partial coherence or vibrational motions were recovered within the reconstruction procedure [86].

2.2.5 System error estimation algorithms

In the cost functions described in the previous sections, the pupil function P and the illumination angle k_i are assumed as the known values. In experiment, these can deviate from the expected values due to unknown aberrations or alignment errors. Illumination intensity between different illumination angles and the LED wavelength can also vary between different LED array manufacturers. Hence, algorithms have been developed in literature to estimate these errors and provide superior quality reconstruction.

2.2.5.1 Pupil errors

Unknown aberrations in the optical system is the most commonly encountered problem. Well-corrected objective lenses can also suffer from spatially varying aberrations. Hence, within the reconstruction procedure the pupil function P is also assumed as an unknown value [87]. This creates a simultaneous optimization problem for O and P . The reconstruction procedure remains exactly same, with one additional step of updating the pupil function P along with O . The pupil function is also updated using the quasi-Newton method [6] as follows:

$$P_{upd} = P + \alpha \frac{|O(k)|}{|O(k)|_{\max}} \frac{\tilde{O}(k) \times (O_{i_upd}(k - k_i) - O_i(k - k_i))}{|O|^2 + \delta}, \quad (2.11)$$

This pupil function update exploits the redundancy in the captured data. The pupil function P remains same for all the recorded images; hence, it provides a better chance of convergence. In addition, this can only correct a small amount of unknown aberrations in the system. Any large variations will make the problem unstable, breaking the assumptions made for the simultaneous optimization problem formulation. The parallel to pupil recovery in real-space ptychography is the scanning probe beam. In ePIE, the probe is recovered simultaneously using equation (2.4) implementation [37].

An adaptive estimation algorithm has been proposed by using generalised pattern search [88]. This, however, is very slow and not required for small

aberration variations as described above. Hence, this is not used in this work. This can be used if the system has large unknown aberrations. In a typical FPM reconstruction method, it is advised to use the embedded pupil recovery (EPRY) discussed above to improve the reconstruction quality. Generalised pattern search method is not advised due to its slow convergence. If the system suffers from large aberrations then it is suggested to use a *Zemax* model to generate aberration estimates if the optical model is available.

2.2.5.2 LED position errors

After the pupil errors, the position errors of the illumination angles k_i constitute most of the remaining artefacts produced in FP reconstruction images. In experiments, these errors can occur due to several factors: LED array distance from the object plane, orientation and placement of the array, manufacturing errors in the array.

LED array distance from the object plane can be easily corrected by using adaptive correction method described in [88]. Here reconstruction is performed by varying the LED array distance and the position with least error in reconstruction is chosen as the final value for the LED array distance. The LEDs are usually assembled with a precision of 100 microns, which is found to be sufficient for FP recovery as described in later sections. This leaves the orientation and XY placement errors of the array as the main source.

Similar to LED array distance calibration, an error metric has been used to search for the optimal LED-position (illumination-angle). Simulated-annealing based search method has been proposed to find the position errors in the individual LEDs, which are then corrected to provide high-quality reconstruction [78,89]. This method, however, is very slow. It can also fail if there are errors in other system parameters, such as the pupil function. In the real-space ptychography the simulated-annealing method is always used to correct for any calibration errors and produce high-quality reconstructions [90].

A self-calibration method has been proposed to calibrate the positional errors in the bright-field illumination angles [91]. This algorithm depends on the fact that the Fourier transform of the recorded intensity image is the auto-correlation of the object's frequency spectrum multiplied by the pupil function. This produces two overlapping circles in the Fourier transform, which provides the position of the bright-field illumination angles. This can be used to calculate a geometrical transformation between the estimated and the calculated bright-field illumination angles. This transformation can be applied to dark-field illumination angles to correct for any errors caused due to the LED-array alignment errors. This method provides the fastest and most reliable correction for systematic errors in the LED positions [92].

2.2.5.3 Illumination variation

Variation in the intensity within different illumination angles can produce artefacts as described in later sections. This can be easily corrected by measuring the variations before performing the experiment as described in [92,93]. However, minor fluctuations within a single LED due to power fluctuations cannot be corrected using this method. It was observed that the LEDs in the commercial arrays produce stable intensity and the fluctuations produced are negligible. If this is not the case, an adaptive correction method has been proposed in [88]. In this method, an intensity correction factor is used for intensity update function. This intensity correction factor is updated at every iteration using a specialized metric. Similar to simulated annealing algorithms for LED position correction, this method also fails in presence of other system errors.

2.3 FP robustness analysis

In this section, several experimental system parameters that influence FP reconstruction are discussed.

2.3.1 Fourier space overlap requirement

Redundancy in the data acquired is the key to the robustness achieved in the ptychography reconstruction as mentioned previously. A simulation has been performed in [94] to demonstrate that a minimum overlap of 35% is required to achieve a good reconstruction as shown in Figure 2.4 (A). A similar analysis has been performed in the real-space ptychography [95], where a similar conclusion was achieved. A 30% overlap was suggested for high-speed imaging and 60% overlap was suggested for high-reconstruction quality. However, an explanation was not provided with respect to the particular values for overlap redundancy achieved in the simulation results.

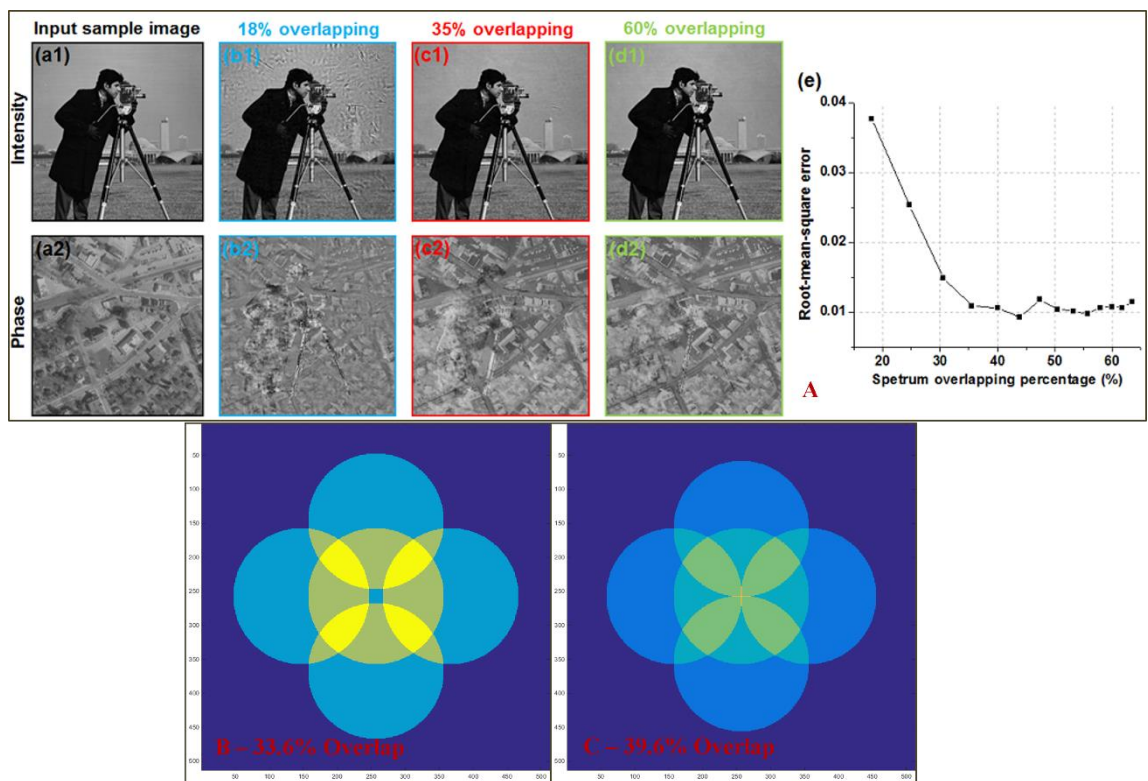


Figure 2.4 Overlap requirement in Fourier ptychography. Sub-image A is taken from [94].

An analysis of the Fourier spectrum was performed here to answer this question. In FP, for each point in Fourier space two values will be recovered - amplitude and phase; hence, to create a well-posed problem at-least two measurements are

required for each point. It is observed from geometry shown in Figure 2.4 (B) and (C) that when an overlap percentage of 39.6% is achieved, every point in the Fourier spectrum inside the region of interest is sampled at-least twice. From this, we can conclude that the ideal overlap percentage for simulations is 39.5%, which is closer to the achieved value in [94]. In Figure 2.4 (A), an ideal-data was used, i.e., noise, aberrations and calibration errors were not considered. In an experimental setup these errors contribute to additional variables in the model, hence an overlap percentage of around 60% is demonstrated to provide optimal performance [6].

2.3.2 Partial coherence limits

FP is a coherent imaging technique; however, a partially coherent light source such as an LED is conventionally used in the experiments. In FP, the points in the object need to be sufficiently close such that these two points are coherent to each other. The separation of these two points depends on the partial coherence of the light source. The partial coherence provided by the LEDs in commercial LED arrays is sufficient for FP and reduces speckle artefacts caused by highly coherent sources such as lasers. However, some limitations need to be considered before designing the experiment [63,96]. The sources of partial coherence in an LED are the size of the LED dye and the wavelength spread. The dye size and the distance of the array from the object determine the extent of the spatial-coherence according to Van-cittert Zernike theorem [7]: $l_c = 1.22 \lambda z / w$. Here l_c is the width in the object plane that is coherent, λ is the central wavelength, z is the distance from the LED array and w is the width of the LED dye. For commercial LEDs, this value is around 350 microns at an LED distance of 60mm. This implies that the large FoV acquired in an FP image needs to be segmented into sections smaller than 350 microns and processed independently. When the LED array is placed closer, this spatial-coherence limit is reduced; hence, an optimal distance is chosen according to these calculations.

The wavelength spread has two implications in the experiments; the temporal coherence length [97] and the chromatic aberration. Temporal

coherence length is calculated using $L = \sqrt{\frac{2 \ln(2)}{\pi n} \frac{\lambda^2}{\Delta \lambda}}$, where L is the source coherence length, n is the refractive index of the medium and $\Delta \lambda$ is the wavelength spread. For 30nm bandwidth light-source like the LEDs, this produces a coherence length of 10mm, which is much larger than the individual section processed in FP.

The chromatic aberration depends on the type of the lens used in the system; a singlet lens will have much higher chromatic aberration compared to an achromatic doublet lens. If the chromatic aberration is comparable to the DoF of the low-NA system then this degrades the image reconstruction. Advanced algorithms can be developed to address the chromatic aberration problem [68].

2.3.3 Illumination intensity fluctuations

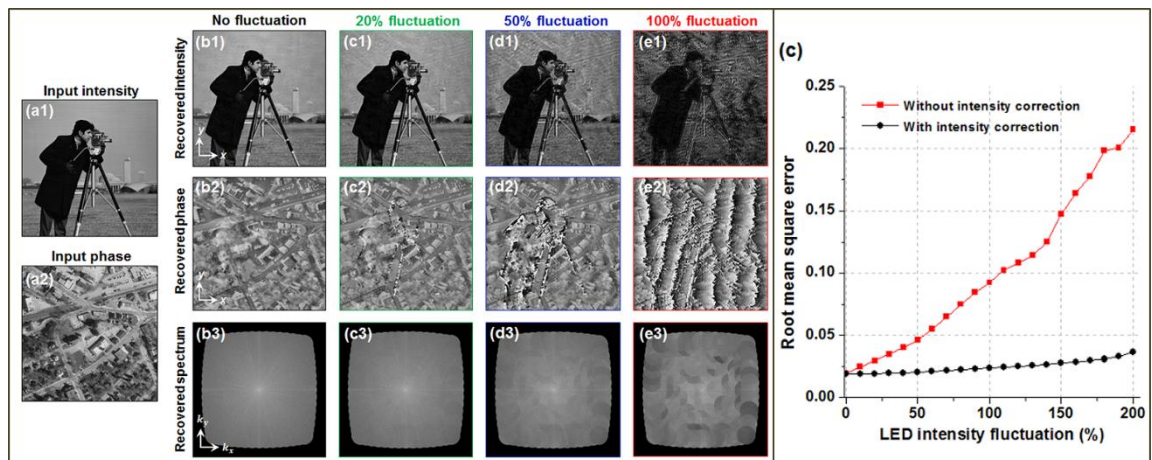


Figure 2.5 Illumination fluctuation errors. Taken from [88].

Since multiple light-sources are present in an LED array, they might produce varying illumination intensities between LEDs, which can be pre-calibrated. Each LED can also produce minor intensity fluctuations in time, which cannot be calibrated. These can cause artefacts in the reconstruction depending on the amount of fluctuations. Simulation were performed in [88] to study this. From Figure 2.5 it can be seen that intensity fluctuations between the LEDs under 20%

can produce acceptable results. An algorithm was proposed in [88] to correct these variations within the reconstruction procedure. In experiment, LED intensity variation between different LEDs in the array can be calibrated. In our experiments, the intensity fluctuations with time are found to be typically less than 10%, which is under the tolerance of FPM reconstruction as seen in the above figure.

2.3.4 Noise tolerance

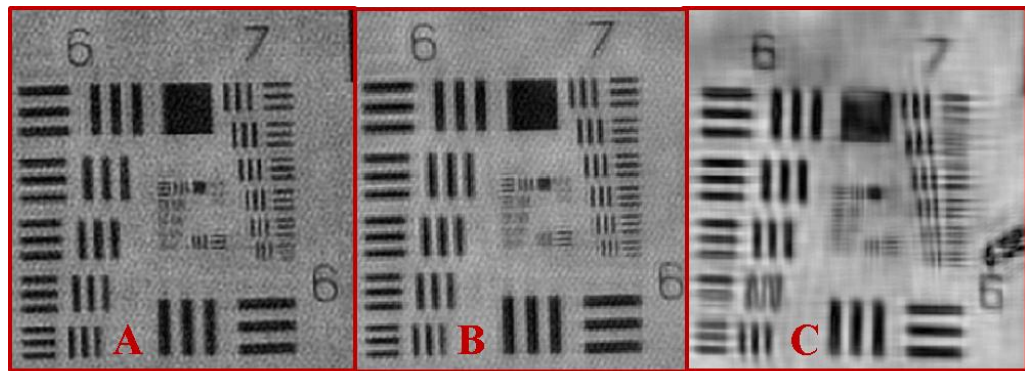


Figure 2.6 Experimental results demonstrating artefacts due to noise subtraction. (A) is reconstructed with no noise subtraction. (B) is reconstructed with offset calculated from the average. (C) is reconstructed with larger offset than the value calculated from the average.

Noise in the experimental images can be classified as photon shot-noise and the detector read noise. Shot-noise is independent of the detector system; it is determined by the number of photons recorded and follows Poisson distribution. The noise magnitude and the signal-to-noise ratio (SNR) in Poisson distribution are equal. The noise magnitude of photon shot noise equals to \sqrt{N} , where N is the number of photons recorded. Bright-field images contain most of the energy; hence, they have higher SNR and noise magnitude compared to the dark-field images. In LED-multiplexed illumination schemes [5,6] the bright-field LEDs shouldn't be mixed with the dark-field LEDs since the noise magnitude in bright-field images can overwhelm the signal in dark-field images. The detector read-noise is dependent on the electronics of the sensor and the temperature. It follows a Gaussian distribution and is independent of number of photons recorded. It

depends on the factors that can affect the detector read electronics, such as the heat generated during prolonged exposure times. In the commercial detectors, the detector read noise is much smaller compared to the photon shot-noise. Hence, it can be assumed that these systems are shot-noise limited. This analysis is described in detail in Chapter 5.

The quasi-Newton based FP algorithm [78] is found to be robust enough to recover good-quality images in the presence of Poisson and Gaussian noise described above. However, these images need to be subtracted by a scalar offset to minimize the noise in the images [98]. This offset is calculated by taking an average of the corners in an image [6]. However, this offset might need adjustment since a smaller offset value can result in noisy reconstruction as seen in image A of Figure 2.6 and a larger offset can result in low-contrast artefacts seen in image C. An adaptive de-noising method was proposed in [99] to provide robust noise subtraction depending on the sensor and the scene content.

2.3.5 LED position tolerances

LED positions determine the angle of illumination at the object plane, hence the frequency-shift in the object's Fourier plane. Information on these LED positions is assumed as *a priori* information in the recovery procedure, therefore significant errors in these positions result in artefacts in the recovered image as seen in Figure 2.7 (c2). The LED position errors can arise due to the errors in manufacturing the LED array or error in its orientation with-respect to the object. The systematic errors can be corrected using self-calibration methods [91,92], however, manufacturing errors are difficult to calibrate. Simulated-annealing has been implemented in such situations and found to improve the results [78,89]. The commercial LED boards are designed with around 100 microns precision, which is found to be tolerable for FP recovery process [92].

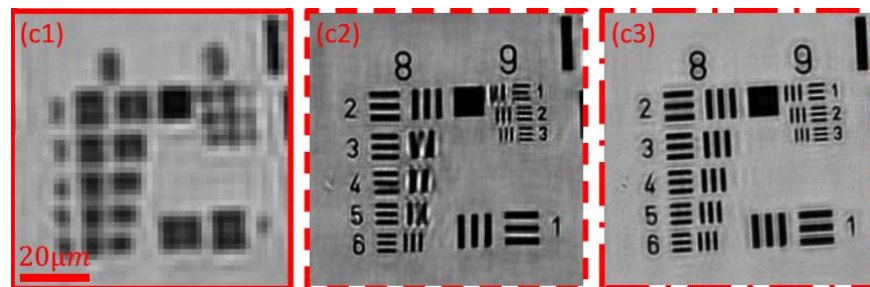


Figure 2.7 Reconstruction error due to LED position mismatch. (c1) low-resolution image. (c2) FPM reconstruction with LED position errors. (c3) FPM reconstruction with corrected LED positions. Image taken from [89].

LED position errors corresponding to the illumination angles in bright-field spatial frequencies produces low-frequency artefacts in the background images as discussed in [91]. High-frequency position errors distort specific groups as seen in Figure 2.7 (c2). In these results the LED position errors have been created by rotating the LED array around its centre resulting in less errors in the low-frequencies (central LED positions) and large errors in the high-frequencies (outer LED positions). Hence, artefacts are only observed in the high-frequency group numbers in the USAF resolution-chart image reconstruction.

2.3.6 Pupil errors

The pupil function in FP is the amplitude transfer function of a coherent imaging system. In an ideal imaging system, this pupil is a circle with a diameter of $\frac{2\pi}{\lambda} NA$ and has a constant amplitude and phase at all points [7]. In experimental systems, this pupil can have varying amplitude - caused by non-uniform transmission of the lens - and varying phase - caused due to the aberrations in the optics. These amplitude errors and aberrations can produce severe artefacts in the image recovery [78,88,100] as shown in Figure 2.8. Minor phase aberrations can be corrected by using embedded pupil recovery algorithm as discussed in the previous sections, however, major aberrations require either pre-calibration or adaptive methods.

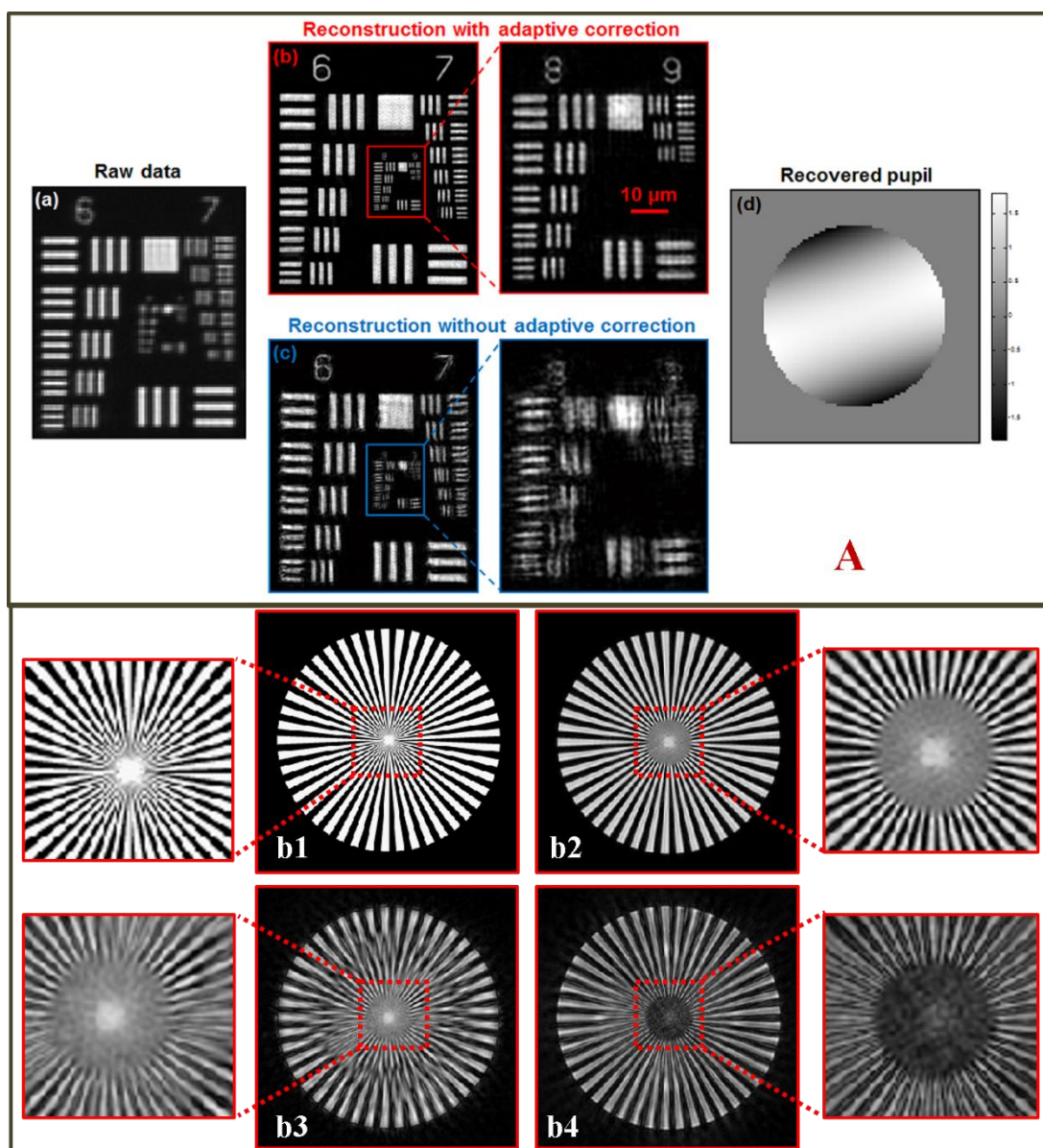


Figure 2.8 Reconstruction errors due to error in the estimated pupil. (A) Experimental results with error in pupil aberrations, taken from [88]. (b1-b4) Simulated results with error in pupil shape.

The amplitude errors can be caused due to errors in estimating the NA. In Figure 2.8 b1-b4, artefacts due to NA estimation error are shown. The input image is shown in b1 and the ideal reconstruction is shown in b2. In b3, the image is recovered with the pupil radius 0.8 times the actual value and in b4 1.2 times. When a smaller pupil size is used the high-frequency features are not reconstructed, whereas they are recovered with artefacts when large pupil size is used. This can be used as a guide to estimate the causes of artefacts in the image

recovery. In some situations, the pupil shape might not be a perfect circle, for e.g., when 3D printing is used or vignetting exists [63]. The aperture shape should be pre-calibrated or modified to correct for these errors.

2.3.7 LED sampling pattern

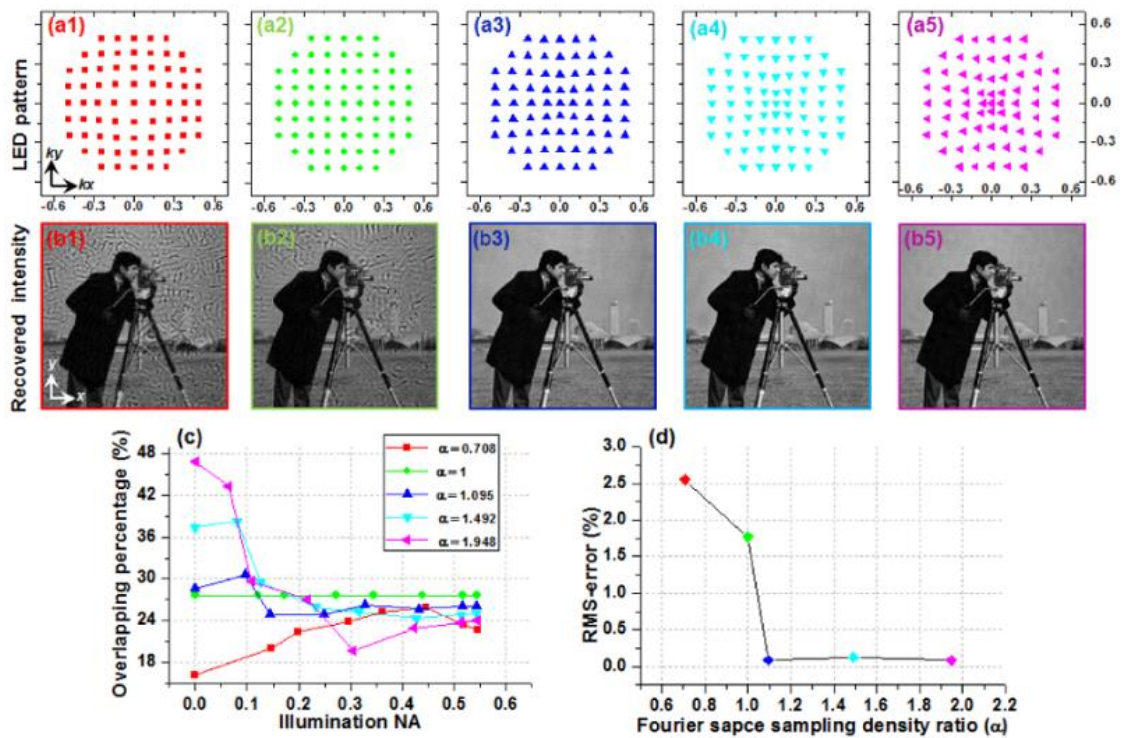


Figure 2.9 Simulation results with different sampling patterns. Taken from [101].

The shape of the LED array and their separation determines the sampling pattern in the Fourier space. As discussed previously there should be at-least 39% overlap in the frequencies captured by any two adjacent LEDs. When a commercial periodic grid array is used, the overlap between the LEDs increases towards higher-NA illumination. Instead a circular/dome shaped LED array can be designed where the overlap decreases when moved to the higher-NA illuminations [101]. It is discovered that using a higher-overlap in the low-NA illuminations produces better reconstruction as seen in Figure 2.9. This is due to the fact that low frequencies contain most of the energy, hence are crucial for a good image

quality. Higher redundancy in the low-frequency data provides superior quality reconstruction for low frequencies, hence better overall image quality.

It was also demonstrated that during the recovery procedure, the sequence of the illumination angles used in the processing determines the quality of the image reconstruction [101]. Highest quality reconstruction is achieved when the sequence is chosen with decreasing amount of total intensity in the images. In conventional recovery procedure a spiral with increasing illumination-NA is used, which satisfies this condition for most of the microscopy scenes. This is faster than sorting the images in their order of intensities, hence is widely used.

2.4 FP experimental configurations

This section describes a list of various experimental setups developed and implemented by FP research community. A brief description is provided for each technique along with its pros and cons. Due to an overwhelming number of papers with various experimental configuration being published in FP, this section is written as a guide to choose best possible setup for the experimental needs. Most of these setups can be modified to be implemented with our MA-FPM principle.

2.4.1 LED multiplexing with quasi-dome array

A custom array of LEDs in the shape of quasi-dome is described in [92] to synthesize 0.99 NA illumination. Bright LEDs used in the array and the quasi-dome shape solves the problem of low-illumination levels in the commercially purchased LED arrays. Quasi-dome shape solves the problem due to low dispersion angles of LEDs for higher NAs and the complex electronic circuit required for a hemispherical dome. The electronics also allows multiplexing LEDs which enables implementation of [5]. Due to their custom nature, this array is expensive. This array will be used in future with the setups discussed in this thesis as a continuation of this work. A quasi-dome type of LED array is the ideal choice for an FPM illumination due to the advantages of bright illumination and the LED multiplexing capabilities.

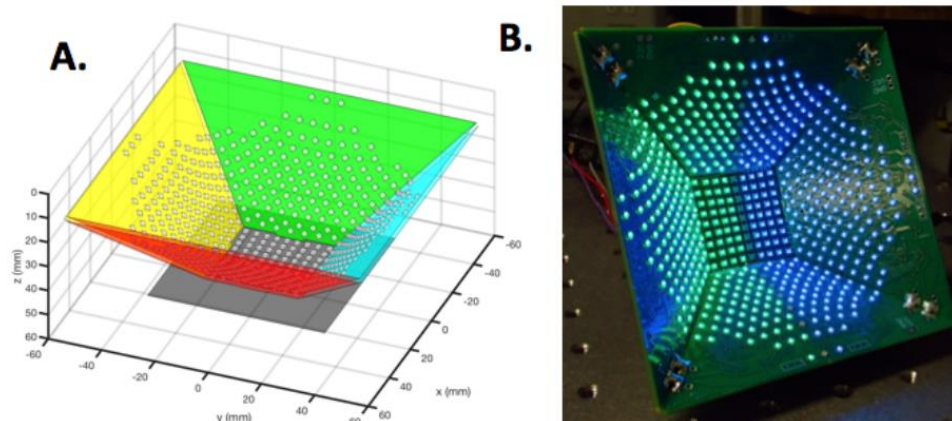


Figure 2.10 Quasi-dome LED array. Taken from [92].

2.4.2 Oil-immersion condenser

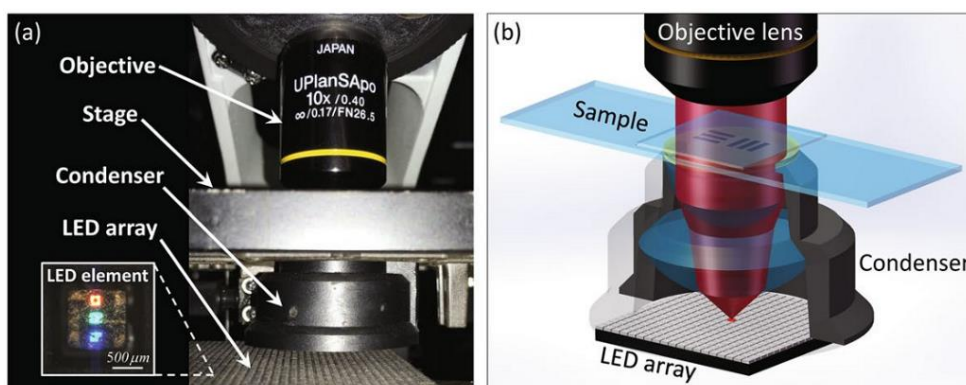


Figure 2.11 Resolution enhanced Fourier ptychography microscope. Taken from [93].

The LED array is placed under an oil-immersion condenser to achieve 1.2 illumination-NA [93]. This is the highest achieved illumination-NA ever reported in FPM. A planar LED array is used in this setup which suffers from low illumination intensities at higher NA angles. Hence, the data acquisition would be slower. A quasi-dome can be used instead of the planar LED array to improve the illumination intensities and the data acquisition speed. An oil immersion condenser is required to achieve extremely large illumination NA. Hence this setup results in very large SBP systems at the highest FPM resolution limits possible.

2.4.3 Aperture scanning

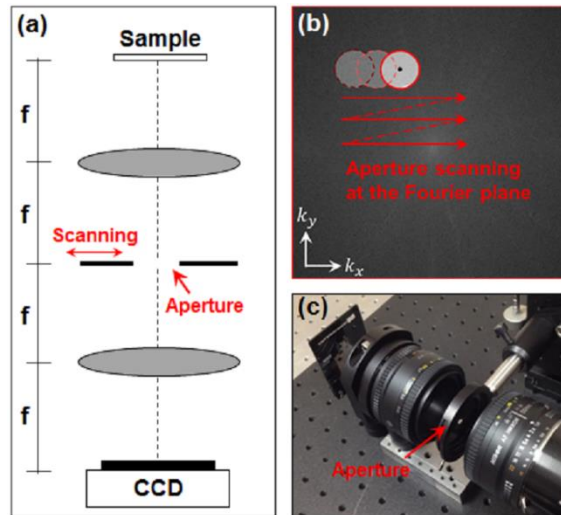


Figure 2.12 Aperture scanning Fourier ptychography setup. Taken from [63].

An FP configuration is reported where a high-NA objective is used and its pupil is cropped to generate a low-NA imaging system [63]. This pupil is then scanned to sample spatial-frequencies. Here an LED array is not required to change the illumination angles. This setup also relaxes the thin-object approximation for FP, hence enabling imaging of 3D objects. Due to the scanning nature this technique is slow compared to the LED systems. This also requires high-NA objectives. The theory of scanning the aperture is similar to MA-FPM.

2.4.4 Liquid crystal display (LCD) setup

This configuration is similar to the previous setup, except here the aperture is used in the pupil plane of the condenser [102]. The aperture is again scanned to provide illumination from different angles. The LCDs can be low-cost and can be switched very fast. This setup provides bright illumination due to the light-source used in microscopes but the illumination-NA is limited to the condenser-NA of the microscope. This provides a low-cost alternative to the LED array illumination in FP to modify an existing microscope. This illumination also results in stray light in the scene due to the low-contrast offered by the LCDs.

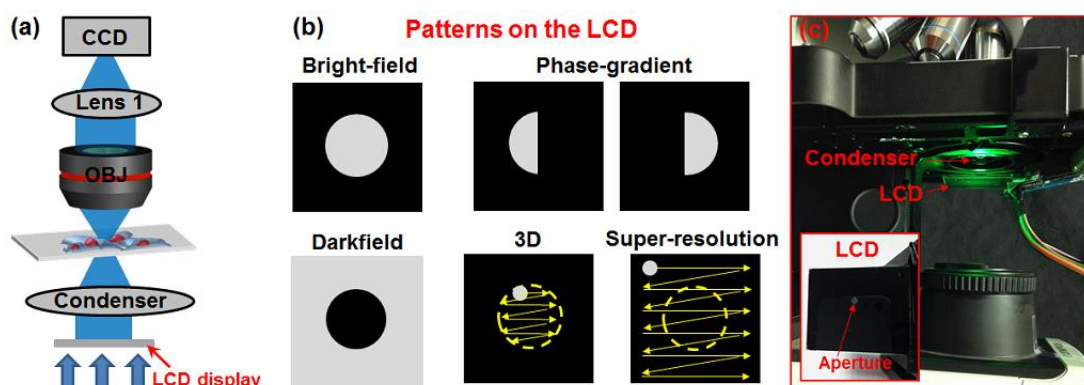


Figure 2.13 Liquid crystal display illumination engineering for FP. Taken from [102].

2.4.5 Laser scanning

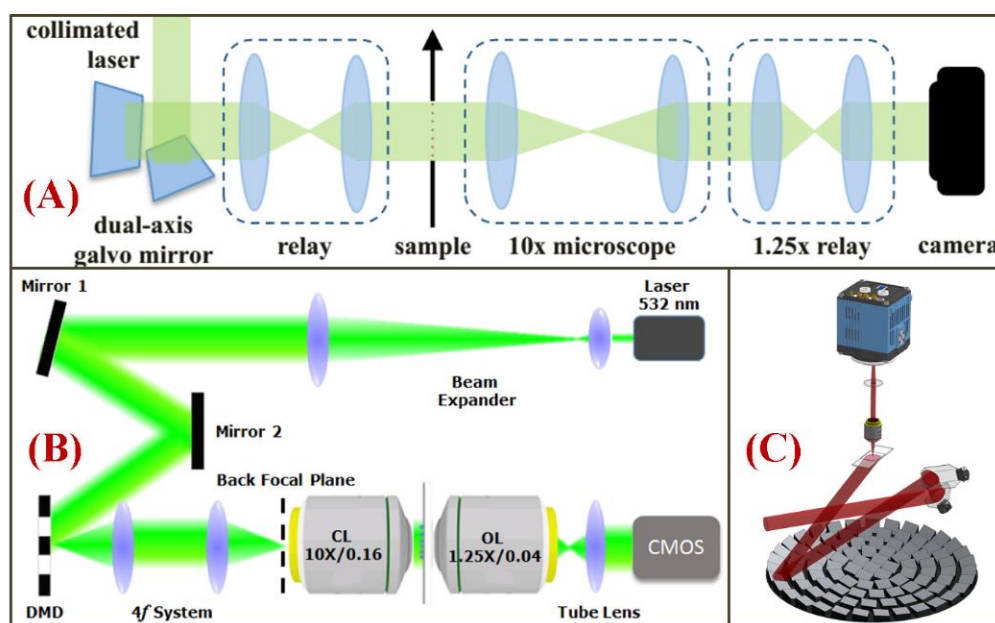


Figure 2.14 Laser scanning FP systems. (A) Taken from [91]. (B) Taken from [103]. (C) Taken from [104].

A laser is proposed as an illumination source to enable short exposure-times, especially for dark-field images. Three different setups have been reported for using laser illumination as shown in Figure 2.14. Setup (A) uses the simplest configuration using galvo mirrors to scan the illumination through a condenser.

This setup suffers from aberrations of the condenser lens, which require extensive calibration [91]. Setup (B) uses a DMD instead of galvos for scanning the illumination, again through a condenser lens. This suffers similar problems as setup (A) except a different scanning mechanism has been presented. In setup (C) the illumination is scanned using galvo mirrors but focused using an array of mirrors instead of a condenser lens, this provides less aberrations in the wavefront compared to (A) but still require pre-calibration of the system. Due to speckle from the laser, these setups suffer from artefacts in reconstruction. A laser illumination doesn't show any significant advantages over custom built LED arrays such as the quasi-dome described above. Hence, a custom-built LED array is recommended for FPM illumination.

2.4.6 Reflective FP setup

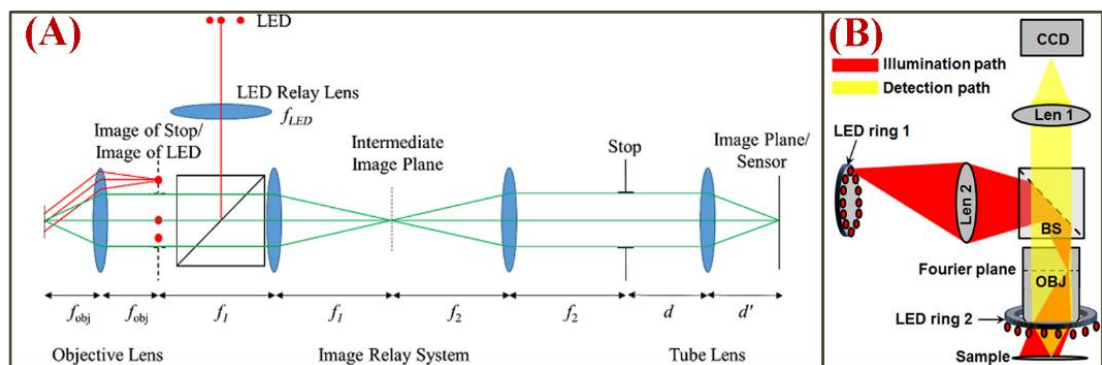


Figure 2.15 Reflective FP setups. (A) Taken from [105]. (B) Taken from [106].

FP can also be implemented for reflective samples such as electronics surfaces [106] or biological surfaces [105,107]. Two experimental configurations have been reported so far, as shown in Figure 2.15. Setup (A) requires a high-NA objective and a relay setup, where an aperture stop is introduced in the pupil plane to generate a low-NA system. The illumination NA in this system is limited to a maximum NA of the objective lens, hence the maximum achievable synthetic NA of the system is equal to the sum of the objective NA and the aperture stop NA. A circular led array is added around the objective lens in setup (B). Hence, setup (B) can be used with low-NA objectives and the maximum synthetic NA

achievable can be one plus the objective NA (in air). Setup (A) can be replicated easily compared to (B) which requires custom building of the LED array. MA-FPM can also be implemented in reflection using either of the following two configurations, which will be an interesting aspect to pursue in future. Reflective FP extends the application of FP to several new applications such as surface quality testing of electronics and retinal imaging [108]. Reflective biological samples often thick and suffer from scattering. This imposes additional variables to solve for in the recovery, hence making this application challenging.

2.4.7 3D FPM

A 3D FPM is reported in [64,66,109]. The experimental setup of 3D FPM is same as the 2D FPM; the only difference is in the reconstruction procedure. FPM assumes a thin-object approximation, which is relaxed in this approach by considering special models of diffraction. A multi-slice algorithm is developed to recover the 3D object. The MA-FPM setups reported in this thesis can be readily used to perform 3D FPM. This will be pursued in future work.

2.4.8 Raspberry Pi FP setup

A miniaturized FPM setup costing under £100 is being built using Raspberry Pi computer and camera - an open source platform for science projects. This is currently an active project proposed and supervised by me in our research group. This microscope is aimed to provide a low-cost product for digital pathology and haematology applications in low-income parts of the world. This can also be an extremely useful learning tool for FP research and computational imaging. We are currently investigating the possibilities of embedding the Raspberry cameras in our MA-FPM systems to reduce the cost. A camera and a Raspberry Pi Zero board can be bought for under £25 to build parallel data-acquisition systems. This can result in an MA-FPM system with 25 cameras costing under £1000, providing SBTP in gigapixels/second.

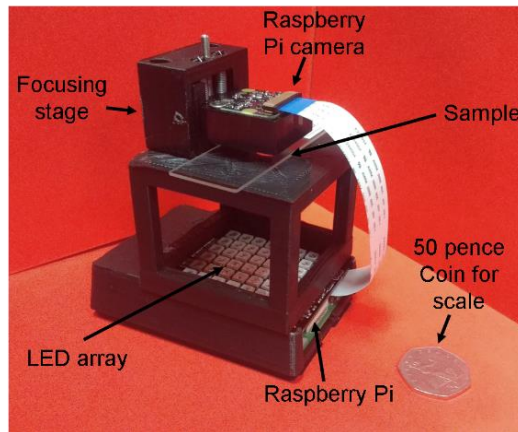


Figure 2.16 FP microscope using Raspberry pi hardware. Taken from [48].

2.4.9 Macroscopic FP with camera array

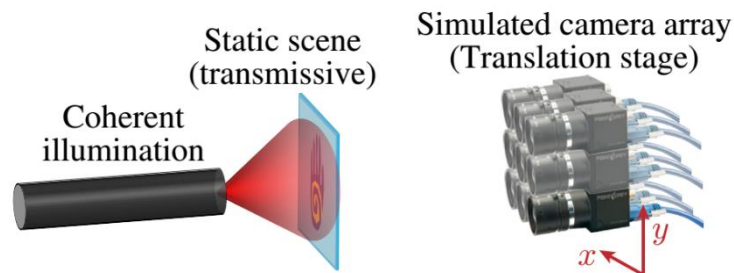


Figure 2.17 Macroscopic FP with camera array setup. Taken from [110].

A camera array setup for macroscopic FP imaging has been reported while the work in this thesis was being developed [110]. A periodic array of cameras (lens fixed to the sensor) was used in this setup. A similar technique where the aperture is scanned instead of using camera array was reported in [63]. The shift in the image due to shifting the camera is ignored in these setups. A smaller LED array is proposed to fill the frequencies between the cameras, similar to the proposal in this thesis. This model is only applicable for macroscopic imaging, i.e., it cannot be applied for microscopic imaging. This thesis deals exclusively with the microscopic implementation of the camera array configurations.

2.4.10 Single pixel FP

An FP setup using single-pixel imaging modality is proposed in [111]. Single-pixel imaging systems contain a photodiode (PD) instead of a detector. A series of known patterns are projected on the object and resultant sum of the object multiplied with the projected pattern is recorded by the PD. The PD intensity pattern is solved to recover the image [112]. Single pixel imaging is used in wavelengths where pixel arrays are expensive, such as in infrared. In this setup a PD array is used to simulate the aperture scanning method presented above [63]. This is an interesting setup for applying FP to extreme ultra-violet [39,40] or Infrared imaging where detectors are expensive.

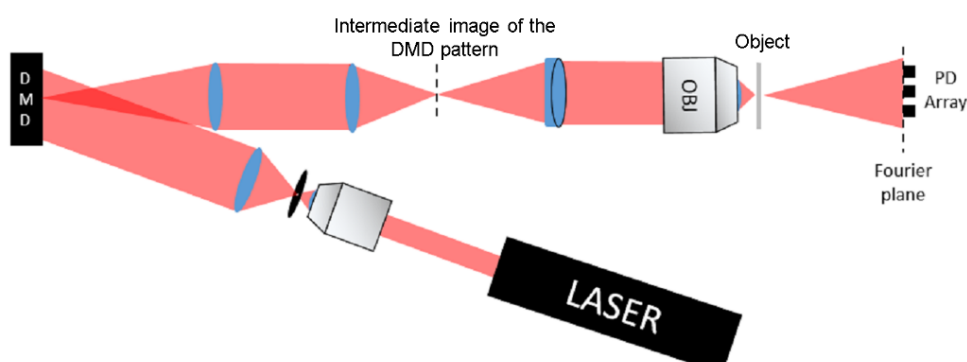


Figure 2.18 Single pixel FP setup. Taken from [111].

2.5 Summary

In this chapter, the theory behind FP was discussed and space-bandwidth-product terminology was defined. The FP recovery procedure was then demonstrated as a regularized optimization problem. Several optimization models for FP recovery were then discussed. It is concluded that the sequential quasi-Newton optimization method provides robust convergence with faster processing time and the amplitude-based cost function provides best representation of the forward model. A generalized FP-reconstruction algorithm is presented and LED/colour multiplexing concept was discussed along with its deviations in reconstruction

procedure compared to the generalized FP algorithm. There are few more variations of the FP reconstruction developed for specific applications such as sparsely sampling FP [94], adaptive noise-correction [99], 3D FPM with aperture scanning [63,113] and 3D FPM using thick sample approximations [64,109]. These are not discussed here due to the limited scope of this thesis. Later, algorithms for correcting errors in the experimental system were also discussed. Embedded pupil recovery algorithm is found to be the best method for correcting minor aberrations in the experimental setup and self-calibration algorithm is found to be the most efficient method for correcting LED position errors due to misalignment. Calibrating the illumination intensity variations experimentally is suggested as the best method; however, an automated algorithm was also discussed.

In section 3, the robustness of FP with several experimental parameters was discussed. The influence of the partial-coherence parameters and methods to calculate them for an experimental setup were described. The overlap requirement in FP was discussed and an explanation for this requirement was provided. The influence of the background noise subtraction was demonstrated with experimental results from this thesis. The importance of the LED array shape and the sequence of illuminations used in the reconstruction were discussed. It is concluded that a non-periodic array with high-dense sampling in the lower-NAs is preferred and the best sequence for processing is an outward spiral starting in the centre of the array.

In the last section, various FP experimental setups were described. This is provided as a guide to understand how the experimental setup configuration can influence the applications and the feasibility/advantages of MA-FPM work in this thesis being implemented in such configurations. 3D FPM and the quasi-dome with LED multiplexing is planned to be implemented in the near future with the experimental setup developed in this work. It is proposed that an MA-FPM setup using Raspberry Pi hardware can provide low-cost high-throughput gigapixel imaging system.

Chapter 3 Multi-Aperture FPM

This chapter introduces the Multi-Aperture FPM (MA-FPM) concept and theory. Design parameters for an MA-FPM setup are discussed. A Fresnel propagation based reconstruction algorithm is proposed for MA-FPM reconstruction. An FPM reconstruction algorithm based on Fresnel propagations is described along with validation on experimental data. Differences of the Fresnel propagations based algorithm and Fraunhofer propagations based algorithm are discussed. The sampling criterion for the Fresnel algorithm is also discussed.

3.1 MA-FPM Theory

Spatial-frequencies in FP are sampled by exploiting the Ewald sphere theory as discussed in the previous chapter. This can also be understood with the help of the diffraction orders of a periodic grating as seen in Figure 3.1. In this figure it is assumed that the object is a Ronchi grating [114]. This grating object splits the collimated illumination into its diffraction orders [115]. These diffraction orders contain distinct information about the square grating object (Ronchi grating). This is equivalent to splitting a square wave into its sinusoidal components according to the Fourier theory [116]. To reconstruct the square wave from these sinusoids, the amplitude and phase information of all the sinusoidal components is required. In a conventional optical system, these diffraction orders are collected by the objective lens to form an image. The highest-diffraction order collected by the system depends on the collection angle of the lens (depicted as the shaded area in Figure 3.1 (a) and (b)). This angle corresponds to the Numerical aperture (NA) of the optical system. Hence, higher diffraction orders are not recorded, limiting the sharpness of the square grating image. According to the theory of diffraction, the centre of the diffraction orders lies in the direction of the angle of illumination [115]. This is exploited in FP by changing illumination angles to shift

the diffraction pattern (seen by green arrow in Figure 3.1 (a)) into the collection angle of the objective. Spatial-frequencies collected from these diffraction orders can be seen in the object's Fourier space depicted in Figure 3.1 (c).

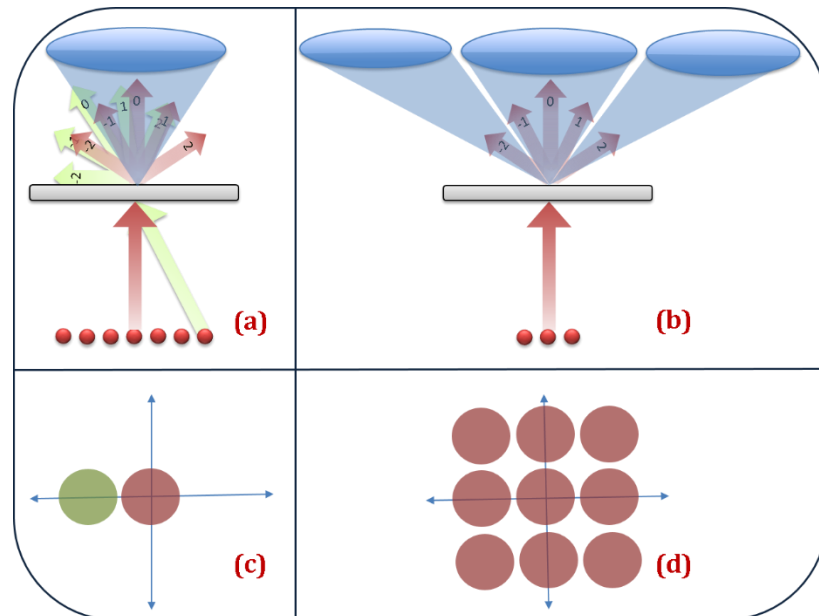


Figure 3.1 MA-FPM theory depiction.

In Multi-Aperture FPM, to collect these higher diffraction orders, an array of objective lenses is proposed as shown in Figure 3.1 (b). These individual lenses have their own collection angle, distinct from each other, sampling a distinct set of the spatial-frequencies as seen in the object's Fourier plane shown in Figure 3.1 (d). This increases the bandwidth of frequencies captured in a single snapshot as seen in the figure. However, the gaps between the lenses leave empty spaces in the recorded Fourier space. These are filled by using an LED array to shift the missing spatial-frequencies inside the pass-band of the multi-aperture synthetic objective. This also provides the redundancy required in the FP data as explained in the previous chapter. Thus, adding multiple objective lenses and detectors improves the speed of the data-acquisition, which is not possible with the existing microscopy methods.

The conventional method for recording the higher diffraction orders is to increase the collection angle of the objective lens, i.e., using a higher NA

objective. This introduces several problems such as higher aberrations, requiring well-corrected objective lenses. It also imposes several restrictions such as short working distance, narrow DoF and small FoV. In MA-FPM, a synthetic objective is created using low-NA optics which circumvents these shortcomings. In conventional FPM experiments, a commercial objective lens is used. Despite providing low-NA, these are usually bulky and have less freedom due to the specific application design. Instead, an achromatic doublet lens is proposed here as the objective in MA-FPM experimental design, which can provide sufficient image quality for low-NA's up to 0.15NA. This can provide extremely long working distances - in experiment, we have achieved 57mm working distance. This also allows dense packing of the objective lenses, providing better speeds.

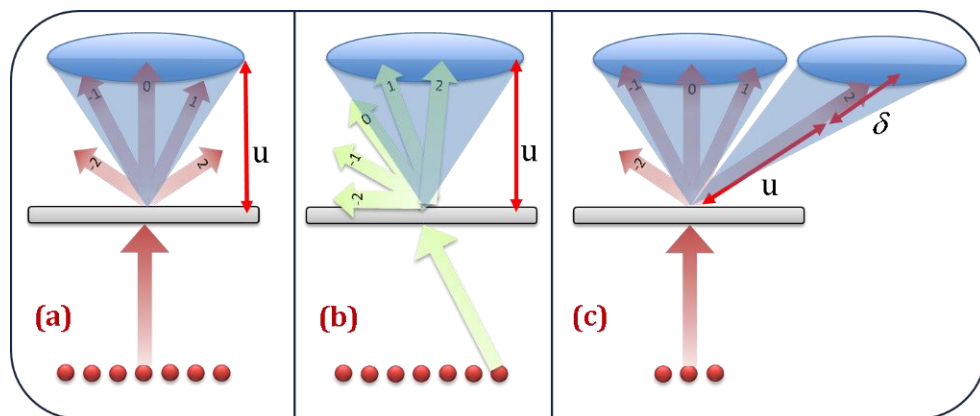


Figure 3.2 Sampling differences between FPM and MA-FPM. (a) FPM frequencies sampling for on-axis illumination. (b) FPM frequencies sampling for off-axis illumination. (c) MA-FPM frequencies sampling for on-axis lens and off-axis lens for on-axis illumination.

As described MA-FPM creates a synthetic objective of higher NA with respect to the individual objective lenses. In FPM, the resolution improvement is achieved by simulating synthetic high NA illumination; therefore, the maximum resolution achieved by an FPM system is limited to the maximum illumination NA possible (i.e., one in air). For example, a 0.1NA objective lens in FPM can provide a theoretical maximum of 1.1NA in air. With MA-FPM, this limit can be pushed further; the theoretical maximum can be two in air, when a synthetic objective with NA 1 is created using several 0.1NA objective lenses. Hence, MA-FPM

configuration can provide the highest SBP and SBTP possible among existing microscopy methods.

The path travelled by the light in an imaging system can describe the imaging properties of that imaging system. In FPM, the path travelled by the light from the object to the lens plane can provide insight into the object's Fourier spectrum sampled by that system. Hence, the light path in an FPM system for on-axis and off-axis illumination is compared to the light path in an MA-FPM system on-axis lens and off-axis lens as seen in Figure 3.2. In FP, the path travelled by the shifted higher diffraction order is same as the path travelled by the central diffraction orders without the shifted illumination as seen in Figure 3.2 (a) and (b). Hence, this is equivalent to a simple shift in the object's Fourier space. However, in MA-FPM the higher-diffraction orders travel a slightly different path compared to the central orders as seen in Figure 3.2 (c). Therefore, this cannot be treated as a simple shift of the frequencies in the Fourier plane. Instead, this can be treated as shifting the lens position in the lens plane of the setup. Fraunhofer propagations can only be used for this case if the objective lenses are present in the far-field of the object diffraction pattern as demonstrated in [63]. Fresnel propagations should be used in near-field situations, which is the case for microscopy [39,100,117-119]. Hence, we propose an algorithm using Fresnel propagations that can be used in MA-FPM applications. In our algorithm, we have made some assumptions and relaxations to improve its computational efficiency. These are discussed in the following sections.

3.1.1 MA-FPM design parameters

MA-FPM experimental design schematics using two lenses and detectors are shown in Figure 3.3. The optical axis of an MA-FPM system is defined as the line passing through the centre of the central objective lens and perpendicular to the lens plane (P_3), the detector plane (P_4), the object plane (P_2) and the led-array plane (P_1). Hence, the imaging system (objective lens and a detector) present in the centre of the array is termed as on-axis imaging system and rest are termed as off-axis imaging systems.

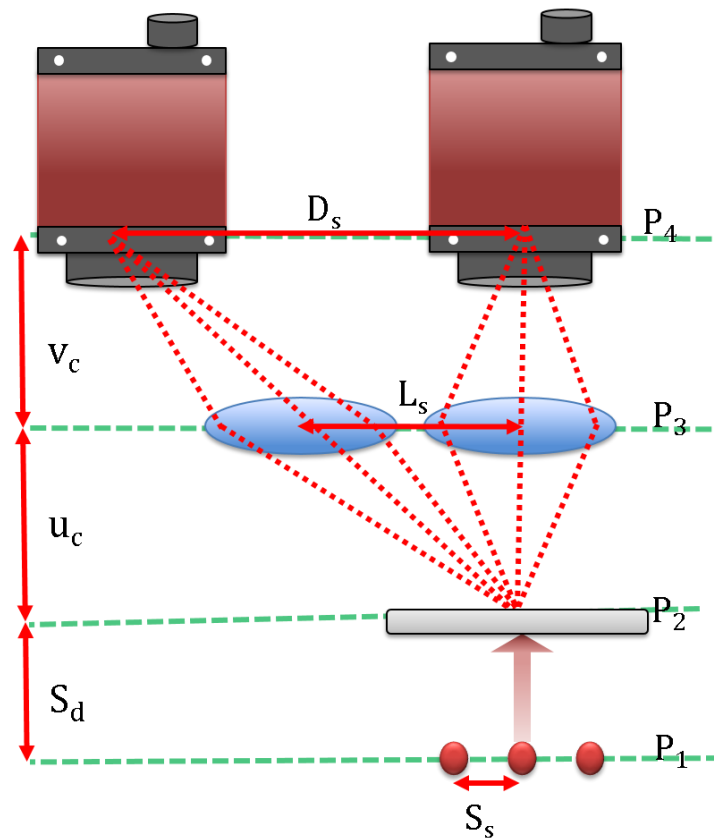


Figure 3.3 MA-FPM experimental design. P_1 - LED array plane. P_2 - Object plane. P_3 - lens array plane. P_4 - Detector array plane. S_s - Separation between LEDs in the array. S_d - Distance between the LED array plane and the object plane. u_c - Distance between the object plane and the lens array plane. v_c - Distance between the lens array plane and the detector array plane. L_s - Centre to centre distance between the lenses in the array. D_s - Centre to centre distance between the detectors in the array.

The magnification of an MA-FPM system is defined as the magnification of the on-axis imaging system m . Imaging configurations of the off-axis systems are designed to produce same magnification as the on-axis system. In the current work, we chose all the objective lenses with same focal length f and the aperture radius r . Using objectives with varying focal lengths can create several combinations, hence making the designs interesting and complex. We chose identical lenses for all the imaging systems for simplicity. The most crucial parameter for an MA-FPM system design is the separation of the objective lenses L_s . A closest packing and highest speed is achieved when these are placed next to each other, but this requires a large number of off-axis imaging systems when aimed for large improvements in the synthetic NA. In situations, where only a specific factor of speed reduction is

required for a targeted synthetic NA, a small number of off-axis imaging system and LEDs can be used to achieve this balance. For e.g., if 15x15 LEDs are required to improve the NA by five times and a nine times reduction in data acquisition time is sufficient, then a 3x3 array of objective lenses with a 5x5 LED array can be implemented. The off-axis lens position is calculated such that its centre matches the shift provided by the fifth LED from the centre (i.e., 13th from the first) in the 15x15 array. We have implemented this configuration in the experimental validation described in the next chapter.

The positions of the off-axis objectives and detectors are calculated using the parameters defined so far. The off-axis objectives are placed in the objective lens plane P_3 same as the on-axis objective, but their centre is translated by L_s from the MA-FPM optical axis. The off-axis detectors are placed in the detector plane DP same as the on-axis detector, but their centre is translated by $(1+m)L_s$ from the MA-FPM optical axis. The off-axis objectives and detectors can be theoretically placed in a plane different to the P_3 and P_4 respectively. This configuration is chosen to match the experiment in the next chapter where a single objective lens and detector are translated to emulate an MA-FPM system. A robust optical configuration for a multiple cameras setup is discussed in chapter 5 and an experimental setup with multiple cameras is also discussed.

3.2 Fresnel propagations based FPM reconstruction

In the previous section, it was stated that a Fresnel propagation based algorithm provides more precise modelling of an MA-FPM system compared to Fraunhofer propagations. In this section a Fresnel propagation based reconstruction algorithm is proposed to process a conventional FPM dataset. It is validated with experimentally recorded data and its robustness against a conventional Fraunhofer based algorithm is discussed. Adaption of this algorithm specifically for MA-FPM application is described in the next chapter.

3.2.1 Fresnel propagation algorithm

The Fresnel propagation algorithm follows mostly the same procedure as the conventional Fraunhofer propagation based algorithm described in section 2.2.2. The major difference is that the propagation of the complex fields will be between the object plane, the lens plane and the detector plane instead of the Fourier plane and the detector plane. Moreover, the propagations here are based on the Fresnel diffraction integrals discussed in the next sub-section.

The reconstruction algorithm starts by a high-resolution estimate of the object, which is propagated onto the lens plane using Fresnel propagations. In this plane, the complex field is filtered using a pupil function corresponding to the angle of illumination. The filtered complex field is then propagated to the detector plane using Fresnel propagations. The amplitude of the complex field in this plane is updated using the experimentally recorded image. The updated complex field is then propagated back to the lens plane and the initial high-resolution complex field of the object in the lens plane is then updated. This updated complex field in the lens plane is again filtered for the next illumination angle and the entire process is repeated until all the illumination angles are used. The final high-resolution complex field in the lens plane is propagated back to the object plane to recover a high-resolution image of the object. The error in this image is calculated to check if the solution is converged. If the solution is not converged then the complete process is repeated, else the process is terminated and the high-resolution image obtained at the end is the final reconstruction.

As it can be observed in the flow chart of the algorithm, the reconstruction process starts in the object plane. Hence, the initial estimate is required in the object plane instead of the frequency plane in the conventional algorithm. This is another key difference compared to the conventional FPM reconstruction process. Hence, the initial estimate generation differs in these two methods. In conventional reconstruction method, the initial high-resolution object estimate is obtained by zero padding the Fourier transform of the low-NA image from the central bright-field LED. In Fresnel method, the low-NA image is interpolated to the size of the high-resolution image. This is then multiplied by the illumination phase profile

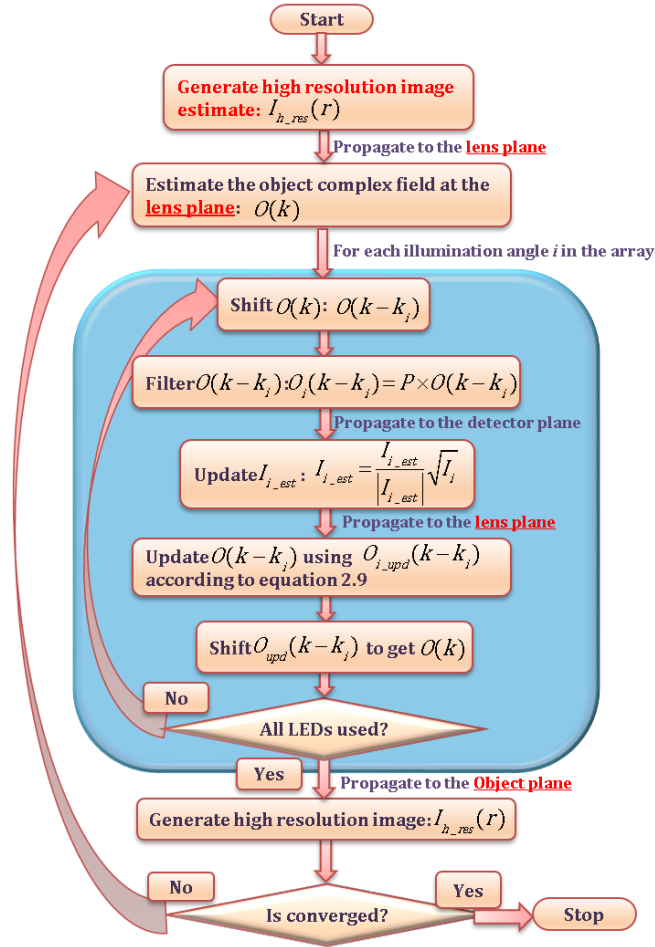


Figure 3.4 Fresnel propagation based reconstruction algorithm.

and propagated to the lens plane (equivalent to performing Fourier transform in the conventional method) to get the estimate of the high-resolution complex field in the lens plane. Also at the end of the iteration, the complex field in the lens plane is propagated back to the object plane before determining the convergence criteria. This new initial estimate step is especially important in MA-FPM reconstruction where multiple lenses are present because it incorporates the additional path distances described in Figure 3.2. Here the pupil shifts due to the changing illumination angles are calculated in the lens plane instead of the Fourier plane. Rest of the procedure remains identical to the conventional reconstruction method. The differences of the Fresnel propagation algorithm compared to the conventional method described in chapter 2 are highlighted in red colour in the flowchart shown in Figure 3.4.

3.2.2 Field propagation using Fresnel diffraction integral

Propagation of light between two planes is calculated using Kirchoff's diffraction integrals [7,115]. This integral is simplified by Fresnel approximations, which is widely used due to its speed and accuracy. Angular spectrum propagations are also used to propagate the optical fields. In experimental reconstructions, these propagations are performed in a computer. In a computer, the optical field is described by a discretized matrix. The physical extent of the optical field depends on the bin size (pixel size) multiplied by the total extent of this matrix. In optical field propagations using Angular spectrum propagation, the pixel size of the matrix remains constant between the propagated planes. Hence, the total extent of the complex field sampled remains constant in the plane where the optical field is propagated to. This is ideal in situations such as refocusing the optical field, but it is not suitable when the optical field needs to be calculated in a smaller/larger area. This is often the case, the lens plane is usually much larger compared to the object plane. The Fresnel propagations using Fourier transform approximations as described below vary the pixel size between the propagated planes. Hence Angular spectrum is not chosen, instead a Fresnel approximated diffraction integral is used in this work. This is explained in this sub-section, along with the approximations made for the off-axis cases in MA-FPM systems. Sampling requirement in Fresnel propagations is discussed along with pixel-size calculation.

Fresnel approximated diffraction integral:

Kirchoff's diffraction integral with Fresnel approximation can be written as [7]:

$$U(x, y) = \frac{e^{jkz}}{j\lambda z} \iint_{-\infty}^{\infty} \{U(\xi, \eta) e^{j\frac{k}{2z}((x-\xi)^2 + (y-\eta)^2)}\} d\xi d\eta . \quad (3.1)$$

This can be rewritten in the following form:

$$U(x, y) = \frac{e^{jkz}}{j\lambda z} e^{j\frac{k}{2z}(x^2 + y^2)} \iint_{-\infty}^{\infty} \{U(\xi, \eta) e^{j\frac{k}{2z}(\xi^2 + \eta^2)} e^{-j\frac{2\pi}{\lambda z}(x\xi + y\eta)}\} d\xi d\eta , \quad (3.2)$$

which can be recognized as the Fourier transform form of the integral as shown below:

$$U(x, y) = e^{j\frac{k}{2z}(x^2 + y^2)} \mathbb{F}\{U(\xi, \eta)e^{j\frac{k}{2z}(\xi^2 + \eta^2)}\}. \quad (3.3)$$

Here, $\frac{e^{jkz}}{j\lambda z}$ in the front is a constant and does not influence the complex field distribution being calculated. Hence this term is usually ignored for simplicity.

Propagation of the complex field $U(\xi, \eta)$ begins by multiplying it with a quadratic phase factor $e^{j\frac{k}{2z}(\xi^2 + \eta^2)}$ as seen in the above equation. This resultant product is then Fourier transformed. The resultant Fourier transform should be multiplied by another quadratic phase factor $e^{j\frac{k}{2z}(x^2 + y^2)}$ as seen in the above equation. The resultant product is the required propagated complex field $U(x, y)$ in the new plane.

In this Fresnel propagation integral, the quadratic phase multiplied in the initial and final planes must be sampled according to the Nyquist criterion to avoid aliasing. The sampling criteria in the Fresnel propagation integrals is given as follows [118]:

$$d < \frac{\lambda z}{2(x_{\max} + h_{\max})}. \quad (3.4)$$

Where, δ is the pixel period, λ is the wavelength, z is the separation between the planes, ξ_{\max} and η_{\max} are the maximum extensions of the complex field in transverse directions. This Fresnel diffraction field propagation method is applied to field propagation in the flow chart shown in Figure 3.4 and the resulting propagation equations are derived in the following sub-sections.

Field propagation from the object to the lens plane:

Fresnel propagation in the form of Fourier transform described above is implemented as described to propagate the complex field of light between different planes. The complex field in the object plane is defined as $O(x, y)$. The lens plane complex-field $L(\xi, \eta)$ is then calculated as:

$$L(\xi, \eta) = e^{j\frac{k}{2u}(\xi^2 + \eta^2)} \mathbb{F}\{O(x, y)e^{j\frac{k}{2u}(x^2 + y^2)}\}. \quad (3.5)$$

Where, u is the propagation distance from the object plane to the lens plane, k is the wavenumber, (x, y) are coordinates in the object plane and (ξ, η) are coordinates in the lens plane.

When multiplying the quadratic phase factor, the Nyquist sampling criteria stated above must be followed. From equation 3.4, for typical experimental conditions it was observed that the sampling criterion is always satisfied. This is because the pixel size in the object plane is always very small. This is because the pixel size in this plane is determined by the required Nyquist sampling criterion for the synthetic high-NA. In the experimental setup described in the next chapter, it can be calculated that the pixel period in the object plane should be less than 10 microns, which is easily satisfied by the MA-FPM setup since the pixel size in the object plane is around 0.2 microns.

Field Propagation from the lens plane to the detector plane:

Before propagating the complex field in the lens plane to the detector plane, it needs to be filtered with the lens transfer function [7], given as:

$$LTF = P \times e^{j\frac{-k}{2f}(\xi^2 + \eta^2)}, \quad (3.6)$$

where, P is the amplitude of the lens transmission and the quadratic phase factor corresponds to the phase modulation due to the lens. Hence, the complex field in the detector plane can be calculated as:

$$D(\alpha, \beta) = e^{j\frac{k}{2v}(\alpha^2 + \beta^2)} \mathbb{F}\{P \times L(\xi, \eta) e^{j\frac{k}{2v}(\xi^2 + \eta^2)} e^{j\frac{-k}{2f}(\xi^2 + \eta^2)}\}, \quad (3.7)$$

where, v is the propagation distance from the lens plane to the detector plane, f is the focal length of the lens, k is the wavenumber and (α, β) are coordinates in the detector plane.

In the lens plane several quadratic phase factors are multiplied, i.e., from the first Fresnel propagation, the lens transfer function and the Fresnel propagation to the detector plane. The sampling criterion needs to be considered for the resultant phase sum of these factors:

$$PhaSum = e^{j\frac{k}{2u}(\xi^2 + \eta^2)} e^{j\frac{k}{2v}(\xi^2 + \eta^2)} e^{j\frac{-k}{2f}(\xi^2 + \eta^2)}. \quad (3.8)$$

By replacing $1/f$ in the above equation using lens maker's formula [7,115], it can be observed that the resultant phase sum is zero. Hence, there is no requirement for sampling phase in this plane.

Backward field propagation from the detector plane to the lens plane:

Once the amplitude is updated in the detector plane from the recorded amplitude values, the complex field is then propagated back to the lens plane. This is written as:

$$L'(\xi, \eta) = e^{-j\frac{k}{2v}(\xi^2 + \eta^2)} \mathbb{F}\{D'(\alpha, \beta) e^{-j\frac{k}{2v}(\alpha^2 + \beta^2)}\}. \quad (3.9)$$

When the complex field in the detector plane $D(\alpha, \beta)$ is updated, the phase is kept constant. Hence, in the detector plane between the forward and backward propagation, the resultant sum of the phase multiplied is zero. Therefore, the sampling criterion is also satisfied in this plane.

Backward field propagation from the lens plane to the object plane:

After all the illumination angles are updated in the lens plane, the complex field in then propagated back to the object plane as follows:

$$O'(x, y) = e^{-j\frac{k}{2u}(x^2+y^2)} \mathbb{F}\{L'(\xi, \eta) e^{-j\frac{k}{2u}(\xi^2+\eta^2)} e^{j\frac{k}{2f}(\xi^2+\eta^2)}\}, \quad (3.10)$$

As it can be observed the complex conjugates are multiplied in the backward propagation and the resultant phase sum is again zero in the lens plane. In the object plane, however, the phase factor multiplied in the first step is removed by multiplying it with its complex conjugate as seen in the above equation. Hence, the sampling criteria required for Fresnel propagations is satisfied in all these conditions.

It should be noted that any aberration corrections in the reconstruction procedure will be added to the lens transfer function described above. The aberrations phase is slowly moving and does not wrap as much as the quadratic phase factors in the Fresnel propagations. Therefore, sampling is not a problem for aberration correction. Like the Fraunhofer method, in this method the shift of the complex field due to changing illumination is treated as shifting the pupil. The changing illumination is given by a tilt phase in the object plane, which results in shifted complex field according to the Fourier theory. Since the Fresnel integral is written in the Fourier transform form, the impact of the changing illumination angle in the reconstruction procedure stays same.

3.2.2.1 Off-axis lens system field propagation

In the above analysis, only an on-axis system was considered. The lens plane approximation described previously needs to be re-calculated for an off-axis system. The only difference for an off-axis system is the lens transfer function. This is written as:

$$LTF = P \times e^{j\frac{-k}{2f}((\xi-d_\xi)^2+(\eta-d_\eta)^2)}, \quad (3.11)$$

where, d_ξ and d_η are the lens coordinates. When expanded, this equation can be written as:

$$LTF = P \times e^{j\frac{-k}{2f}(\xi^2 + \eta^2)} e^{j\frac{-k}{2f}(d_\xi^2 + d_\eta^2)} e^{j\frac{k}{2f}(2\xi d_\xi + 2\eta d_\eta)} \quad (3.12)$$

Here, the first quadratic term is same as the on-axis lens phase term, the second term is a constant and the third term is a tilt factor. The resultant sum of phase in the lens plane will be simply the tilt term from the above equation. This tilt term when removed, shifts the coordinates of the image in the detector plane to the origin. This implies that the resultant sum of the phase in the lens plane is again zero and this results in a fast calculation of the Fresnel propagation, which otherwise can be very slow. The rest of the propagations remains same for the off-axis system.

3.2.3 Pupil shift calculations

The pupil diameter and the pupil shifts due to the changing illumination angles are crucial parameters for successful FPM recovery as discussed in the previous chapter. Here the pupil shift calculation methods for both conventional FPM and Fresnel FPM recovery methods are presented. The Fresnel method differs from Fraunhofer method by one crucial step, the quadratic phase factor in propagating the field to the lens plane. Hence a comparison between the pupil shifts is made to study their further differences. Since the complex field is discretized in a computer, the pixel size (discretization step) should be known. Also, the pixel size value changes between different planes in the reconstruction process. Hence, these calculations are provided below for both Fresnel and Fraunhofer method.

Pixel size calculations

In Fresnel propagation, the pixel size changes between the propagated planes. It depends on the distance propagated and total width of the plane where the optical field is propagated from. Hence, it is important to calculate the pixel size for each

plane in the algorithm. In a Fresnel propagation, the pixel pitch in the plane where the field is being propagated to is given as [120]:

$$\delta = \frac{\lambda z}{W}, \quad (3.13)$$

where, w is the total width of the source complex field plane, z is the propagating distance and λ is the wavelength.

To calculate the pupil shifts, the pixel size in the lens plane is needed. From the previous equation, the pixel pitch in the lens plane δ_l is given as:

$$\delta_l = \frac{\lambda u}{\delta_o D}, \quad (3.14)$$

where, u is the distance between the object plane and the lens plane (or focal length of the objective lens in a 4f system), δ_o is the pixel size in the object plane and D is the object matrix dimension. The δ_o can be calculated from the detector pixel size δ_d as: $\delta_d / (M * R_f)$. Here M is the system magnification and R_f is the resizing factor from the low-resolution image to the high-resolution image.

In Fraunhofer based conventional FPM recovery procedure, the pixel size in the Fourier plane δ_f can be calculated as:

$$\delta_f = \frac{2\pi}{\delta_o D}. \quad (3.15)$$

Here, it can be observed that the pixel size is independent of the propagation distance u , since the propagation distance is always infinity. The pixel size in the detector plane will be same as δ_o if the matrix size is kept constant. However, the detector pixel size is usually much larger due to the low-NA imaging system. Hence, the matrix size is usually cropped (by R_f) in Fourier transforms (in both methods) to increase the detector pixel size. Hence the pixel pitch in the Fourier plane can also be written as:

$$\delta_F = \frac{2\pi M}{\delta_d D_d}, \quad (3.16)$$

It can be observed that the D_d (matrix size of the low-NA image in the detector plane) is smaller by R_f times compared to D and the pixel size in the detector plane is larger by R_f times, which keeps the pixel pitch constant as required. In experiment, the D_d is the size of the image segment that is processed at a time, which is chosen by the user such that it satisfies the partial coherent requirements described in section 2.3.2. The resizing factor R_f is calculated from the object pixel size δ_o and the effective detector pixel size δ_d / M such that δ_o provides Nyquist sampling for the high-resolution reconstructed image.

Fresnel propagation method

In Fresnel method the pupil function is applied in the lens plane, hence the pupil radius and the pupil shifts are expressed as lengths (SI unit metres). These need to be converted into pixels to calculate the pupil radius and shifts in pixels. This can be achieved with the help of the pixel size calculated above. The pupil radius is the aperture radius $R_{aperture}$ of the lens used in the experiment. Hence the pupil radius in pixels is:

$$R_{pix} = \frac{R_{aperture}}{\delta_l}. \quad (3.17)$$

The shift in the LED illumination angle is equivalent to shifting the lens as depicted by the dotted lens in Figure 3.5. These calculations are performed for a general case by taking all the experimental variables into consideration. The pupil shift in an FP setup depends on the LED position and the FoV position from the centre of the lens. These are zero for an on-axis LED and central FoV, however they vary for various parts of the FoV. The following equations are valid for any part of the FoV. The pupil shift in the lens plane is calculated by determining the hypothetical shift of the lens. The shift in the pupil centre due to the illumination angle is given as:

$$R_{aperture} = \left(\frac{P_{FoV} - L_{shift}}{L_{dist}} \right) u + P_{FoV} \cdot \quad (3.18)$$

The unit of the $S_{aperture}$ is expressed in length, hence it needs to be converted into pixels by dividing it with the pixel size in the lens plane as below:

$$S_{in_pixels} = \frac{S_{aperture}}{\delta_l} \cdot \quad (3.19)$$

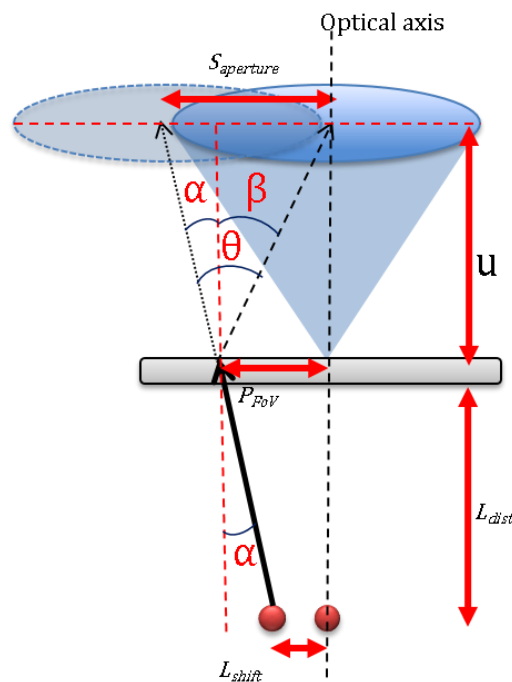


Figure 3.5 Pupil shift depiction. In Fresnel method, the frequencies shift due to the illumination angle is depicted as the apparent aperture shift, shown as the arrow headed dotted lines lens. In Fraunhofer method, frequencies shift is calculated using the angle between the excitation light beam and the light beam recorded by the lens (represented by the arrow headed dashed line). This is shown as θ in the figure. The dotted black line shows the optical axis of the system and the black bold arrow headed line shows the illumination angle of the LED.

Fraunhofer propagation method

Unlike the Fresnel method, in the Fourier method the pupil function is applied in the Fourier plane. Hence the pupil radius and the pupil shifts are expressed in frequencies (cycles/metre). These frequencies are converted into pixels by

dividing with the pixel size in the Fourier plane δ_F , which also has frequencies as units. The radius of the pupil aperture in pixels is given as:

$$R_{pix} = \frac{k \times NA_{obj}}{\delta_F}. \quad (3.20)$$

The pupil shift in the Fourier plane is calculated by measuring the effective numerical aperture of the illumination angle with respect to the centre of the lens, i.e., $\sin(\theta)$ depicted in Figure 3.5. This is the angle between the zeroth order of the diffracted light and the higher order entering the centre of the lens as observed in the figure. θ is the sum of two angles α and β as shown in the figure. These angles can be calculated from geometry as follows:

$$\alpha = \tan^{-1} \left\{ \frac{P_{FoV} - L_{shift}}{L_{dist}} \right\}, \quad (3.21)$$

$$\beta = \tan^{-1} \left\{ \frac{P_{FoV}}{u} \right\}. \quad (3.22)$$

The shift in the pupil centre due to the illumination angle is given as:

$$S_{in_pix} = \frac{k \sin(\alpha + \beta)}{\delta_F}. \quad (3.23)$$

These equations can be now used in the recovery procedure to determine the pupil shifts due to the illumination angles for both Fresnel and Fraunhofer methods.

Fresnel vs Fraunhofer methods comparison:

The Fresnel method can be condensed to the Fourier method with exception to the quadratic phase factor in the first step after the approximations made earlier in this chapter. Hence their further differences are studied by observing the pupil positions for two different experimental configurations implemented in this work. First setup has a 0.025NA objective lens and the second one has a 0.007 NA objective lens. The first setup is used in the experiments presented in the current and next chapter, whereas the second setup is used in chapter 5. The calculated pupil diameters for both methods are very similar: 39.84 and 39.83 pixels for

Fresnel and Fraunhofer methods respectively for the first setup and 36.27 and 36.18 pixels for the second setup. The pupil positions for the LEDs in the array for the central section of the FoV are calculated for both Fresnel and Fraunhofer methods and their difference is plotted as shown in Figure 3.6. It can be observed that for the low-NA system the difference is zero until 5th LED from the centre and goes to a maximum of 3 pixels error for the 10th LED. However, for the higher-NA system the difference is zero only until 3rd LED from the centre and goes to 14 pixels error for the 10th LED. This explains that the Fresnel and Fourier formulation are very similar in nature and their pupil shifts and radii can be used interchangeably when the NAs are small - around 0.14. At higher NAs the differences become large as could be understood from their fundamental differences. Despite high similarity in the reconstruction algorithms, from these graphs it can be concluded that they differ significantly at higher NA. This difference is however small in the low-NAs. The Fresnel formulation also corrects for another fundamental factor that is usually ignored by the Fourier diffraction model. This is explained later with the help of the experimental results from the next section.

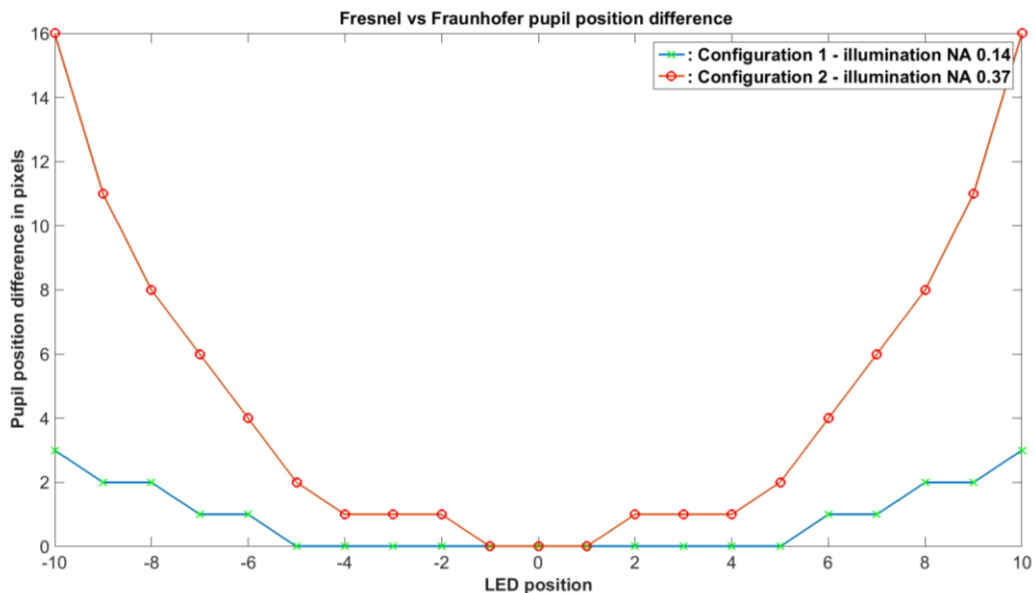


Figure 3.6 Fresnel vs Fraunhofer pupil position difference

3.2.4 Experimental validation

To validate the algorithm a conventional FPM dataset is acquired using the setup described in the next chapter. Here the FPM dataset is reconstructed using both the Fresnel based method and the Fraunhofer based propagation method and their results are displayed in Figure 3.7. A USAF resolution chart is chosen as the object. This chart highlights any artefacts in the reconstruction and provides quantitative image resolution. The central 256x256 pixels of the image are processed to produce a high-resolution image by using central 179 LEDs in a circle of a 15x15 LED array. The low-NA image had a resolution of 25 microns corresponding to the group 5 element 4 in the chart. FPM recovery provided a resolution of 5.24 microns corresponding to the group 7 element 4 in the chart.

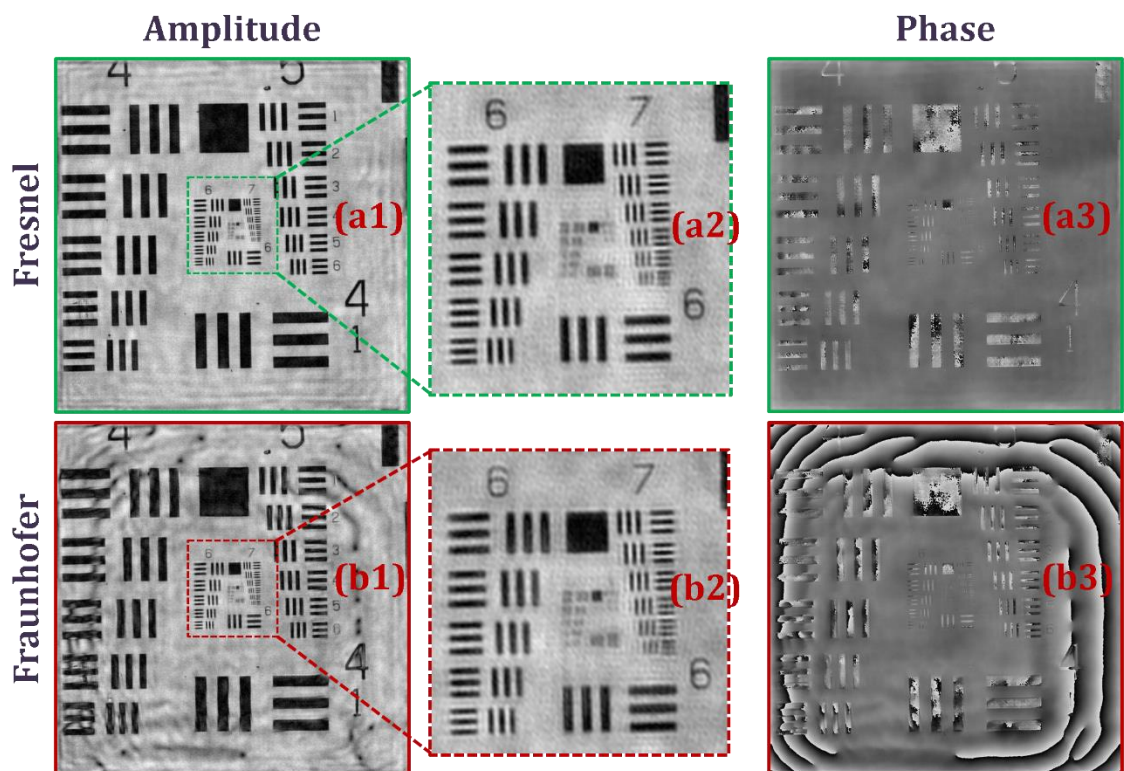


Figure 3.7 FPM data reconstruction using the Fresnel method and the Fraunhofer method

In the above figure the Fresnel model recovery results are displayed on the top and the Fraunhofer model recovery results are displayed at the bottom. The central part of the recovered image amplitude is magnified and shown in the

middle to highlight the high-frequency features. The recovered phase is presented on the right. It can be observed that the recovery in the central part of the image is of good quality in both models. The group 7 element 4 is visibly resolved in both the results and the background does not have any strong variations. For a conventional FPM setup both recovery models should provide equal quality recoveries, which is observed in the central part of the recovered images. However, the edges of the recovered amplitude of the section have poorer quality in the Fraunhofer model, which is also observed in the phase recovery. This is manifested by strong ripples in the background, which is expected to be uniform. The artefacts in the recovered phase also show ripples where the recovered phase appears to be wrapped. The artefacts in the phase recovery appear in the same parts of the image where amplitude recovery artefacts are observed. The phase recovery artefacts suggest a defocus or a field-curvature type of effect. However, it is discovered that the Fraunhofer based formulation incorporates a small FoV approximation [7]. This is because a Fraunhofer propagation in far-field is also equivalent to the Fourier transforming property of a lens. In the Fourier transforming property of a lens, a small FoV is assumed. Hence the Fraunhofer method works under this assumption. When a larger section is processed in the above results, this approximation is broken, hence resulting in artefacts on the edges and corners. Hence, this imposes an additional restriction on the size of the image segment that can be processed besides the partial coherent requirements discussed in the last chapter. This is discussed in detail in the next section.

3.2.5 Spatially varying frequency sampling

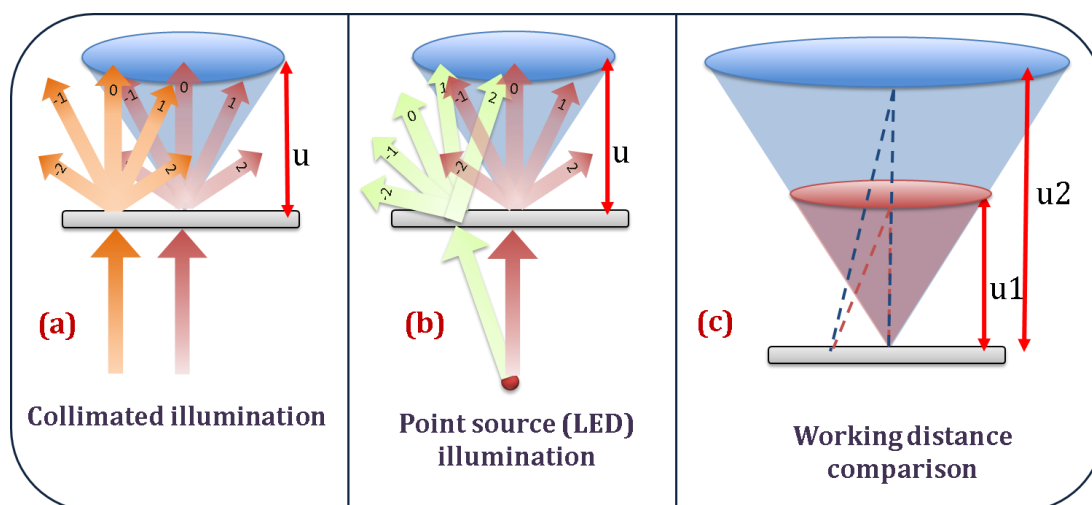


Figure 3.8 Spatial frequencies sampling across the FoV

In the object plane of a coherent diffractive imaging system the light is diffracted by each point in space. The diffraction orders directions emitted from a point in space depends on the illumination angle of the light. However, the diffraction orders captured by an imaging system (such as the objective lens) depends on both the illumination angle and the position of the object in space with respect to the centre of the objective lens. This is illustrated in images shown in Figure 3.8. In sub-image (a) a simple case of collimated illumination is considered. In this case the diffraction orders captured by the objective depends on the spatial position of the object with respect to the centre of the lens. Hence, this suggests that the spatial frequencies captured across the FoV differ. It can be approximated that the captured spatial frequencies are same in a small part of the FoV and they can be calculated separately for a different part of the FoV which is processed independently. This is an additional approximation inherent in the Fourier model but not discussed in the literature. In FPM literature the images are segmented into much smaller sections than the partial coherence limit and found to satisfy the additional criteria mentioned in this section without having knowledge of the spatial frequency variation criteria described here. The variation in the spatial frequencies sampled across the FoV is further aggravated by the point like emission from LEDs as shown in Figure 3.8 sub-image (b). It can also be observed

in sub-image (c) that the shorter working distance objectives have higher spatial frequency variation compared to a longer working distance objective lens despite having identical NA. For e.g., a 0.15 NA objective lens with 6mm working distance used in [48,121] has larger spatial frequency variation compared to a 0.15 NA commercial microscope objective lens [122].

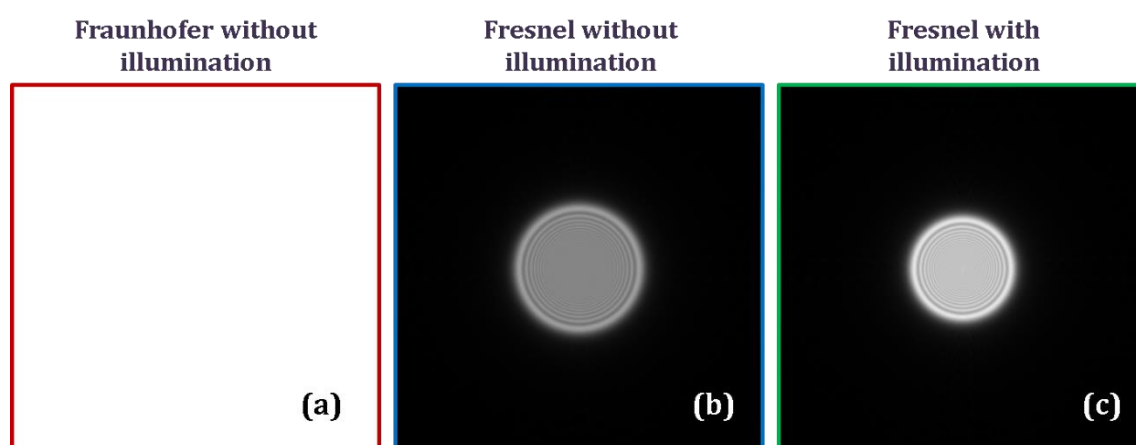


Figure 3.9 Bright-field diffraction ring simulation: A flat transparent object with no phase variation is chosen as the object. (a) shows Fraunhofer method simulation where a bright-field ring is not observed, instead the input object profile is seen. (b) shows Fresnel method simulation where a bright-field circle is observed but does not have right dimension since illumination wavefront curvature is not considered. (c) shows Fresnel method simulation where a bright-field circle is observed with right dimensions due to correct illumination wavefront curvature.

The Fresnel model encapsulates the spatially varying spatial frequency content, hence it provided better recovery across the entire reconstructed segment as observed in the reconstructed images. The Fourier transforming property of a lens is the key principle used in the Fraunhofer model, which assumes a small FoV [7]. Since Fresnel propagations method does not have such assumption, the Fresnel method works better. A simulation is performed to demonstrate the spatially varying frequencies sampled in an image. The experimental setup used in the results presented above is simulated using the Fourier model and the Fresnel model, with and without point source illumination. A completely flat transparent 8mm wide object with constant amplitude and phase is chosen as the sample and the results are displayed in Figure 3.9.

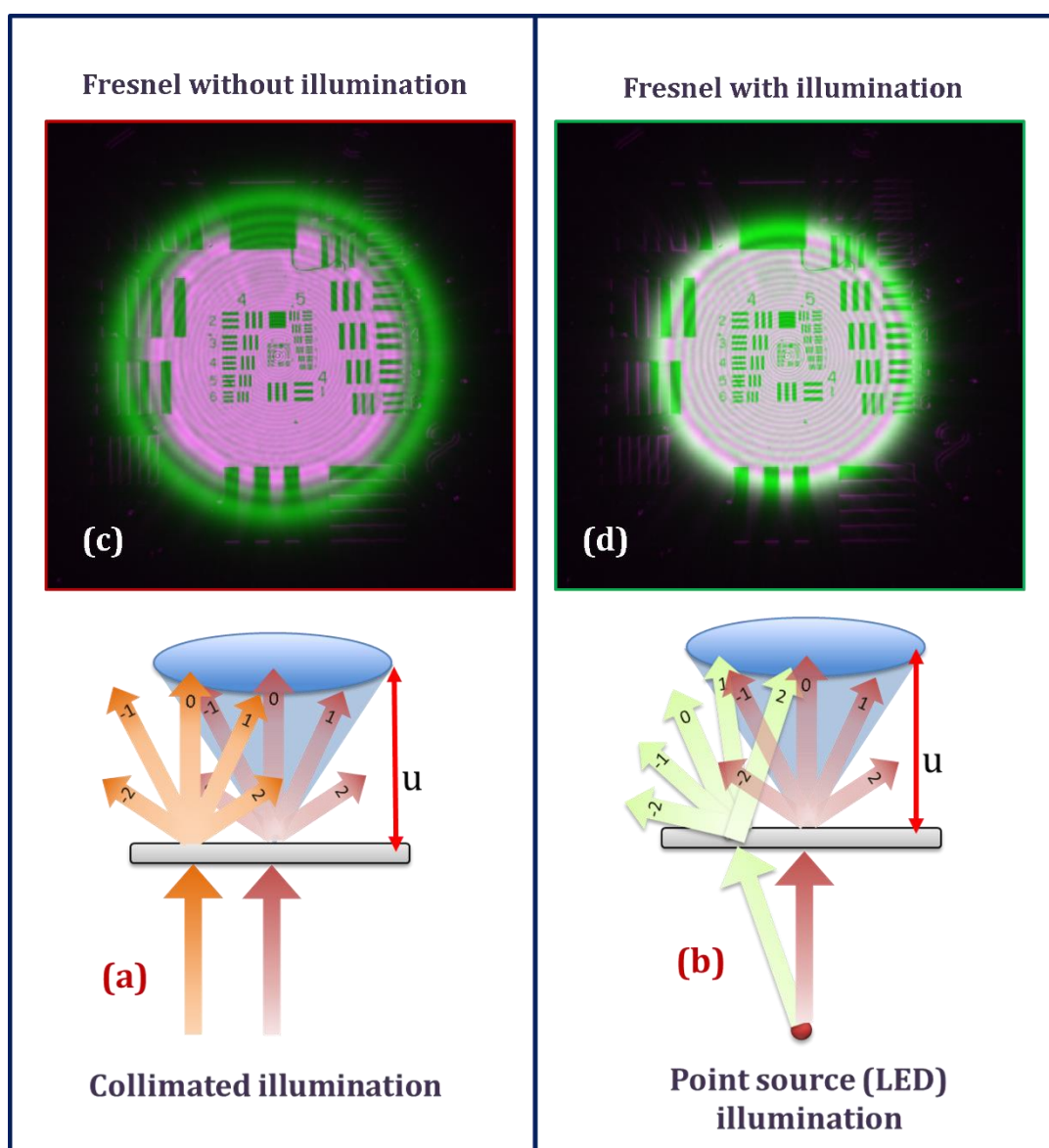


Figure 3.10 Bright-field diffraction ring experimental validation. Experimental image with a diffraction ring (in purple) is superimposed on the simulated image with a diffraction in green. Two scenarios are demonstrated, one where the illumination is collimated (a) and is a spherical wave from a point LED source (b).

In an experimental setup, a bright-field ring is observed due to the varying spatial frequencies being sampled (Figure 3.9 (b) and (c)). As we move away from the centre of the FoV, the angle of light coming from this position with respect to the centre of the FoV increases. Hence, higher spatial frequencies will be sampled at farther FoV. At a point in the FoV, these higher spatial frequencies sampled move from being bright-field frequencies to dark-field frequencies. Due to the circular symmetry of the lens, this is appeared as a ring, hence termed as a bright-field

ring. This bright-field ring can be observed in the Fresnel based simulation models shown in Figure 3.9 (b) and (c) but cannot be seen in Fraunhofer based model shown in sub-image (a). The diameter of this ring depends on the numerical aperture of the objective and the working distance (or focal length in a 4f system). In the setups where LEDs are used for illumination, the bright-field ring diameter also depends on the distance of the LED array. The expanding nature of the point source illumination wavefront further reduces the diameter of the ring as seen in sub-image(c). This demonstrates that the Fresnel model incorporates the spatially varying spatial frequencies phenomenon, hence relaxes the FoV segment size processed in FPM recovery. It can also be observed that the wavefront curvature from the point source illumination is also corrected within the reconstruction. In Fresnel model the FoV segment processed is limited by the source partial coherence and off-axis aberrations of the imaging system.

In Figure 3.10, the simulated bright-field ring (green) is compared with the experimentally captured bright-field ring (magenta). Image (c) is obtained by superposing simulated bright-field ring without illumination wavefront curvature correction on the experimentally captured bright-field ring. Since the illumination wavefront curvature correction is not implemented, the bright-field ring diameters do not match. The simulated bright-field ring in green is larger than the experimentally obtained bright-field ring in magenta. However, when the illumination wavefront curvature is considered in the simulation, the bright-field ring diameters match in sub-image (d). The diameter of simulated green bright-field ring is approximately same as the experimentally obtained bright-field ring in magenta. The simulated and experimental bright-field rings comparison can be used to calibrate an experimental setup. The diameter of the experimental bright-field ring is compared with the simulated data to estimate the LED array distance or the aperture diameter. The shift in this bright-field circle due to changing illumination angle is used to find the appropriate orientation of the image (flips and rotations of the image by the detector) and pupil shifts. This is implemented in all the experimental reconstructions of this thesis to provide robust initial estimates which improved the calibration procedure.

3.3 Summary

This chapter presented the core concepts of this thesis, MA-FPM principle and the Fresnel recovery algorithm. The MA-FPM principle was presented with the help of the diffraction orders produced by a Ronchi grating. It was proposed that the conventional Fraunhofer approximated model is insufficient to model the off-axis imaging systems in MA-FPM systems, a Fresnel propagation based model is consequently suggested. The design parameters of a typical MA-FPM system were discussed. The MA-FPM setup presented here assumes that the lenses and detector are placed in planar arrays to satisfy the experiment performed in the next chapter. A more generalized setup is proposed in later chapters.

The Fresnel model reconstruction algorithm was presented. The field propagation using Fresnel diffraction integral was then discussed in detail. It was demonstrated that the sampling criteria in Fresnel propagations is satisfied in all the propagations. The pixel size calculations in Fresnel propagations were presented. The pupil shift calculations are presented for both Fourier and Fresnel methods. The differences in the Fourier and Fresnel reconstruction method were studied to get a better understanding of their limitations.

FPM data captured for the next chapter was processed using both Fourier and Fresnel methods. It was observed that the Fourier algorithms provide sufficient quality reconstruction in the central section of the image but fails in the edges of the image. This is explained by the small FoV approximations made for the spatially varying spatial frequencies in the Fraunhofer approximated model which was not discussed in the literature. This limitation was discussed in detail in the context of FPM and it was demonstrated that the Fresnel model doesn't have this limitation and hence is preferred for FPM recovery. It is also suggested that a Fresnel model can be used for robust calibration of several parameters in experiments.

Chapter 4 Multi-Aperture FPM experimental validation

This chapter describes the experimental setup used for validating the MA-FPM concept described in the previous chapter. The calibration procedure implemented in the experiment is discussed along with the results obtained for the calibration step. The reconstruction procedure implemented is explained and the results obtained from this setup are presented. The quality of the results and limitations of the current system are debated in the summary.

4.1 Experimental setup

Figure 4.1 shows a picture of the experimental configuration implemented. MA-FPM configuration is emulated by translating a lens and a detector to the positions of the lenses and detectors in the system design. The objective lens is mounted on a motorized translation stage such that the system parameters remain same between the datasets and required positions of the lens are achieved with high precision. The detector is translated manually and any errors in the image positions are corrected using image registration as described in the later sections.

In the experiment, an MA-FPM system with 3x3 lenses is implemented with a 5x5 LED array. This is equivalent to an FPM system of 15x15 LEDs, therefore providing nine times higher data throughput. An NA of 0.025 is achieved for an individual imaging system in the array using *Edmund optics* achromatic lenses with 36mm focal length and 9mm diameter, cropped to 3mm diameter clear aperture. This was achieved by using a 1.7X magnification, providing the distance from the object plane to the lens plane u as 57mm and the image distance from the lens

plane v as 97.2mm. An *Andor Zyla 5.5* camera is used as the detector. It has a pixel size of $6.5\mu\text{m}$, providing a sampling factor of 3.8 times the Nyquist limit.

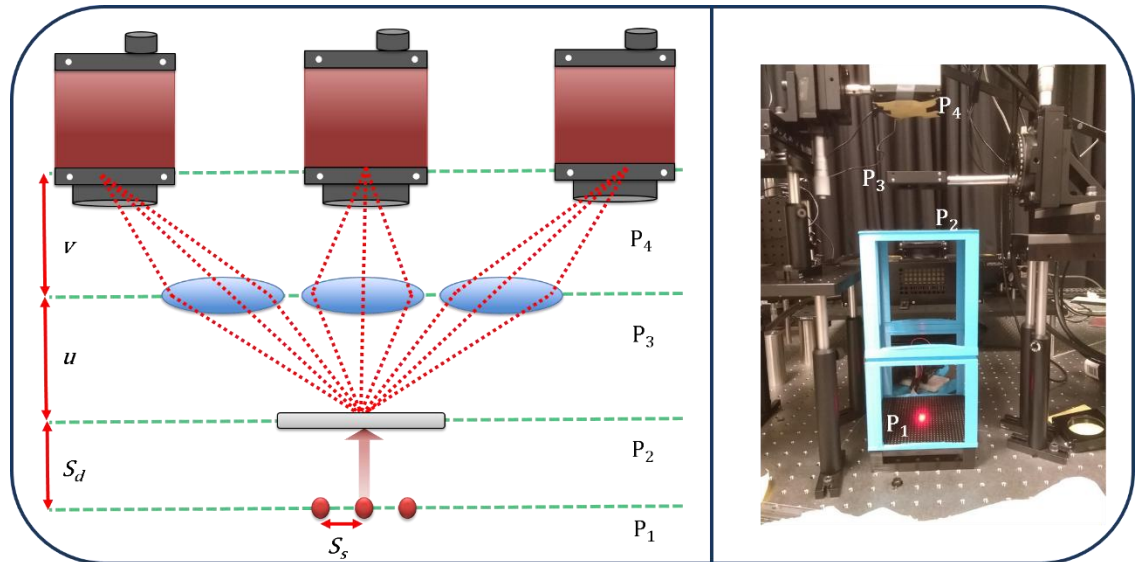


Figure 4.1 MA-FPM experimental setup configuration. P_1 : LED array plane. P_2 : Object plane. P_3 : Lens array plane. P_4 : Detector array plane. S_s : Separation between the LEDs. S_d : Distance from the LED array plane to the object plane. u : Distance from the object plane to the lens array plane. v : Distance from the lens array plane to the detector array plane.

An *Adafruit* 32x32 P4 LED array with 4 mm LED separation is used for illumination. It is placed at a distance of 257mm below the object such that a minimum of 61% overlap is achieved in the spatial frequencies recorded from any two adjacent LEDs. A synthetic NA of 0.119 is achieved with the MA-FPM configuration, i.e., using 3x3 lenses and 5x5 LEDs: a factor of four increase in the NA over the individual objective lenses NA. Within this setup, matching synthetic NA can be achieved by using 15x15 LEDs in the array with the on-axis imaging system (FPM configuration).

The separation between the lenses in the array is chosen to be 4.25mm such that the synthetic NA of MA-FPM system and FPM system are matched. This allows us to compare the images obtained from both the systems directly so that the MA-FPM system can be validated. Due to the chosen lens separation, when the fifth LED from the centre of the array illuminates the object a bright-field image can be seen on the corresponding off-axis lens system. This bright-field image can be

used for aligning the system. An array of 15x15 LEDs around this fifth LED can be used to generate an FPM system similar to the on-axis FPM system. This is used in the calibration procedure as described later.

In the MA-FPM experimental datasets, the central camera is operated at 100 milliseconds exposure time and other cameras are operated at 1000 milliseconds to improve the SNR in the off-axis cameras. The off-axis cameras only record dark-field images, hence suffer from low light intensities and reduced SNRs. Images from different cameras are later normalized accordingly before processing. Similar procedure is followed for FPM datasets, images with central 5x5 LEDs in the array are acquired with 100 milliseconds exposure and rest are acquired with 1000 milliseconds exposure. The illumination intensity variation due to the LED positions and their angles is also calculated based on the LED's datasheet and corrected along with the exposure variation correction.

In this experiment, only the red LEDs in the array are used. These LEDs have a FWHM of 17 nm centred at 623 nm. During the reconstruction, 2048x2048 pixels in the image on the detector are divided into sub-image segments of 256x256 pixels and processed individually to satisfy the partial coherence requirements [34, 23]. The SBP of the initial low-NA system is 0.48 megapixels (which is also the SBTP) and the SBP of the final MA-FPM system is 18.6 megapixels. It should be noted that the low-NA images were oversampled by 3.8 times the Nyquist limit due to the system design. The maximum travel of the translation stages is limited, hence the synthetic objective NA of the reported MA-FPM system. The system design to fit these limitations resulted in oversampling due to the finite conjugate configuration of the lenses, reducing the SBP achieved. This can be addressed by using a different focal length objective lens. A SBP up to 160 megapixels can be achieved using such system (sampled at Nyquist frequency) using a 4 megapixels image sensor. Even higher SBP can be achieved by using either more lenses and/or more LEDs. The SBTP of the reported MA-FPM configuration is 0.7440 megapixels per snapshot, whereas the SBTP of an equivalent FPM configuration is 0.0827 megapixels per snapshot, much lower than the initial low-NA system SBTP (0.48 megapixels per snapshot). The SBTP of the reported MA-FPM configuration can be

further increased using LED multiplexing illumination to produce a very large SBTP setup.

4.2 Calibration procedure

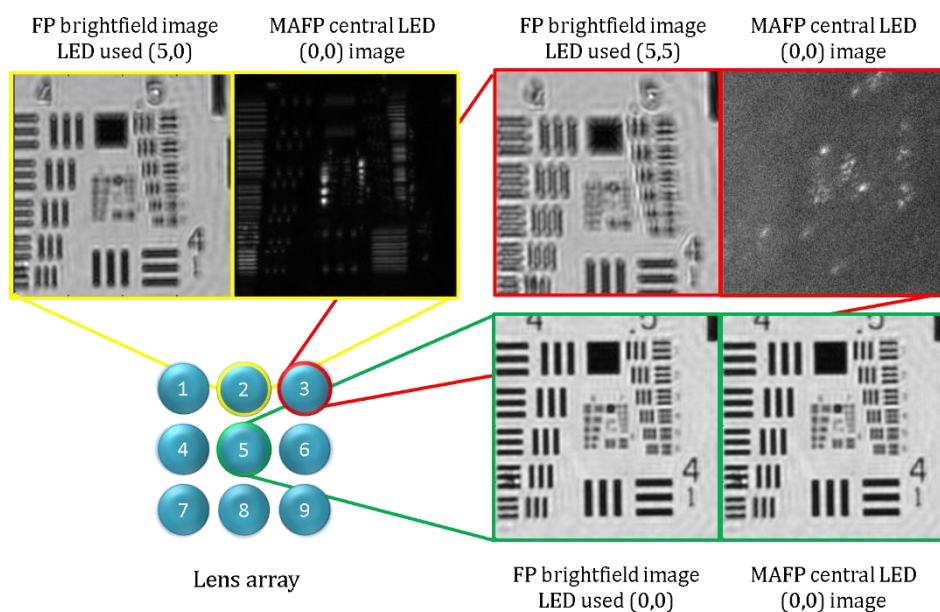


Figure 4.2 Aberrations and registration errors between the MAFP images from different cameras

In the MA-FPM system, each lens samples a distinct set of spatial frequencies for a given illumination angle as discussed previously. This can be observed in Figure 4.2. Three imaging systems in the array are chosen and images obtained from these are displayed in the figure. For each lens, two images are displayed. The images on the right are captured when the central LED in the LED array is used for illumination, i.e., the illumination angle was zero. The on-axis imaging system records the bright-field image, whereas the off-axis imaging systems record dark-field images. These are typical images obtained in an MA-FPM setup; they have distinct set of frequencies. Hence, these images cannot be registered using conventional image registration procedures [123-125] since these methods require common features in the images from different cameras for registration. Therefore, the illumination angle (LED position) is chosen such that the bright-

field frequencies shift into the passband of the off-axis imaging system. Thus, using a distinct illumination angle bright-field images can be captured as shown in the left images of each imaging system in Figure 4.2.

The translation between the images due to alignment errors can be clearly seen in these images. It should also be noted that each of these imaging systems have dissimilar aberrations. This makes it not possible to register these bright-field images with good accuracy. As discussed in the previous chapter, for robust FPM reconstruction, it is essential to have LED positions and aberrations estimated with high precision. Hence, these off-axis aberrations must be estimated for the reconstruction process. It should also be noted that in the MA-FPM reconstruction procedure, each imaging system only has a small number of images (25 in this experiment). This does not provide the required redundancy to recover the minor errors in the aberrations within reconstruction procedure [87]. Therefore, the aberrations in the MA-FPM system need to be pre-calibrated with highest accuracy possible.

A calibration dataset is captured in this experiment to tackle these issues. An FPM dataset is recorded for each imaging system in the MA-FPM array such that all these datasets sample approximately same set of spatial frequencies. A circular array of LEDs with a diameter of 19 LEDs is chosen around the bright-field LED for each of the imaging systems. For e.g., 293 LEDs in a circle around (5, 5) LED from the centre of the optical axis is chosen for imaging system 3 shown in Figure 4.2. The FPM reconstruction [78,87,100] is performed on these individual FPM datasets using Fresnel propagations described in the previous chapter. This results in two key advantages: 1) Aberrations in the imaging systems can be recovered with the precision required for FPM recovery due to the large number of LEDs present in these datasets. 2) The final image recovered by all the imaging systems will have aberration free matching images of the object with similar set of frequencies that can be used for image registration. Implementing this information in the MA-FPM recovery will produce robust reconstruction.

4.2.1 Aberrations estimation

Aberrations in FPM can be usually corrected within the reconstruction procedure as discussed in the previous chapters. Embedded pupil recovery was proposed to recover unknown aberrations within the reconstruction procedure. However, in the presence of severe aberrations, the pupil recovery might fail. Hence, it is important to have an approximate knowledge of the aberrations in the imaging system to use it as an initial estimate of the pupil aberrations. In the off-axis imaging systems the aberrations can be severe, hence cannot be recovered within the reconstruction. These aberrations are caused from the off-axis imaging configuration; therefore, they can be estimated using simulated optical models.

Zemax software was used to simulate the MA-FPM system design and estimate the pupil aberrations. An achromatic doublet lens is used as the objective lens in the experiment. The lens data was acquired from the manufacturer's website and simulated using sequential mode in *Zemax* [126]. The key parameters are: radius of the first surface (22.16mm), radius of the second surface (-15.98mm), radius of the third surface (-46.14mm), centre thickness of the first lens (2.5mm), centre thickness of the second lens (1.5mm), the first lens material (N-BK7) and the second lens material (N-SF5). The object distance and image distance are chosen for 1.7X magnification and the aperture diameter was set to 3mm. Zernike standard coefficients are generated in the software, which are then used to simulate the pupil phase in *Matlab*. The off-axis imaging system is simulated by decentering the objective lens. The layout of the optical system created in *Zemax* is shown in Figure 4.3 (a) and (b); the point spreads functions generated are shown in (c) and (d). It can be observed that the off-axis PSF is aberrated compared to the on-axis PSF.

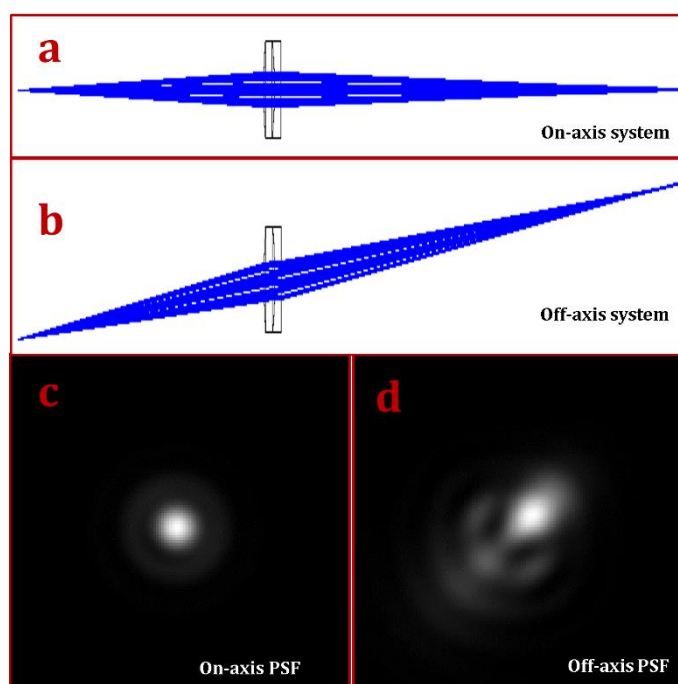


Figure 4.3 Modelling aberrations in Zemax

These Zernike coefficient estimates are used to generate the pupil phase estimates in *Matlab* for FPM reconstruction. These pupil phase estimates are used as initial guess values for the pupil phase in the reconstruction and the pupil recovery is implemented to improve this estimate. A final pupil phase estimate is generated from processing of the calibration data. The Zemax estimate and FPM update of this estimate are shown for two imaging systems in Figure 4.4. The Zernike modes estimated from *Zemax* are plotted for these two imaging systems. For imaging system number six (yellow bars in the bar plot), the aberrations present are defocus, vertical astigmatism, vertical coma and spherical aberration. This can be justified from the horizontal position of the lens. For the imaging system number one (blue bars in the bar plot), the aberrations present are defocus, oblique astigmatism, vertical coma, horizontal coma and spherical aberration. Presence of both vertical and horizontal coma can be explained by the diagonal position of the imaging system. The final update estimates from FPM recovery on calibration data are used in the MA-FPM recovery procedure, resulting high-quality reconstruction as observed in the results section.

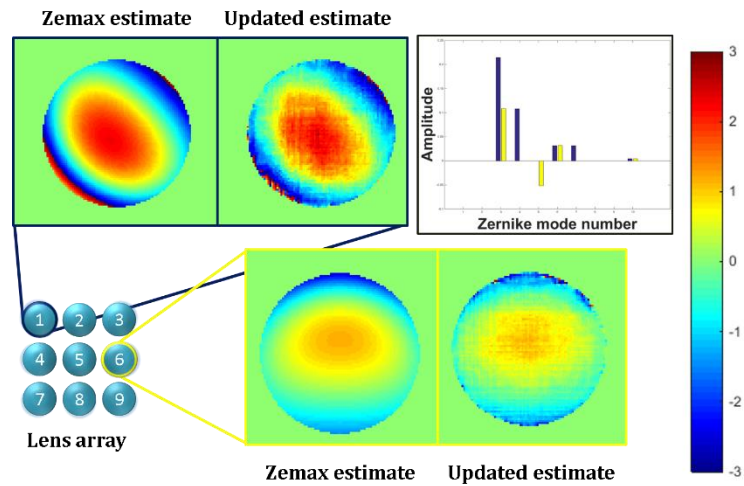


Figure 4.4 Pupil aberrations. Units on the colour bar are radians.

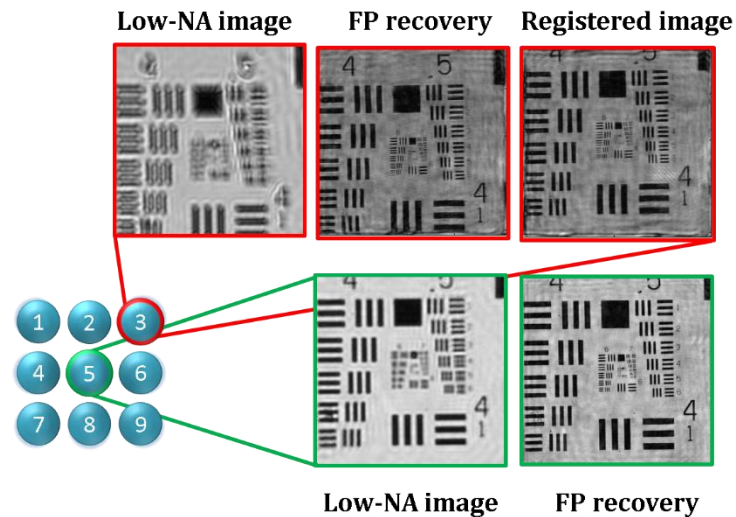


Figure 4.5 Image registration.

4.2.2 Image registration

It is important to register the images from different detectors in the MA-FPM system to avoid frequency stitching errors in the reconstruction. As seen in Figure 4.5 low-NA images, the images are translated with respect to each other. A high-resolution FPM recovery is performed on these individual imaging systems and they are registered with respect to the on-axis system. The recovered high-NA images and the registered off-axis image can be seen in Figure 4.5.

In this experiment, translation stages are used to move the objective and the detectors. Hence, the images only suffer from translation error. Therefore, only the translation vector between the mis-registered high-resolution images is calculated. This is performed manually in this step for simplicity but can be automated using image registration methods. When multiple image sensors are used, they might suffer from additional factors such as tip, tilt and rotation of the sensor. This is considered in the later chapters when multiple detectors are implemented. It should be noted that the translation was performed to only one pixel error to avoid interpolating the data. This accuracy was observed to be sufficient for FPM reconstruction. The translation vector obtained here is applied on all the low-NA images obtained in MA-FPM datasets. This registers the images from different cameras with the required accuracy.

4.2.3 Calibration results

FPM calibration data for individual imaging systems was captured and processed as described so far. In Figure 4.6, the FPM reconstruction for these datasets is presented. The colour bar for pupil phase in this image is same as for Figure 4.4. It can be observed that the estimated aberration values from Zemax modelling match very well. The FPM recovery for horizontal and vertical off-axis imaging systems (2, 4, 6, 8) is of high quality as observed in the sharp recovery of group 7 elements; however, the FPM recovery for diagonal off-axis imaging systems (1, 3, 7, 9) is slightly of lower quality as observed by the low-contrast in the group 7 elements. This can be possibly due to the spatial frequency content in the diagonal lenses is slightly less due to the arrangement of the LEDs in the array. The aberrations are also higher in diagonal imaging systems, hence can produce lower-quality reconstruction despite the aberration correction. In these results, it can be clearly seen that the high-resolution reconstructed images can be easily registered due to highly similar features unlike the low-resolution images seen on the right. At the end of this procedure, the translation vector for image registration of MA-FPM images is obtained and aberrations in these off-axis imaging systems are recovered. This calibration data provides high-quality MA-FPM reconstruction as seen later.

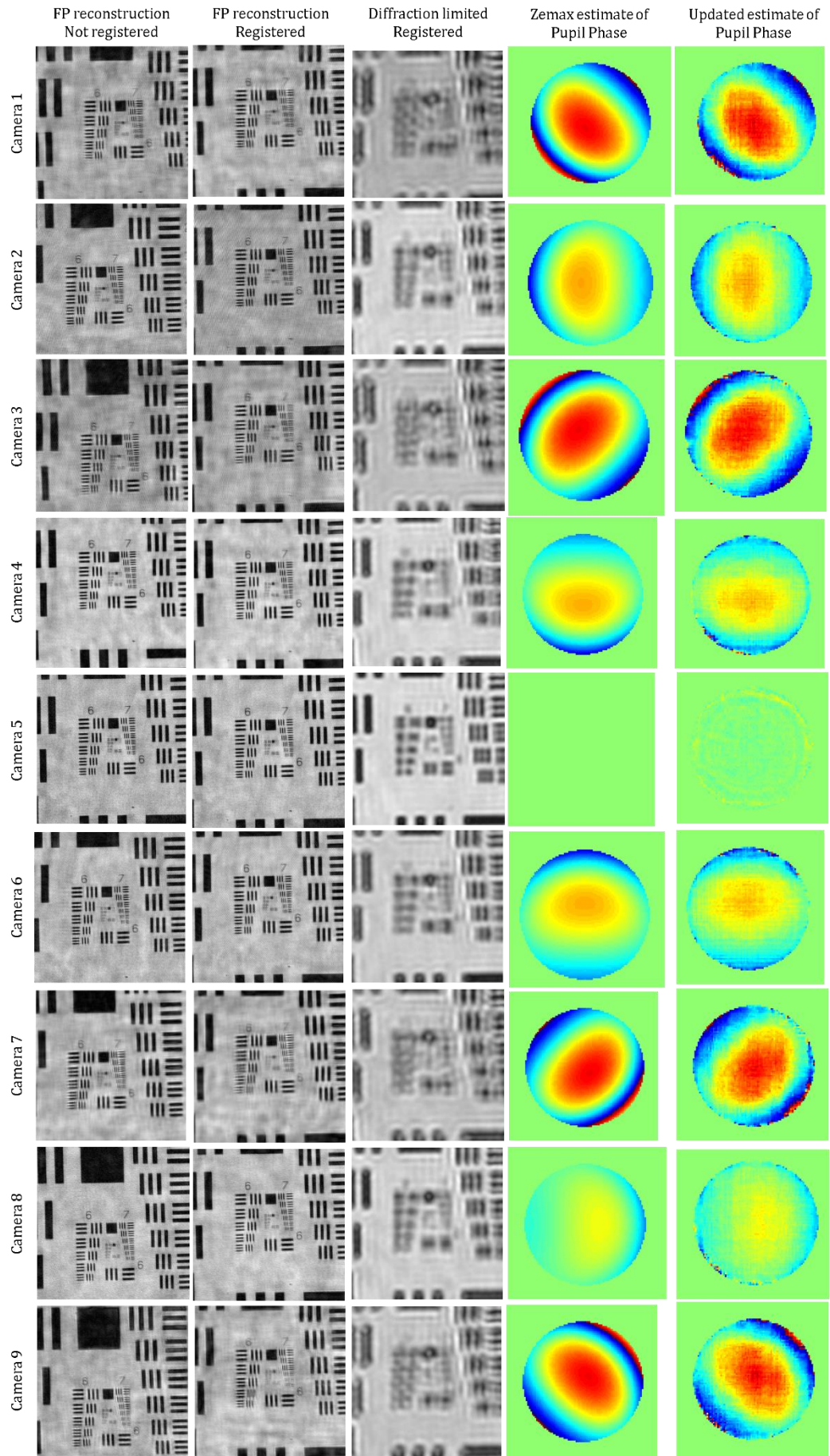


Figure 4.6 MA-FPM Calibration results

4.3 Reconstruction algorithm

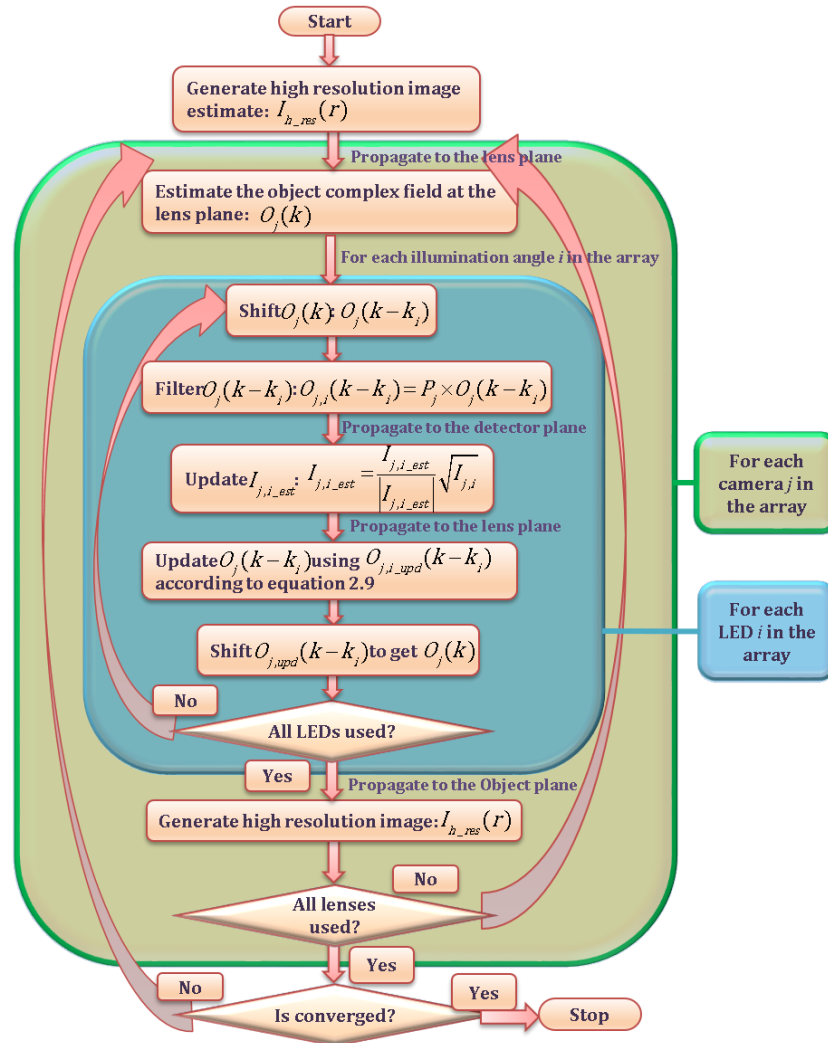


Figure 4.7 MA-FPM reconstruction algorithm.

The reconstruction algorithm for MA-FPM is similar to the Fresnel reconstruction algorithm described in the previous chapter. In the previous algorithms within one iteration, all LED angles are processed. In the MA-FPM reconstruction all lenses are processed within one iteration and for each lens, all the LEDs are also processed. Hence, this algorithm has two loops within a single iteration as observed in the flowchart in Figure 4.7. The rest of the process remains identical to the Fresnel reconstruction algorithm.

4.4 Experimental results

A 1951 USAF resolution test chart is widely used to demonstrate the resolution achievement of an imaging system quantitatively [115,127]. This is also followed in FPM to demonstrate the quantitative improvement in the achieved resolution. This imaging chart also highlights any artefacts in the imaging system; such as low contrast in the high frequencies found in an incoherent imaging system [107], tilting of the bars for LED position error artefacts [89] etc. Hence, we used it to validate the resolution improvement claims of our MA-FPM system. An FPM dataset with equivalent NA is also recorded and processed to compare our setup results. This comparison validates the MA-FPM theory.

Figure 4.8 (A) shows the reconstruction of the resolution test chart under different conditions. An objective-NA-limited low-resolution image is displayed in (a1). The objective NA was 0.025, which corresponds to Rayleigh resolution limit of 25 microns. This is represented by group 5 element 4 in the resolution chart, which is the smallest group resolved clearly. The synthetic NA in this setup is 0.118, corresponding to a resolution limit of 5.27 microns and equivalent to group 7 element 4 on the resolution chart. This element is expected to be resolved clearly in the FPM and MA-FPM reconstructions, which can be clearly seen in sub-images (a2) and (a3). This validates the resolution claim of the FPM and MA-FPM systems. The image reconstruction quality in FPM and MA-FPM recoveries is very similar; the groups resolved and their sharpness are similar, hence this proves that MA-FPM can produce results of similar quality to FPM with nine times faster data throughput.

In sub-image (a4) the MA-FPM recovery is performed using pupil phase estimated from the Zemax modelling. It can be seen that the image quality is comparable to the MA-FPM recovery using a pupil phase estimated from the calibration data but the high-frequency elements (group 7 element 4) have a few artefacts and their contrast is lower. This demonstrates that calibration dataset is required to achieve high-quality results. In sub-image (a5), the MA-FPM recovery is performed without any pupil phase estimation. In spite of resolving the group 7

element 4, the reconstruction quality is very poor and the contrast of the resolved bars is lower. This demonstrates the importance of the pupil phase correction.

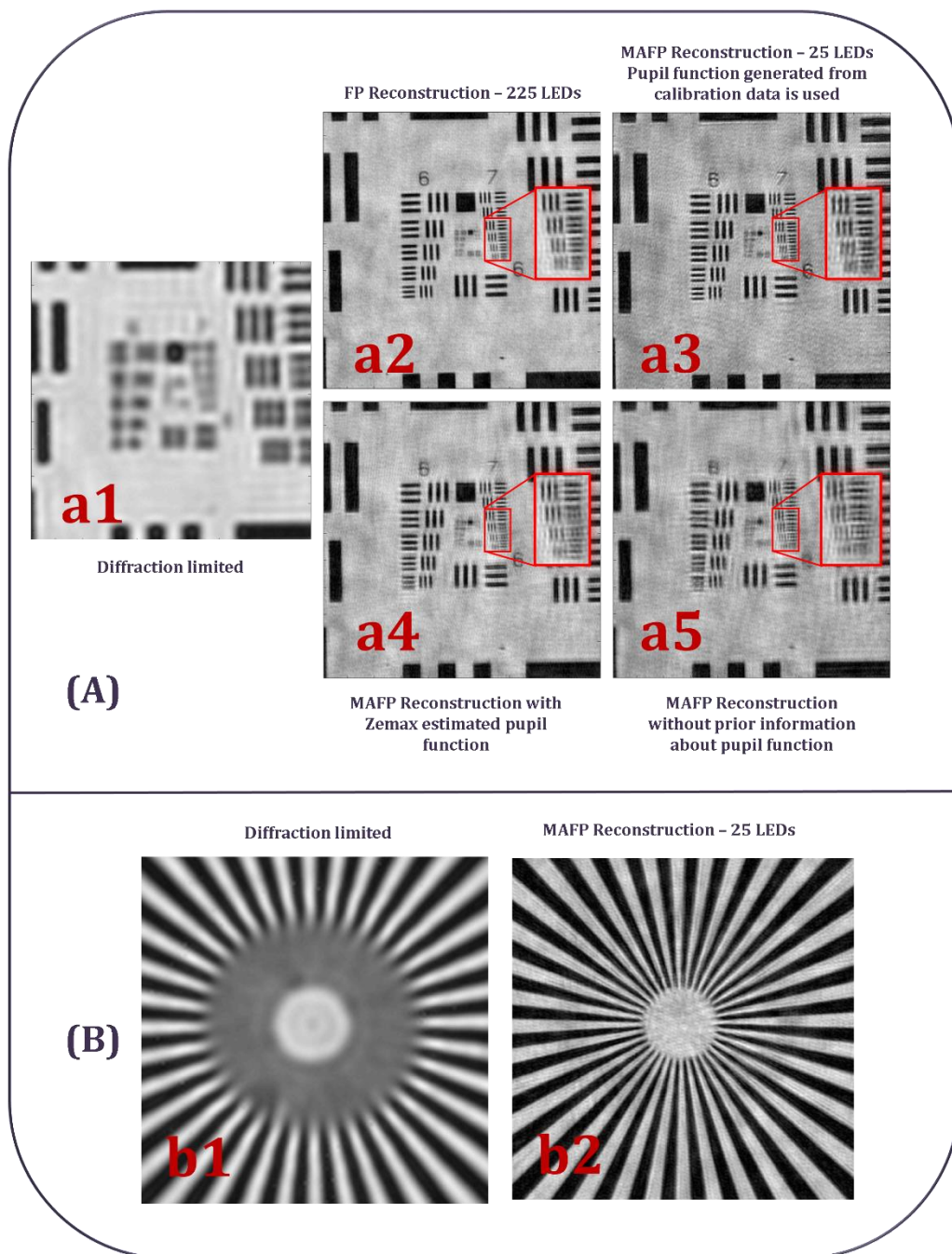


Figure 4.8 MAFP experimental results of calibration targets. 1951 USAF resolution calibration-target image is shown in (A) and a spokes calibration-target image is shown in (B).

In Figure 4.8 (B), image of a spoke target is shown. The spoke target is also an extremely useful imaging-system characterization tool. Unlike the USAF resolution

chart, the spokes target has continuous spatial-frequencies in all directions. Hence, a spokes target is imaged to demonstrate that spatial frequencies in all directions are recovered with high quality. Sub-image (b1) shows an objective-NA limited image and sub-image (b2) shows MA-FPM recovered image. This demonstrates high quality omnidirectional spatial-frequencies recovery of the MA-FPM system.

A microscopic slide is also imaged to demonstrate the high-quality recovery throughout the FoV. A “*woody dicotyled-stem cross section taken at 3 years*” microscopic slide from Brunel is chosen as the sample. This sample has three rings of cells, corresponding to the 3-year growth of the plant, with varying sizes of cells within each ring. This was helpful in identifying the resolution improvement very clearly and focusing the sample at low-resolution. The sample was approximately eight millimetres wide. The MA-FPM FoV could image the entire sample.

The full FoV MA-FPM reconstruction of the sample is shown in Figure 4.9. It can be seen that the low-resolution image has only central part in a circle of the sample imaged in bright-field, whereas rest of the sample is imaged in dark-field. This demonstrates the bright-field ring theory discussed in the last chapter. This bright-field ring can be avoided if all the LEDs in the array are illuminated, resulting in an incoherent illumination. It should be noted that due to the incoherent illumination, the phase information will be lost.

Three localized areas across the FoV are magnified to show the smallest features (cells of various sizes) that are recovered. These three image segments are taken from the central section of the FoV (shown in yellow box), 30% of the FoV away from the centre (shown in red box) and 75% of the FoV from the centre (shown in green box) to demonstrate the high-quality reconstruction across a wide FoV. The reconstruction quality in the edges (over 75% FoV) is degraded slightly due to the higher levels of aberrations present in the edges of the FoV. Field-curvature and distortion can be additional factors for the degraded image quality, which were not considered in this thesis. These can be addressed by using advanced reconstruction algorithms [91]. Since MA-FPM is a coherent imaging

technique, phase is also recovered in the reconstruction. The recovered phase is shown next to the recovered amplitude in the above figure. Phase information can be extremely useful, especially when imaging unstained samples. Therefore, MA-FPM can be used in such situations.

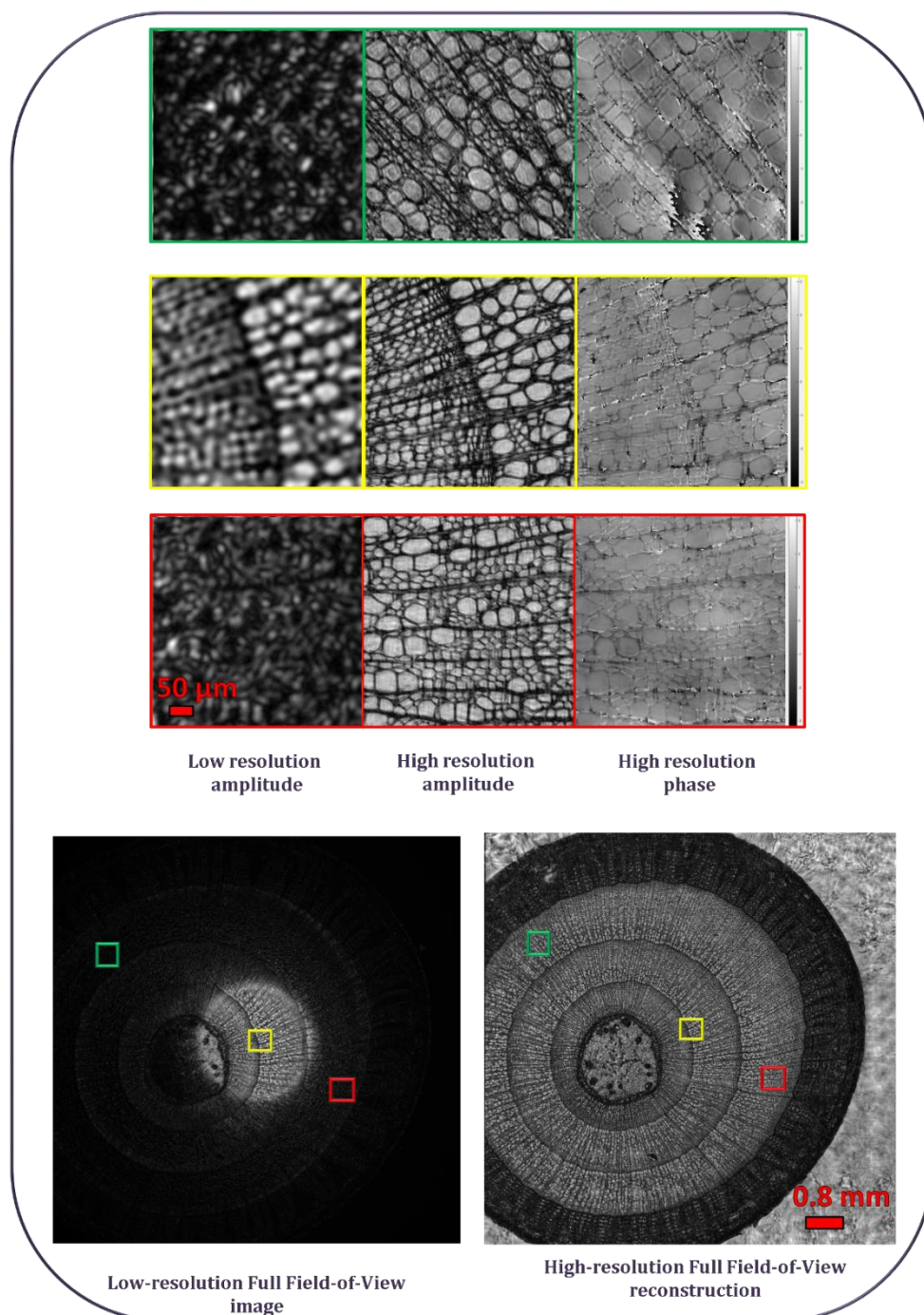


Figure 4.9 MA-FPM experimental results. Full FoV reconstruction of a *woody dicotyled-stem cross section* taken at 3 years. Three segments of the full FoV are shown at the top.

The experimental results in this section verify the MA-FPM theory proposed in the previous chapter. From this experiment it is observed that the off-axis imaging system suffer from severe aberrations which can degrade the image reconstruction. This can also limit the maximum achievable synthetic objective-NA in the experiment due to the increased point spread function size. However, these aberrations can be corrected within the experimental setup described in the next chapter. This will increase the maximum achievable NA, improving the scope of MA-FPM.

4.5 Summary

This chapter described the experimental setup implemented to validate the MA-FPM theory. In this experiment, an MA-FPM system is created by translating an objective and a detector for a proof of concept demonstration. This setup benefited from reduced number of degrees of freedom in a multi-camera system such as varying noise statistics between detectors, additional tip, and tilt positioning errors etc. A system with multiple detectors is developed in the next chapter. The calibration procedure implemented to achieve robust reconstruction was reported in this chapter. It is shown that obtaining FPM datasets for individual systems will provide the necessary calibration on pupil aberrations and image registration. In this particular experimental configuration, the objective lens is translated to focus the image. This can produce minor imaging system variations due to the finite conjugate nature of the lenses configuration in the MA-FPM setup. However, it was observed that the FPM reconstruction algorithm is robust despite such variations. An ideal setup would translate the sample to focus, as demonstrated in the future experiments.

Experimental results validated the MA-FPM theory: USAF resolution chart and the spokes target were imaged with good quality. A microscope slide is also imaged and its full FoV reconstruction of amplitude and phase was presented. The reconstruction is of high quality in most of the FoV except the edges due to the high amount of aberrations, which can be addressed by the experimental configuration proposed in the next chapter.

Chapter 5 Scheimpflug MA-FPM

In the previous chapter it was observed that the aberrations in the off-axis imaging systems degrade the recovered image quality. To address this issue, an experimental configuration based on Scheimpflug condition is proposed in this chapter. This setup can minimise the off-axis aberrations experimentally, resulting in high-quality images. A Scheimpflug MA-FPM setup is presented using 3D printed parts. The FPM recovery forward model for Scheimpflug condition is presented and is validated experimentally.

5.1 Curved lens array

In the previous chapters a planar lens-array is implemented in MA-FPM systems due to its simplicity. However, when working with higher-NA systems, a curved array is preferred. The NA of the off-axis systems in the planar array will get progressively smaller with their distance from the centre to the on-axis system NA, which is not the case in a curved array. This implies that a curved lens array will have higher synthetic NA compared to a planar lens array with identical lenses and array size. A curved LED array is preferred for FPM illumination due to a similar reason [92,128].

When the lens-array is curved, the object plane will be tilted with respect to the off-axis lens plane. If the detector plane is placed parallel to the lens plane, then the image will suffer from spatially varying aberrations. To obtain best image quality, Scheimpflug condition [129,130] must be deployed. Scheimpflug condition and its implementation is discussed in later sections of this chapter. In the curved lens-array, the light path of an off-axis system is same as the on-axis system unlike the planar arrays, as seen in Figure 5.1. Hence, this can relax the Fresnel

propagation requirement discussed in Chapter 3. The forward model of the Scheimpflug FPM systems is discussed in later sections.

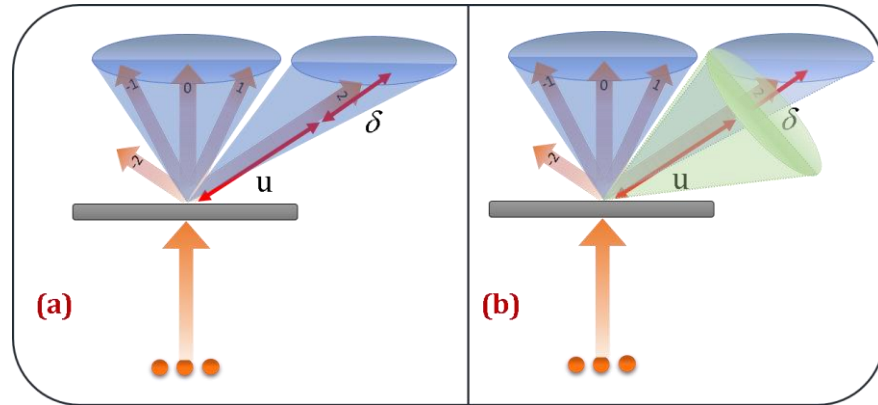


Figure 5.1 Planar lens array (a) vs Curved lens array (b)

5.2 Scheimpflug principle

The Scheimpflug principle is a geometrical condition developed by Theodor Scheimpflug in 1904 to correct for perspective distortions in aerial photographs [131]. It was widely used in photography to image tall structures such as building as seen in Figure 5.2 (a) and is still used in some digital projectors (for keystone correction) when projecting images onto tilted screens. Currently, it is widely used in stereo microscopy for particle tracking applications [132-134] and corneal pachymetry imaging systems [135-138]. In this chapter, we propose a new application: implementation in MA-FPM systems with curved lens array to improve the image quality [139].

The Scheimpflug condition states that if the objective lens is tilted with respect to the object, then the detector must also be tilted with respect to both, the object and the lens such that the detector plane must pass through the line of intersection of the lens plane and the object plane [131,140]. This can be observed in the Scheimpflug FPM configuration shown in Figure 5.3 (b) (brown camera system). When this is satisfied, the tilted object plane will be in-focus as

seen in Figure 5.2 (b). An Anti-Scheimpflug condition is also shown in this figure to demonstrate the decreased DoF in a tilted scene image.

A comparison between a Scheimpflug FPM system, an on-axis FPM system and an off-axis FPM system is presented in Figure 5.3. Their experimental configurations are presented in sub-image (b) and their corresponding ZEMAX simulated PSFs are displayed in sub-images (a1-a3). It should be noted that the detector in the off-axis configuration is refocused to obtain best focus such that the PSF was sampled appropriately in the software. The imaging systems were simulated with the parameters used in the experimental setup described in the later sections of this chapter: the aperture diameter of the lenses was 8mm, the off-axis lens was placed 15.5mm from the centre and the working distance was 56mm.

The on-axis system shown in green is a conventional imaging system, hence the object, the objective-lens and the detector are all parallel to each other and centred on the optical axis of the system. This system provides ideal optical performance, which can be used as a reference to compare optical performance of the other imaging systems.

An off-axis system in a planar lens array configuration is shown in blue. The object, the objective-lens and the detector are all parallel to each other in this configuration similar to the on-axis system. However, the object and the detector are off-centred with respect to the optical axis of this system. Due to the off-centering, the image suffers from off-axis aberrations such as coma and astigmatism as observed in the PSF. The size of the PSF is increased drastically due to the aberrations. Since FPM is a coherent technique, it should be able to correct for these aberrations within the reconstruction. But, due to the approximations in the reconstruction procedures only a small part of the FoV is processed at a time. If the PSF extent is too big compared to the size of the image segment that is being processed, then the reconstruction suffers from artefacts despite having an ideal dataset. Hence, it is desired to correct for these aberrations experimentally.

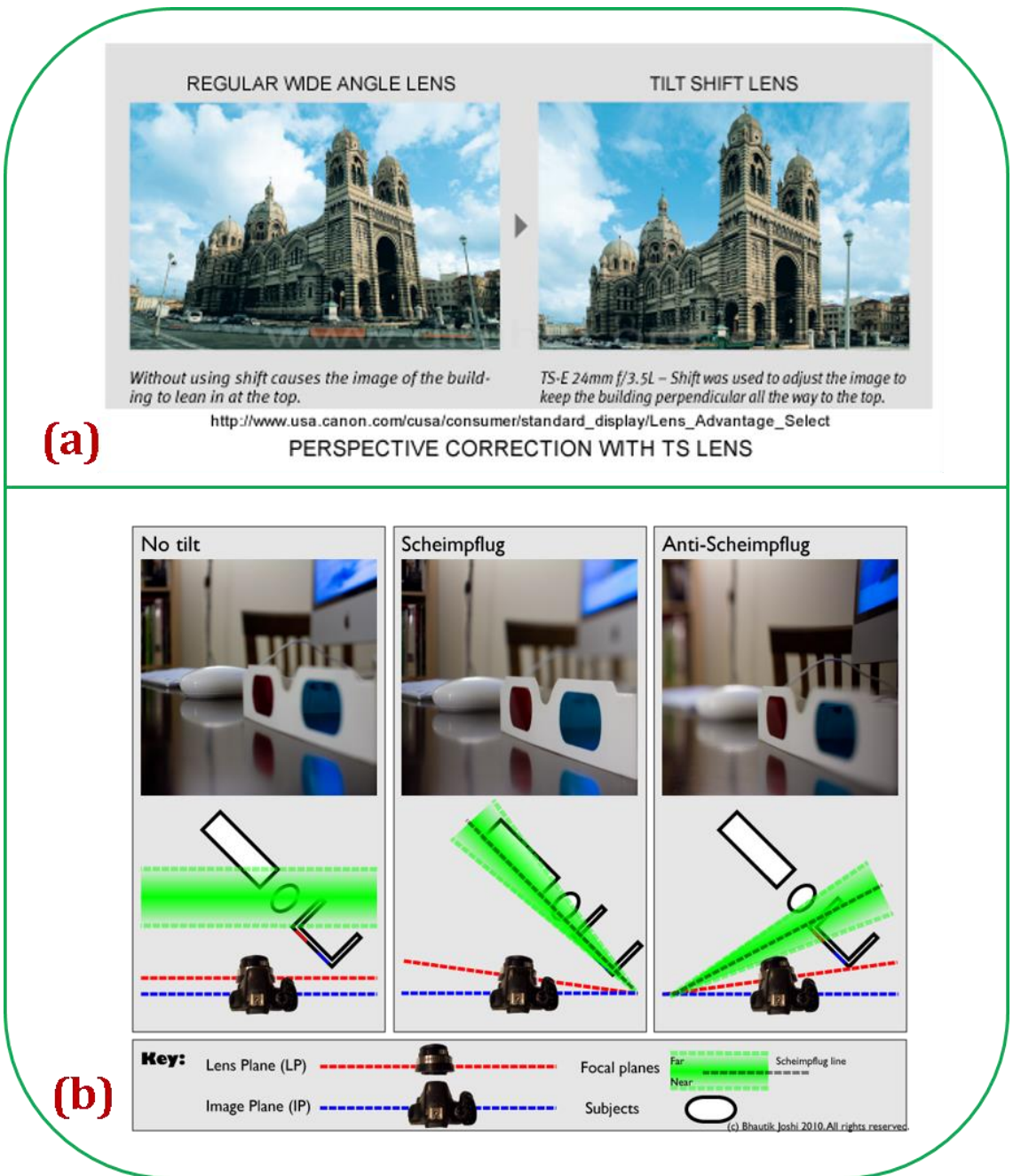


Figure 5.2 Scheimpflug condition example application.

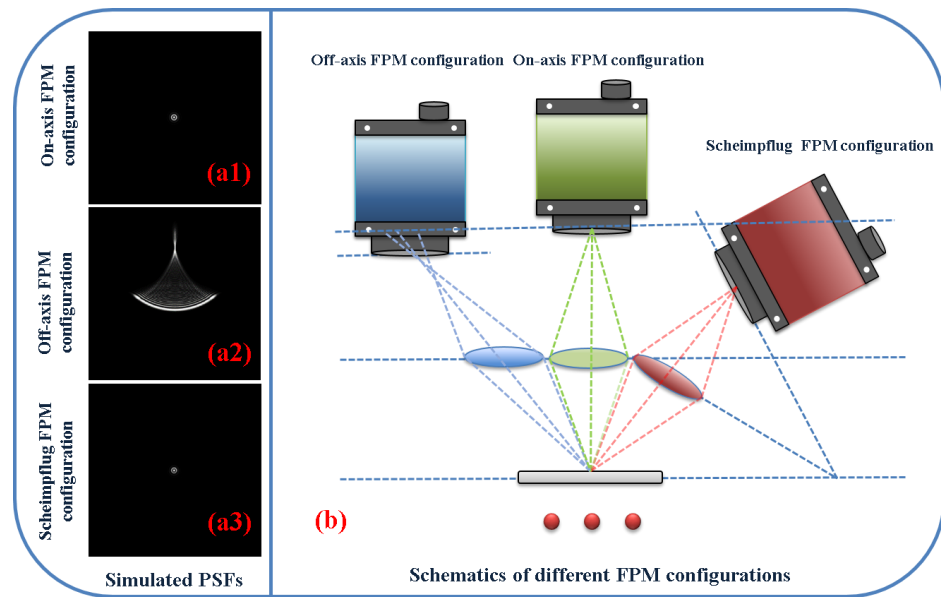


Figure 5.3 Scheimpflug FP setup geometry showing the positions of the imaging lenses and the detectors. On-axis and off-axis FP systems are shown for comparison. The PSFs of these systems are shown in a1-a3.

The optical model of a Scheimpflug condition FPM is different compared to a conventional on-axis setup. Hence, this needs to be studied rigorously to understand the implications in the reconstruction procedure for both S-FPM and SMA-FPM setups. In the next section an experimental setup built using 3D printed parts is described. In the following sections the forward model for Scheimpflug FPM reconstruction is discussed and a proof of concept experiment is presented.

5.3 Scheimpflug MA-FPM setup

In an on-axis or off-axis system there are only three degrees of freedom for each of the lenses and the detectors corresponding to the spatial position degrees of freedom. In a Scheimpflug condition, this increases to five due to additional degrees of freedom from the tip and tilt rotations (pitch and yaw). This increases the complexity of the system. In a planar array all the lenses can be placed in a single 3D printed part, similarly all the detectors in the array can also be placed in a single 3D printed part. The lens array can be moved for alignment, which aligns all the lenses with respect to their detectors. This effectively reduces the

degrees of freedom for alignment to two (axial translations) from $6n$, where n is the number of optical systems. In a Scheimpflug MA-FPM system, the lenses can be placed in a single 3D printed part. However, the detectors cannot be placed in a single 3D printed part. The angle of the detector is sensitive to the distance between the lens and the detector. Hence, in addition to the distance between the lens and the detector, the detector angle also needs to be adjusted. This results in $3n+1$ degrees of freedom for alignment from $10n$. A custom 3D printed setup with embedded kinematic stages is designed to address this problem. This section describes the details about the 3D printed setup and the parameters used in the experiment.

5.3.1 SMA-FPM design parameters

As discussed above, a Scheimpflug system has five degrees of freedom. Schematics of an off-axis Scheimpflug FPM system are shown in Figure 5.4. The variables corresponding to the lens and the detector positions shown in this figure are derived from the known variables such as the magnification of the system m_o , focal length of the lens f and the tilt of the curved lens θ_l . It should be noted that in this figure it is assumed that the on-axis system and the Scheimpflug off-axis system are in a 2D plane. Such plane can be identified for every off-axis Scheimpflug system and these parameters can be calculated in this plane. This is a simple rotation of the coordinate system around the optical axis of the on-axis system, which helps in simplifying the calculations.

In SMA-FPM, general parameters such as the number of cameras required, curvature of the lens array, the system magnification and the number of LEDs required are calculated as described in Chapter 3 for the MA-FPM configuration. They depend on the initial NA, synthetic NA and the targeted speed improvement. The curvature of the lens parameter is similar to the separation between the lenses in the planar MA-FPM setup, it corresponds to the required frequency shift from the off-axis system.

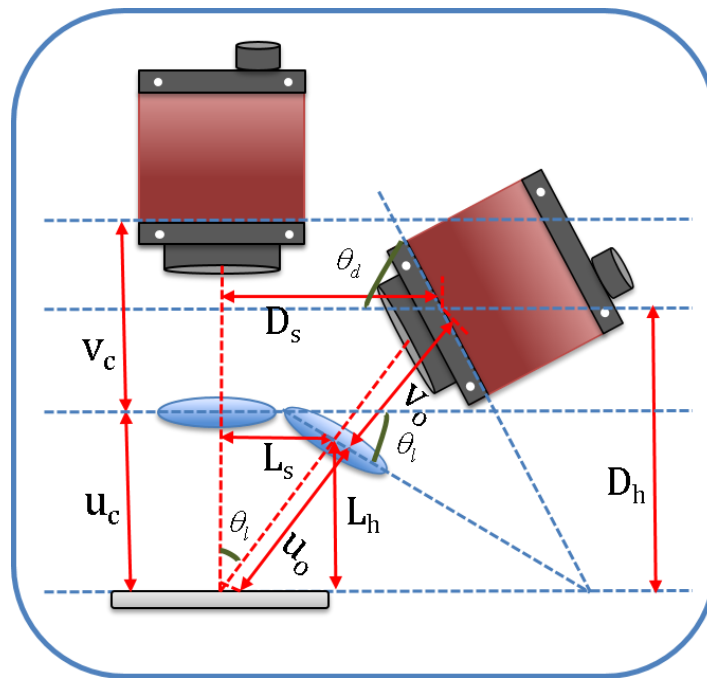


Figure 5.4 Scheimpflug setup schematics

In Figure 5.4 it can be observed that the lens and the detector require three variables each to localize their position. They are two translations (distance from the object and the shift from the on-axis system optical axis) and one rotation (tilt angle with respect to the object). The rotation of the lens θ_l is a known parameter, the remaining five variables to localize the lens and the detector position can be calculated from the geometrical arguments as given by the following equations:

$$L_s = \frac{1 + m_o}{m_o} f \sin \theta_l, \quad (5.1)$$

$$L_h = \frac{1 + m_o}{m_o} f \cos \theta_l, \quad (5.2)$$

$$D_s = \frac{(1 + m_o)^2}{m_o} f \sin \theta_l, \quad (5.3)$$

$$D_h = \frac{(1 + m_o)^2}{m_o} f \cos \theta_l, \quad (5.4)$$

$$\theta_d = \tan^{-1} \left\{ \frac{(1 + m_o) \cos \theta_l \sin \theta_l}{1 - (1 + m_o) \sin^2 \theta_l} \right\}, \quad (5.5)$$

where, L_s and D_s are the separations of the lens and the detector from the on-axis system optical axis respectively, L_h and D_h are the distances of the lens and the detector from the object plane respectively, θ_d is the angles of the detector with respect to the object plane.

These parameters can be used as the desired positions of the lenses and the detectors in the 3D printed setup. However, due to 3D printing manufacturing tolerances these positions can deviate. Hence, a robust alignment system for detector positions or lens positions is desired. The 3D printed setup described in the next sub-section describes the setup and the alignment system.

5.3.2 SMA-FPM experimental setup 3D-model

The SMA-FPM experimental setup consists of mainly four parts: The LED array, the object holder, the lens array and the detector array. These parts need to be mounted/aligned with respect to each other. In conventional method (such as in the last chapter), these are built from commercially available kinematic opto-mechanical components. With the advent of 3D printers, most of these are being replaced by custom, innovative 3D printed parts [48,121,141]. Similarly, in this work all the major mounts and stages are built from custom designed 3D printed parts. However, these 3D printed parts are made of plastic. Plastic has much higher expansion coefficient compared to metals, hence can change the alignment of the system with the surrounding temperature. Hence, in this work individual mounts for the four parts mentioned above are made from 3D printed parts, but they are assembled together with metal posts to minimize the thermal expansion.

In the SMA-FPM experiment, nine lenses and nine detectors are used. This creates 18 optical elements that needs to be aligned to achieve the targeted positions given by the equations from the previous sub-section, which can be challenging. To reduce the complexity, the lenses are placed in fixed positions calculated according to the above equations and only the detectors are moved for fine adjustment. This provides a simpler design and easier alignment.

In some microscopes, to focus the system the objective-lens is translated instead of the object itself. This can create minor changes in the optical setup which can often be ignored. But, in the SMA-FPM system this can be problematic since any changes in the object distance will create calibration errors. Microscope slides usually have small variation in the slide or the coverslip thicknesses, resulting in a change in the object position between the samples. This needs to be corrected by either moving the object or the lens-array and the detectors together. Moving the lens-array and the detectors would change the system calibration, including the image registration. Which would require separate calibration for each sample. Hence, this setup is designed such that the object can be moved to focus the system such that the calibration would remain the same between the samples. This means calibration is only required unless the lens-array or the detectors are moved, improving the usability of the system.

The final experimental setup consisted of several 3D printed parts created from ten different 3D designs. There are three crucial parts to describe the alignment of the system shown in Figure 5.5. These are (a) the detector array holder, (b) the lens array holder and (c) the detector case. These parts simplify the alignment of the 18 optical components.

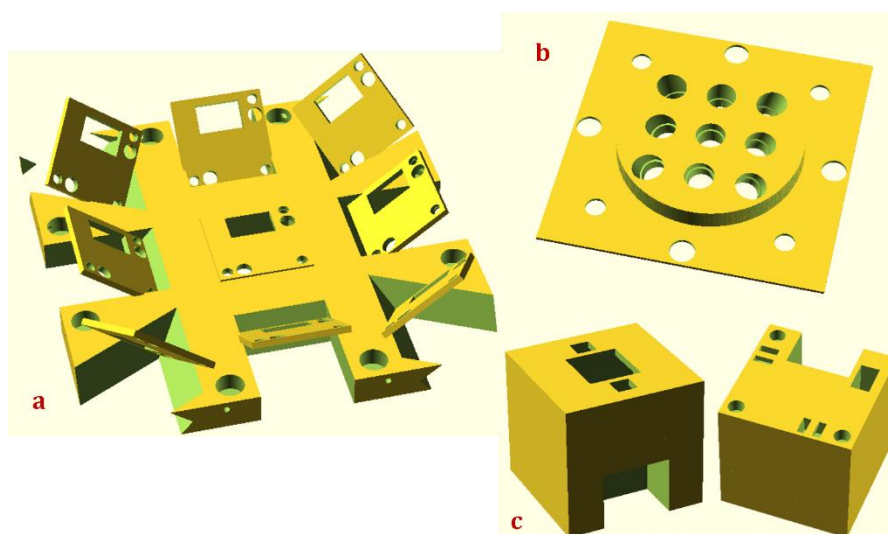


Figure 5.5 3D models of the setup parts. (a) Detector array holder (b) Lens array holder (c) Detector case

Lens array holder:

The lenses need to be immovable in the setup to minimise the system complexity as described before. This is achieved by printing a lens array holder as seen in Figure 5.5 (b). This holder is designed such that the individual lenses in the array will sit at a predefined angle. This angle is given by the SMA-FPM parameters calculated from the equations in the previous section. Each lens has an aperture at the front, which is faced towards the object. This aperture determines the pupil diameter in the object's Fourier space. The aperture shape and diameter needs to be of high-precision since they are crucial parameters for FPM reconstruction. The back of the lens (towards detector) does not have any aperture or closing. This is to avoid any vignetting in the image. The lenses are held in place with the friction between the lenses and the walls of the 3D print. This part can be mounted on another 3D printed stage to incorporate it into the setup.

Detector array holder:

The detector array holder is a stage where all the detectors can be mounted individually. This stage can also be connected to rest of the stages holding the lenses and the object using metal posts. This stage needs to support kinematic mechanism to align the detectors. Each of the detector is mounted in a custom case described below and mounted onto this stage. Each detector can be mounted onto a square plate like structure with several holes as seen in Figure 5.5 (a). These plates are tilted at an angle such that when the detector is mounted, it will be located approximately at the angle required for the Scheimpflug condition. The detector holder plate contains two large circular holes on the sides where two springs will be passed through and held at the back using 3D printed support pins. Bushings with 0.2mm pitch internal threads are mounted in the three small holes on the corners of each plate. These bushings will let the 0.2mm fine pitch *Thorlabs* screws through to the back of the detector case. The rectangular hole on the plate will let the camera USB connector cable into the detector.

Detector case:

The detector case shown in Figure 5.5 (c) enables a 3-axis kinematic mount embedment onto the detector. This case has three small holes at the back such that the screws can sit and push the case. Tiny magnets are glued inside these holes so that it attracts the round-tip of the screw and provides some tension to reduce any motions due to vibrations. The two double-slit structures present at the back of the case have hollow space underneath them. The springs are latched onto the detector case using these double-slit structures. The springs pull the detector case towards the square plate on the detector array stage and the screws pushes it away. This keeps the necessary tension in the system to provide stable alignment of the detector. The springs also help minimizing the backlash error in the kinematic mechanism. The detector sensor is situated in the front of the detector case, hence by increasing the back length of the case, the sensor can be moved closer towards the lens. This is helpful in mounting the detector approximately close to the in-focus position.

The detector has 3 degrees of freedom, the focus translation and the tip, tilt angles. Hence the kinematic design should have three adjustment knobs. This is provided by the three screws sitting behind the detector as described before. Thorlabs screws with 0.2mm pitch are used to generate high-precision movements. An Allan key is used to turn these screws to provide good control over the fine rotation. The kinematic stage design adopted here is a generic design [142], customized such that it embeds the detector and simplifies the experimental setup. With the implemented procedure, this setup provides a robust experimental alignment. The lateral XY positioning of the detector is fixed in the setup by its 3D printed position. However, this deviates from its expected position due to building errors. This is corrected in the post processing by registering the images from the off-axis Scheimpflug imaging systems with respect to the on-axis system.

5.3.3 SMA-FPM experimental setup

The 3D printed experimental setup picture after complete assembly is shown in Figure 5.6. For illumination, an *Adafruit* 32x32 LED array with 5mm separation between the adjacent LEDs is used. It is placed at a distance of 127mm from the object such that a 64% overlap is achieved to produce the necessary redundancy in the data captured. Same lenses used in the planar MA-FPM setup experiment are used as objective lenses - *Edmund optics* achromatic lenses with 36mm focal length - but with an 8mm clear aperture to provide an NA of 0.07, three times larger than the previous setup. The synthetic NA of 0.43 is aimed for by using 21x21 LEDs in the array with a single lens FPM or by using 7x7 LEDs in the array with 3x3 lens array with SMA-FPM. The off-axis Scheimpflug lenses are placed 15mm from the centre of the on-axis lens system to achieve the desired sampling of the object spatial frequencies. The magnification achieved was 1.75 in the central and off-axis systems.

Detector characteristics:

A USB 3.0 board level camera from *e-consystems* See3CAM_CU51 without lenses was chosen as the detector. This company was chosen particularly because it provides board level cameras which can be easily embedded inside a 3D printed case as shown before and are extremely cost effective. These cameras costed £140 each, much cheaper compared to any other existing cameras with similar performance. The pixel size on these sensors is 2.2 microns and they have a pixel responsivity of 1.4 V/lux-sec. These sensors contain 2592x1944 pixels resulting up to 5 Megapixel images. The camera board can provide 12-bit unprocessed images at 14 frames per second. In the reported setup, 9 cameras are implemented. Hence, this system can provide 9x14x5 (630) megapixels of data bandwidth per second. This is extremely large for its low cost. The sCMOS cameras in the market provide the highest bandwidth among the scientific cameras with 500 megapixels per second bandwidth, which costs around £8000. The total cost of the components for the reported setup was under £2000, hence making it an extremely cheap setup compared to the high-speed FPM with LED multiplexing system [5]. Additional lenses and cameras can be added onto our setup to further

increase its acquisition bandwidth, resulting in gigapixels per second bandwidth system.

Low-cost sensors usually suffer from large read noise. Hence, a study on the detector read noise is performed here to understand the noise statistics. In an sCMOS sensor the detector read noise is less than 2 electrons for a well capacity of 30000 electrons, equivalent to a standard deviation of 0.28 for a 12-bit dynamic range image. Hence, the dominant noise in the images captured by sCMOS cameras is from the photon shot noise. They are also often cooled so their temperature doesn't fluctuate resulting in steady dark current (around 10 counts in a 12-bit image) and read noise. Cheap sensors however, does not have cooling systems hence produce varying dark current and suffer from higher read noise. A table with the detector read noise and the dark current for two sensors in the array is shown below. The detector can go to a maximum of 10 seconds exposure, so the noise statistics were observed for few different exposure times.

From this table it can be observed that the noise statistics change between the cameras but stay approximately close to each other. The detector read noise at one of the lowest exposures is around 2.5 counts and it increases up to 5 counts at longer exposures. The increase in read noise is expected due to the increase in thermal current and other read electronics. It was also observed that at exposures higher than 500 milliseconds the read noise increases with increasing number of acquisitions. The number quoted above is an average for 10 snapshots at each exposure. The detector dark current at 8 milliseconds is 169.25 and at 1.8 seconds is around 190. The increase in the dark current is also due to the thermal effects. If the detector is heated due to room temperature, then it is expected to have increased dark current and read noise. The temperature in the lab was set to 22 degrees Celsius when this data was recorded.

Table 1 Detector read noise and dark current (all counts are for 12-bit images)

<i>Exposures in milliseconds</i>	<i>8 ms</i>	<i>80 ms</i>	<i>200 ms</i>	<i>500 ms</i>	<i>1000 ms</i>	<i>1800 ms</i>
<i>Camera 1 Read noise</i>	2.56	2.66	2.83	3.28	3.59	4.42
<i>Camera 1 dark current</i>	169.25	169.5	170.2	172.65	176.8	183
<i>Camera 2 Read noise</i>	2.7	2.88	3.2	3.45	4.55	5.57
<i>Camera 2 dark current</i>	169.25	169.8	171.6	176.25	184.5	196

When compared to the sCMOS cameras, the read noise is ten times higher for the detector we are using. The dark current is also much higher. However, the total noise in the image is contributed from both the read noise and the photon shot noise. When compared to the photon shot noise, the detector read noise is much lower in images with large signal counts. For e.g., if the image has a peak signal count of 3000, then the shot noise is 54.77 counts and the read noise is 2.75 counts (at low-exposures), which results in a peak SNR of 52.15. This is only a 5% drop in shot noise SNR and the effective SNR is still high, hence the system can be considered as shot noise limited [103]. The detector read noise can be a problem when the signal count drops and the shot noise SNR is very low. In such cases the detector read noise can result in a significant contribution. For e.g., for a peak signal count of 100, the shot noise is 10 and the read noise is 2.75. The effective SNR will be 7.8, a 22% drop compared to the shot noise SNR. In such situations either the exposure can be increased or the amount of light illuminated can be increased. In FPM, the off-the-shelf LED arrays have very less brightness and the illumination intensity drops due to the planar array shape. However, this can be

easily improved by using high power LEDs and curved arrays [92,128] or using laser illumination [103,143].

The dark current is around 180 counts in a 4096 image, hence the effective dynamic range is still very high (~3900). These detectors usually have lower electron well capacity compared to the sCMOS sensors, which can provide larger dynamic range (16 bits). However, this can be solved by using either varying exposures or varying illumination intensities in an experiment as performed in the experiments in this work. In the SMA-FPM setup, a lower exposure can be used for the central camera and higher exposures can be used for the off-axis cameras. Provided the illumination is sufficiently bright, this setup can record the data at the camera full frame rate. Considering all the factors discussed so far, it can be concluded that these detectors have sufficient performance to be implemented in FPM setups, especially in SMA-FPM setups for high speed data acquisition.

3D Printing:

An *Ultimaker 2+* 3D printer was used to print all the 3D parts used in building this setup. A nozzle size of 0.4 millimetres diameter was used for printing all parts except the lens array holder. A 0.25 millimetres diameter nozzle was used for lens array holder such that higher resolution can be achieved in printing the apertures. However, the printed apertures still suffer from minor irregularities. The final printed aperture diameter can also vary from the design value, which can also introduce artefacts in the recovered image. This can be minimised by making this part from methods with higher manufacturing precision such as CNC machining. For most of the printing black PLA material was used, except for few parts of the stages where silver PLA was used. PLA is a biodegradable plastic widely used in filament deposition based 3D printers. It costs around £25 per kilogram of the material. Approximately 1.5 kilograms of PLA was used in printing all the parts in the setup, costing under £40 for the material.

OpenSCAD software was used for designing all the CAD models of the parts [144]. This software is a free opensource CAD software which uses programming interface to build 3D CAD models. The equations for calculating the

lens positions were written in the CAD file and the software automatically calculated the lens positions from the input parameters and positioned them at the corresponding locations in the required orientation. The CAD files are rendered and corresponding STL files are exported. These STL files are fed into *CURA* software, an opensource software for creating files for 3D printing machines [145]. This software generates a GCODE file, which can be inserted into the printer using an SD card for printing. The settings used in the *CURA* software can determine the print quality. Details about these settings and tips on generating a good quality print can be found on the manufacturer's website [146].

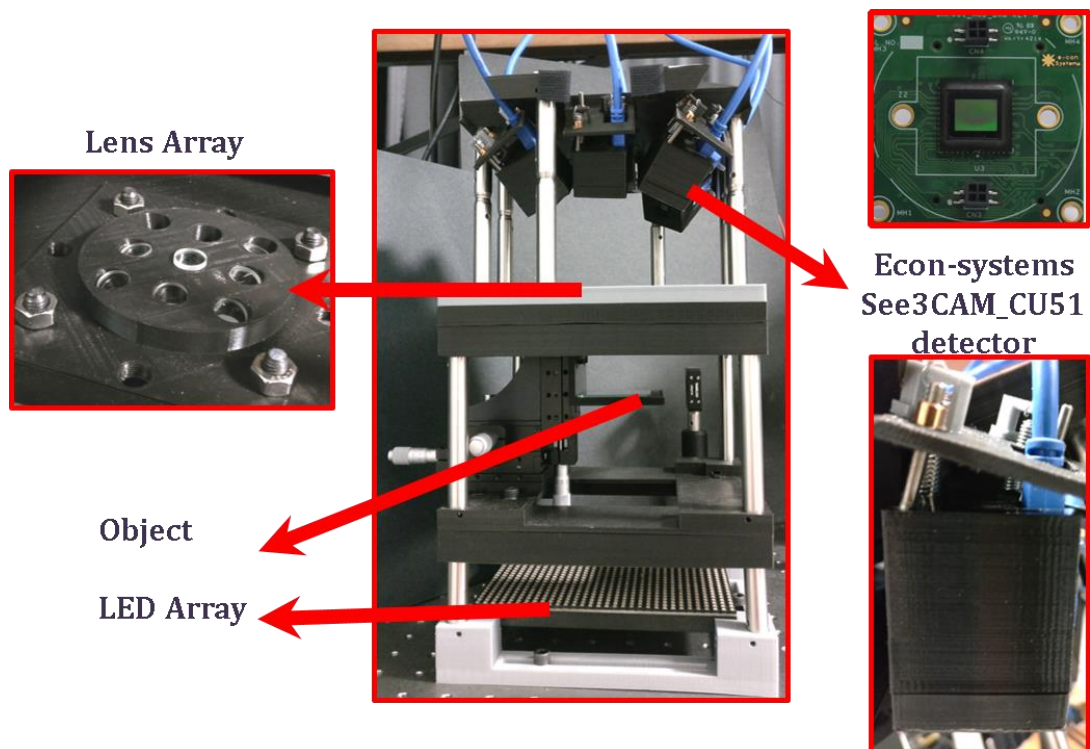


Figure 5.6 Assembled 3D printed experimental setup

Assembly and alignment:

The final assembly of the experimental setup is shown in Figure 5.6. It can be observed that the setup consists of four stages, one for each of the four sections in the setup. The first part is the LED array situated at the bottom of the setup. A 3D printed stage holds the LED array in place with friction as seen in the figure. This stage is screwed onto the optical bench with the help of the grooves

incorporated into the base of the stage. This keeps the setup stable with respect to the optical bench. There are four holes on top of the stage for half inch metal posts to be embedded. There are grooves on the sides of these holes for grub screws to keep the posts attached to the base.

The second part is the object stage located above the LED array as seen in the figure. This stage is made from two parts such that the thickness of the bottom part can be modified to change the height/distance of the object stage from the LED array. These two parts also have four holes each for mounting the posts as seen in the figure. These metal posts usually come in standard lengths, so to achieve the required separation the thickness of the stage is utilised. The object is mounted on a 3-axis *Thorlabs* translation stage, which allows XY positioning and Z focusing of the object. A 3D printed 3-axis translation stage can be used instead of the commercial stage used in this experiment to decrease the costs. A commercial stage was used to save the time in designing and printing the stage.

The third part is the lens array stage located between the object stage and the detector stage. This stage is made from three parts in the current setup, however, this can also be made from two parts as described for the object stage. The lens array holder described in the previous sub-section is highlighted in the inset of Figure 5.6. This is screwed on to the lens array stage using screws. This piece can also be embedded into the lens array stage, but it would require the whole part to be printed at high-resolution, resulting unrealistic times for printing. Hence the lens array holder is made as a separate part. The bottom of the stage has four holes for the posts, but the top has eight holes on the sides instead of the corners. This is due to the shape of the detector array stage.

The fourth part is the detector array stage located on the top. The design of this stage is described in the previous sub-section. The detectors mounted onto this stage can be seen in Figure 5.6. The kinematic mechanism on the detector case is shown in the inset on the right. The board level camera used in the setup is also presented. The detector case is made of two parts, the front case and the back case. The detector sits between these two cases and held in position by

friction. The detector case is moved by the screws to move the detector. The detector stage is mounted on the eight posts coming from the lens array stage.

To align the system, first all the parts are assembled in the order as described above. This results in an approximate position of the detectors, the lenses and the object. In this setup the moving parts are the nine detectors and the object. A dots array slide is used as the sample for initial alignment of the system. First the object is moved in Z so that it appears roughly in focus in the central detector using the central LED illumination. Then the central detector is adjusted using three screws to get perfect focus in the centre of the FoV. Then the illumination is switched to an off-axis LED such that bright-field images can now be seen in the off-axis detectors. These detectors are then fine adjusted to achieve sharp focus in the same section as the central FoV on the central detector. This completes alignment of the system. A different sample such as a USAF resolution chart is mounted and the object Z stage is adjusted to make it appear in focus in the central camera. This should automatically focus the images in the rest of the detectors, which verifies the alignment of the system. This system alignment is observed to be stable for few weeks if the detectors are not disturbed. A calibration performed on this aligned system will, hence remain unchanged over this period.

5.4 Scheimpflug configuration recovery model

The optical model in a Scheimpflug conditioned setup has variations compared to a conventional optical setup. However, with some approximation both of their optical models can be related. In such conditions the FPM recovery using conventional Fraunhofer propagations can be used. These approximations are discussed in this section with their limitations.

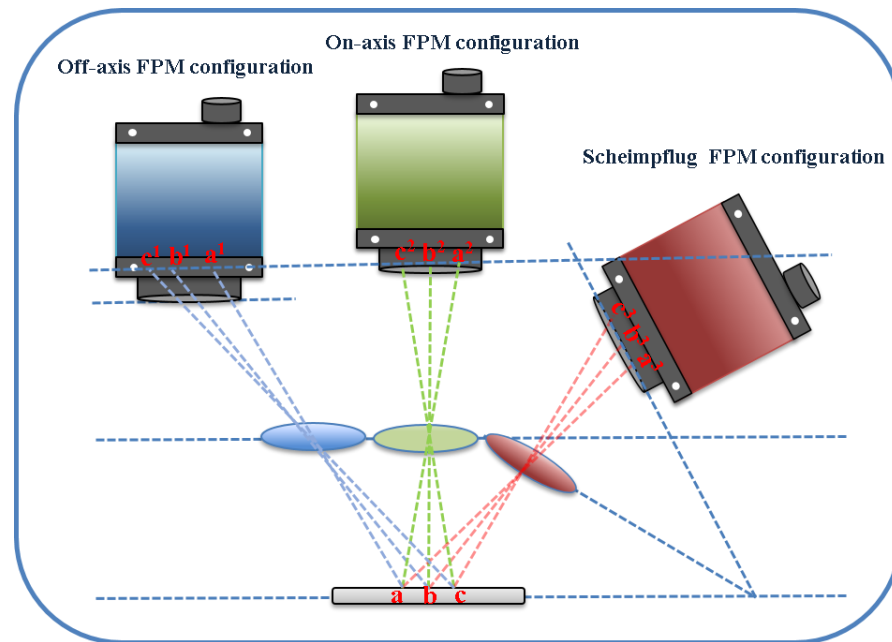


Figure 5.7 Comparison of distortion and NA variation in the FoV between different imaging systems.

The key variation of a Scheimpflug setup compared to a conventional setup is the tilt of the objective lens with respect to the object. The tilt increases the objective lens distance from the object in a non-symmetrical fashion. This induces a distortion, which is minimised by Scheimpflug conditioning the detector. However, there is residual distortion due to the varying object distance across the FoV, resulting in a spatially varying numerical aperture, hence resulting in a spatially varying DoF. This can be observed in Figure 5.7 and Figure 5.8. This variation needs to be addressed in the FPM reconstruction procedure to achieve robust reconstruction.

Distortion:

In Figure 5.7, three periodic points in the object are imaged under various FPM configurations discussed so far. In an ideal imaging system, the points in the image will also be periodic and scaled according to the magnification. In conventional on-axis imaging systems, barrel or pincushion distortion can be observed due to the changing distance of the object across the FoV. The barrel or pincushion distortions are symmetric around the optical axis, hence c^2b^2 and b^2a^2 will be

equal. In off-axis imaging systems (both planar and Scheimpflug), there will be non-symmetrical barrel or pincushion type of distortion. The distance from the object of the point 'a' in the object is different compared to the point 'c' in the object. This makes the distortion non-symmetric. The tilt in the distortion depends on the direction of the tilt and shift of the off-axis lens. Hence c^1b^1 is different to b^1a^1 and c^3b^3 is different to b^3a^3 .

In low-NA imaging systems, the distortion in the images is small and can be ignored. In the planar MA-FPM experiment reported in the previous chapter, the distortion in the images is ignored due to the low-NAs involved. However, this could impose limitations on the maximum FoV that can be imaged. This can explain some of the minor artefacts observed in the edges of the FoV in the MA-FPM recovery in Chapter 4. In high-NA imaging systems the distortion is severe and can degrade the FPM image reconstruction if not addressed properly. In MA-FPM systems, the distortion variation in the individual imaging systems needs to be considered and their contribution to the resulting MA-FPM reconstruction.

Distortion is purely a geometrical phenomenon, when the aberrations are ignored. The distortion in the image can be inverted computationally by inverting the geometrical transformation applied by the optical setup, if it is known. The geometrical transformation due to the optics can be measured by using a periodic grid array of dots with known separation as the object. The image of the dots grid array object will have the separation between the points distorted according to the geometrical transformation of the optical system. By comparing the actual spacing to the achieved spacing in the image, a geometrical transformation relationship can be obtained. This transformation can be applied on all the images captured to correct for the distortion. Similar distortion correction can also be applied to the off-axis imaging systems under the Scheimpflug condition. It should be noted that this method only corrects for distortion in the images but not the aberrations or the field-curvature. Aberrations can be corrected independently within the reconstruction using pupil recovery. Field-curvature can shift the LED positions from the expected values [79]. This can be corrected by implementing LED position correction methods discussed in the second chapter [91,92].

Numerical aperture variation:

The varying distance of the off-axis points from the objective lens also changes the NA of those points. This can be understood by observing the cone angle of the light collected from those points (a, b and c in Figure 5.7). Depth-of-field depends on the NA; hence it is also varied across the FoV [130,147]. In Scheimpflug condition, the DoF has a wedge shape as seen in Figure 5.8. DoF however, doesn't have any influence on the FPM recovery. It only provides the tolerance in the alignment of the detector in the Scheimpflug condition. The NA on the other hand is a crucial parameter that needs to be corrected in the FPM recovery.

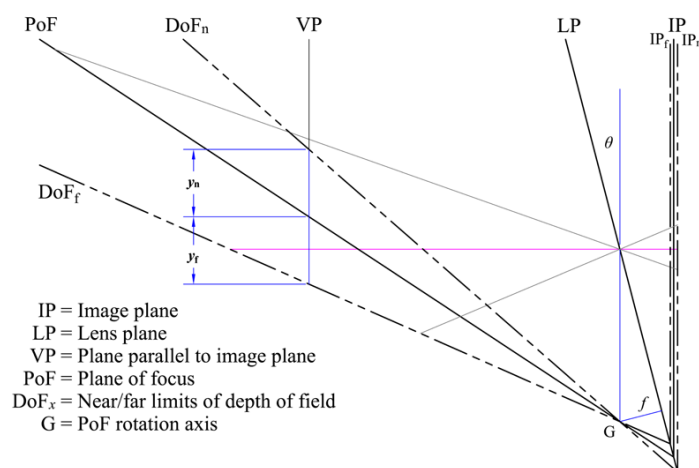


Figure 5.8 DoF in a Scheimpflug condition setup. Image taken from [148].

The spatially varying NA and the frequencies sampling in the on-axis system can be corrected by using Fresnel diffraction based forward model and dividing the image into segments smaller than the partial coherence limits. In off-axis Scheimpflug systems, similar approach can be implemented. However, the lens and the detector planes are tilted, hence this requires advanced Fresnel diffraction propagation algorithms. To simplify this problem a Fourier transform based forward model can be used by dividing the image into segments such that the Fourier transform forward model is valid in this segment size. Within this segment size, the NA and the frequencies sampled can be considered spatially invariant. However, the NA and the frequencies sampled should be calculated

separately for each of these sections. The NA can be changed in the reconstruction process by modifying the pupil diameter accordingly. The frequencies sampled can be implemented by correcting for the pupil position according to the calculations. These corrections should provide robust FPM reconstruction.

SMA-FPM reconstruction:

In SMA-FPM, the NA, the distortion and the field-curvature at a particular position in the object will be different for the individual imaging systems. However, if they can be calibrated for individual imaging systems using FPM calibration datasets as performed for MA-FPM experiment in the previous chapter, then the SMA-FPM recovery can be performed using the algorithm described for MA-FPM in chapter 4 by using these calibrated parameters. The distortion between different cameras can be corrected by registering them with respect to each other, the field-curvature can be corrected by calibrating for the effective LED positions using self-calibration method and the NA variation can be applied by changing the pupil diameter for the imaging systems in the recovery. These approximations and methods should enable the SMA-FPM reconstruction using Fraunhofer propagation based forward model. The major limitation due to this forward model is the size of the image segment that is processed. The image segment size cannot be made arbitrarily small due to the resulting aliasing effects in the pupil plane. Hence, implementing a Fresnel based forward model would be ideal. This would require developing Fresnel propagations between tilted planes, hence is suggested as a future work.

It should also be noted that the object distance variation over the FoV is dependent on the working distance and the system NA similar to the spatial frequency sampling variation demonstrated in Chapter 3. Hence, a longer working distance system will have slower variations compared to a smaller working distance system. Also, in practice it is observed that the object distance variation is slow in FPM systems due to the small magnifications involved. This can be observed in the experimental images obtained in the next section.

5.5 Scheimpflug FPM experiment

A SMA-FPM experimental setup was built as described in the previous section. Due to the limited available time, a complete SMA-FPM experiment couldn't be performed and left as future work. To demonstrate the validity of Scheimpflug condition for FPM, a calibration FPM dataset is acquired for all the cameras in the system and an FPM recovery is performed on these datasets. The preliminary results are shown in this section.

A 32x32 Adafruit P5 LED array was used for illumination. The experimental setup was designed to use 21x21 LED arrays for an FPM dataset from the on-axis data to produce equivalent NA to SMA-FPM synthetic NA using 3x3 cameras and 7x7 LEDs. Hence, only 7x7 LED sets were available for off-axis imaging systems' FPM datasets. These 7x7 LEDs ideally should produce identical frequency content in the off-axis FPM datasets but due to the planar LED array design, they produce significantly different spatial content.

System alignment:

A 20 μ m diameter dots array sample is imaged using the experimental setup. The low-resolution full FoV raw images recorded by three cameras in the setup are shown in Figure 5.9. In these images it can be observed that they all are focused to produce best resolution and image quality. These images have minimal aberrations and the distortion tilt from the tilted lens design is also small. This is also evident in the cropped low-NA images of the USAF resolution chart images shown in Figure 5.10. However, the achieved positions of the experimental images on the detectors are very different from the design. According the design, the raw images on the detectors should look identical and should not have much translations or rotations. However, due to deviations of the experimental setup from the design, the experimental images on the detectors are rotated and translated. This suggests that the individual imaging systems are not at the designed Scheimpflug condition, but at a different Scheimpflug condition. This variation can produce artefacts in the reconstruction as observed in Figure 5.10.

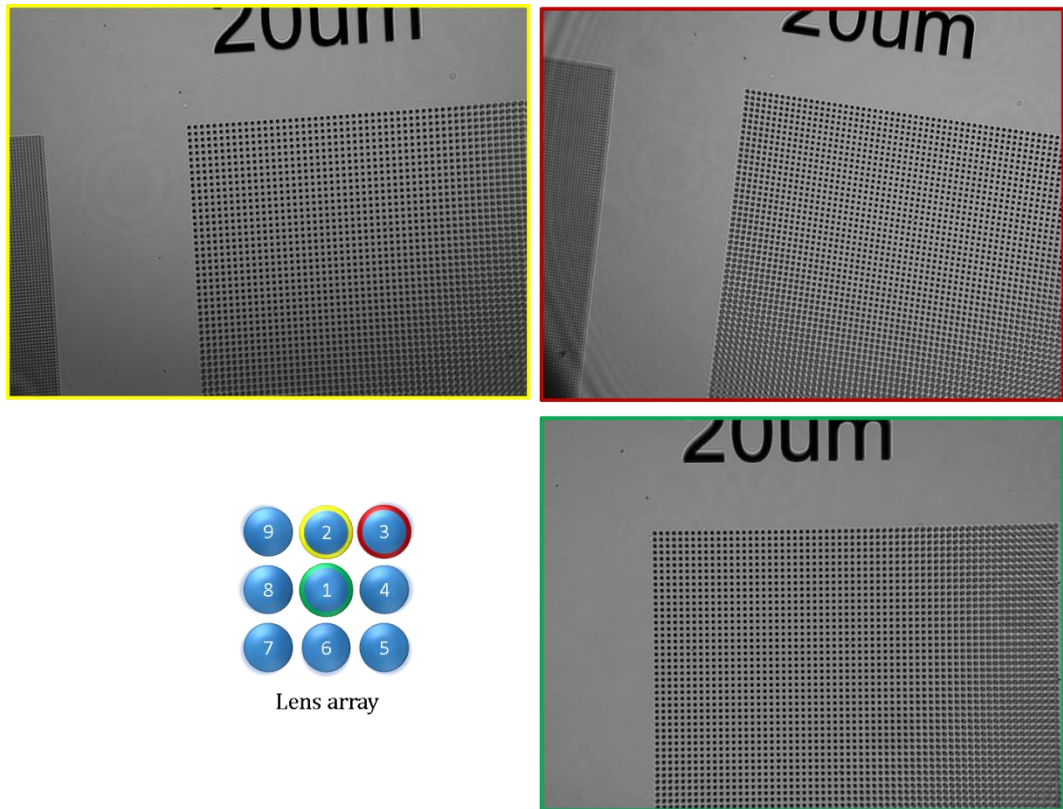


Figure 5.9 Raw captured full frame images.

For the S-FPM reconstruction of the off-axis cameras, the images are registered with respect to each other prior to reconstruction. Even though this is not necessary, performing this would provide the calibration data that can be directly used in SMA-FPM recovery. Image registration is performed by registering the images of the dot array sample shown in Figure 5.9. The images are binarized by thresholding and the centres of the dots are then calculated. A geometrical transformation matrix is calculated by fitting a transformation to the localized positions of the dots from two images from two detectors. This geometrical transformation matrix can be applied to all the images obtained by the detectors to register the images. This program was written in *Matlab*. Most of the above-mentioned operations were implemented by using computer vision toolbox in *Matlab*. The low-resolution images shown in Figure 5.10 were obtained after registration.

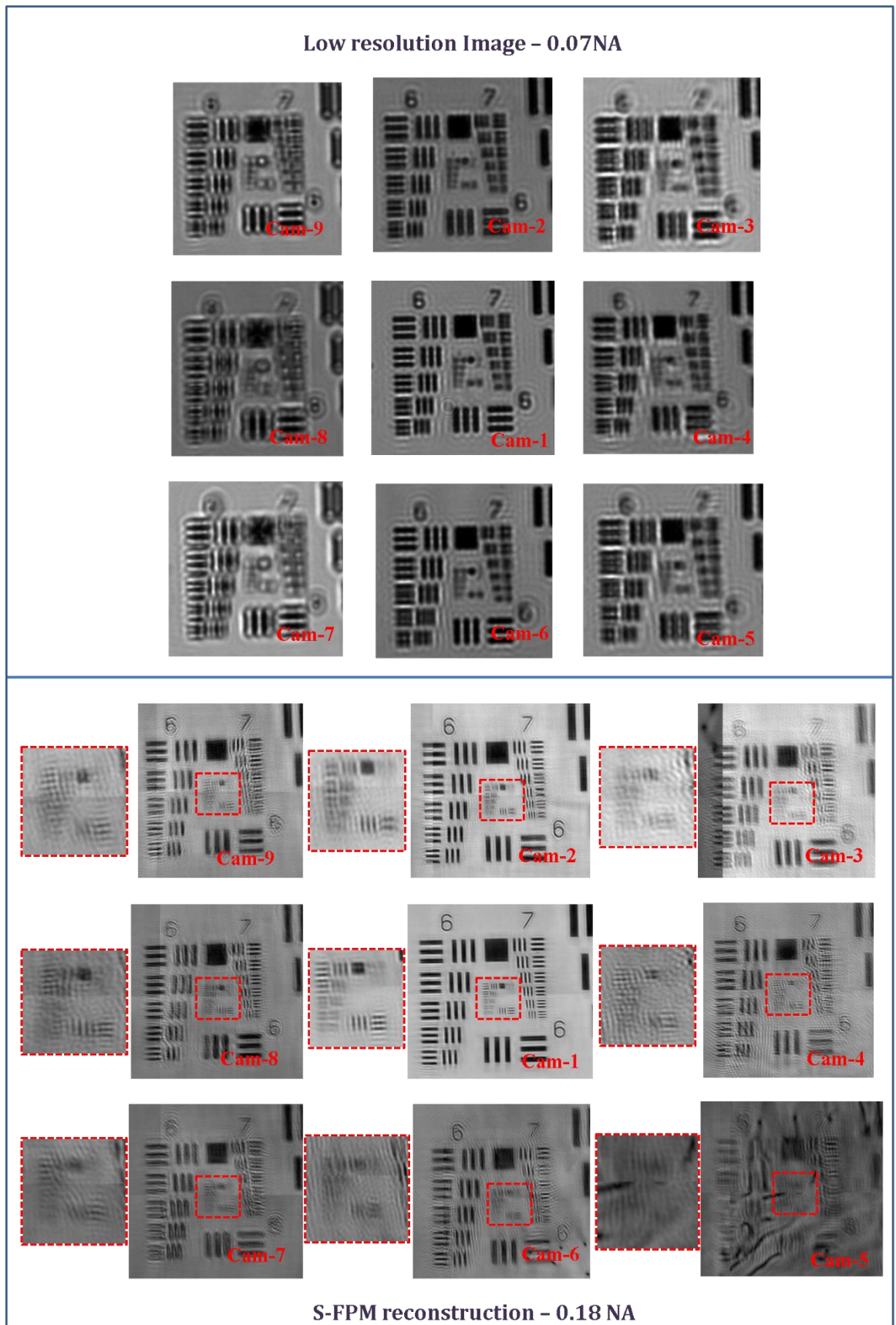


Figure 5.10 S-FPM reconstructions of a USAF resolution chart

S-FPM results and discussion:

S-FPM results from all the cameras in the SMA-FPM setup are shown in Figure 5.10. Low-resolution images are shown in the top section and their corresponding reconstructions are shown in the bottom section. The images from the cameras are arranged in a 3x3 grid to show the position of the camera in the 3x3 lens array used in the experiment. In this grid, the systems in the corners have larger tilt compared to the systems in the edges.

From the results, it can be observed that the reconstruction of Cam-1 is of highest quality. Cam-1 is an on-axis FPM system, hence should produce ideal FPM recovery. Cam-2 reconstruction is the next best among all the other off-axis imaging systems. The recovered image quality is very close to Cam-1 recovery. The group 8 elements 1 and 2 are resolved in both images. There are some minor artefacts due to calibration errors. The recovery of Cam-5 has severe artefacts in the recovered image and other cameras also have mild to moderate artefacts in their corresponding recovered images. In most of these cameras, it can be observed that the high-frequency features are recovered. Hence, it demonstrates that a Scheimpflug conditioned system can be used for FPM. The artefacts in the reconstruction are due to calibration errors. These can be corrected by developing calibration methods specific to these setups.

In the results, a correlation has been observed between the deviation of the image position on the detector compared to the central camera image and the artefacts in the recovered images. The deviation is caused by change in the experimental parameters, hence in systems with higher deviation, severe artefacts were observed in the recovered images. This can be improved by achieving better accuracy in the experimental setup assembly. The deviations affect the FPM recovery in two major ways, LED positions and the pupil aberrations. The LED positions can be calibrated by using self-calibration type of methods. The pupil aberrations can be recovered within the reconstruction but would require more LEDs in the array.

There are other factors identified as possible sources for artefacts. They are described as follows with proposed method of correction. First, the experimental setup can be printed and assembled such that the images recorded have less deviations. Printing the parts for the experiments setups with parameters for closest replication would require several iterations in practice. Since the printing times of the parts in the setup were long and there was not enough time left in this project, this was not achieved, hence this is suggested as future work. Once the parameters for closest replication are achieved, they can be used to build copies of the setup without any modifications. Hence, this is a one-time development step. The lens array holder is designed to not use any supporting material while printing, hence this produced a tube structure in the front of the lens aperture. This can cause vignetting when imaging large FoV segments. A dome shaped lens array holder design can avoid this vignetting. The lens array holder is the most important part of the setup and requires high quality printing. Hence, it is suggested to manufacture this part from CNC machining technology. It was also observed that the detector case holders couldn't hold the detectors with friction very well. Few of the detectors were not attached to the detector case strongly, hence had low-frequency ($\sim 0.2\text{Hz}$) vibration motions, contributing to the artefacts in the reconstruction [149]. It is suggested to screw the detectors into the detector cases to avoid these motions. A quasi-dome LED array is suggested for illumination instead of the planar LED array to provide more LEDs for calibration, providing better aberration estimates. These suggested improvements along with the LED position calibrating algorithms [91,92] should remove the artefacts in the presented results.

5.6 Summary

This chapter introduced a new experimental configuration for MA-FPM application. A curved lens array was proposed instead of a planar lens array for better coverage of the recorded object spatial frequencies. The Scheimpflug condition was implemented in the off-axis imaging systems to minimise the aberrations and the distortions experimentally. Scheimpflug condition requires a complicated experimental setup. Hence, an experimental setup was designed using 3D printed

parts and kinematic stages to simplify building such setup. The parts required for building the setup cost less than £2000, making this a low-cost system. A low-cost board level monochrome detector costing less than £150 was used as the sensor to reduce the SMA-FPM setup cost. A noise analysis of this detector was performed and compared to the noise performance of a scientific grade sCMOS camera. It is concluded that when there is sufficient light in the recorded image, these systems are shot noise limited, hence comparable to the noise performance of the sCMOS sensor. This is true for most of the modern CMOS cameras when the system is not photon starved. The 3D printed setup suffers from alignment errors due to the manufacturing process. These can be corrected by using advanced calibration algorithms reported in the literature review. Once well calibrated, this system is found to be stable and the calibration can remain unchanged for extended periods of time when the system is left undisturbed.

The forward model for the Scheimpflug FPM setup was discussed. The residual distortion across the FoV from the Scheimpflug condition was observed to be small. This distortion can be corrected by geometrical transformation of the image computationally. The NA variation across the FoV is also studied in the Scheimpflug setup and it is concluded that this can be compensated by changing the pupil diameter accordingly in the reconstruction process. These approximations suggest that a conventional Fraunhofer based reconstruction model is sufficient for processing the data from a Scheimpflug FPM system. This is validated on the off-axis imaging systems on the SMA-FPM setup. It was observed that the Fraunhofer model provided acceptable reconstruction quality, however, some artefacts were observed due to errors in the system calibration. These can be corrected by using self-calibration algorithm proposed in the literature. Improving the calibration and the SMA-FPM experimental validation is left as the future work.

Chapter 6 Conclusion and future work

In conclusion, a novel microscopy technique with parallelized data acquisition capability is proposed which can provide bright-field, dark-field and phase-contrast imaging modalities. This technique was inspired from Fourier ptychographic microscopy; hence it is termed as Multi-aperture Fourier ptychographic microscopy. This system can provide large FoV images with high resolution and has extended DoF. Over the course of this work, following things were developed:

MA-FPM theory:

The theory to parallelize the data acquisition in FPM was conceptualized. It was demonstrated that using multiple objectives and detectors, a large bandwidth of spatial frequencies can be captured in a single snapshot. However, it was shown that despite closest packing of objectives, all the spatial frequencies cannot be recorded and the data redundancy required for FPM reconstruction is lost. Hence, an LED array is used to sample the missing spatial frequencies and obtain the required redundancy. A design is proposed where an optimised set of objective lenses and LEDs is chosen to achieve required data acquisition speed without increasing the complexity of the system. This design also enables implementation of the LED multiplexing scheme in the MA-FPM experimental setup. To conclude, MA-FPM theory developed here provides a solution to realize large SBTP systems in microscopy.

Fresnel diffraction forward model:

In the MA-FPM theory it was recommended to use Fresnel diffraction propagation model for MA-FPM reconstruction instead of the conventional Fraunhofer based propagation model. Hence, a reconstruction algorithm based on Fresnel diffraction integrals was developed. The sampling criterion in this method was also discussed and it was concluded that this is satisfied in the Fresnel model reconstruction algorithm. Experimental data were processed using both Fresnel and Fraunhofer reconstruction methods. It was concluded that both algorithms work well when the size of the processed image segment is small. However, when larger image segments are processed the Fresnel model outperforms the Fraunhofer model. This is due to the small FoV approximation inherent in the Fraunhofer model. This approximation is not reported in the literature, but the image segments processed in FPM literature were found to obey this limit unintentionally, hence these artefacts were not reported. To conclude, Fresnel algorithm developed here provides better modelling of the imaging system compared to the Fraunhofer model. When an accurate Fresnel model cannot be developed for an imaging system, the Fraunhofer model can be used for reconstruction, however, the approximation mentioned here needs to be considered to calculate the size of the image segment being processed.

MA-FPM experimental validation:

An experimental setup to simulate an MA-FPM system was built by translating an objective lens and a detector. The design of this setup involved 3x3 lenses placed in a planar array, hence resulting in nine times improvement in data throughput. In MA-FPM, the images from different cameras does not have any common features since they sample different spatial frequencies of the object. Hence, a calibration procedure was developed to perform registration between these imaging systems and calibrate their parameters. A USAF resolution chart was imaged using this setup and the resolution improvement was demonstrated. The MA-FPM reconstruction was compared to an equivalent FPM reconstruction and found to have similar reconstruction quality. It was observed that the MA-FPM reconstruction of high-frequency features had better contrast compared to the

FPM reconstruction. This can be due to the fact that the dark-field images in MA-FPM have better SNR compared to FPM images since the LEDs used for illumination in MA-FPM have low illumination angles. The illumination intensity of the LEDs drops as the illumination angle increases, hence smaller illumination angles in MA-FPM results in higher illumination intensity providing better SNR. A microscopic slide was also imaged to demonstrate the high-quality reconstruction over the FoV of the image. Few minor artefacts were observed towards the edges of the FoV. These can be due to the aberrations and field curvature on the edges, which can be corrected by using advanced calibration algorithms discussed in the literature review.

Scheimpflug MA-FPM experimental setup:

A new experimental setup has been later developed to minimise the aberrations encountered in the previous setup. An MA-FPM experimental configuration was designed based on Scheimpflug condition. This condition requires a complicated experimental setup even for a single objective lens system, this would create a complex setup for the SMA-FPM system. Hence, an experimental setup has been designed using custom designed 3D printed parts. This design simplifies the experimental setup and provides robust alignment. A low-cost CMOS detector was used to reduce the component cost of the setup. An analysis was performed to study the read noise of this detector compared to a scientific grade sCMOS detector. It was concluded that both detectors have similar image noise when the imaging system is not photon starved. The final experimental setup costed less than £2000, much less compared to systems reported with similar SBTP.

Scheimpflug FPM forward model:

The Scheimpflug condition introduces new variables in the optical setup, hence the forward model for image process formation will be different. Two key variations are observed in this configuration compared to a conventional on-axis imaging system: distortion and NA. These two parameters vary across the FoV differently compared to the conventional systems. However, dealing with these parameters required complicated Fresnel propagation integrals involving

propagation between tilted planes. Hence, to simplify the reconstruction, a small FoV approximation is incorporated. This small FoV approximation is same as the small FoV approximation present in the Fraunhofer model reconstruction method. Hence, conventional FPM reconstruction can be used in processing S-FPM data. This is experimentally validated on the data captured using the imaging systems in the SMA-FPM setup. The results provided an acceptable reconstruction quality, however, suffered from artefacts due to calibration errors. Self-calibration algorithm is proposed for correcting the calibration errors. This is left as future work along with SMA-FPM experimental validation.

Future work

The research presented in this work will be continued by Tomas Aidukas, a PhD student starting in Nov 2017. This student will be looking at the future aspects described below for the MA-FPM project. This student has also conducted a summer project in summer 2017 in our research group under my supervision. During this project an FPM setup was built under £100 using Raspberry Pi camera and computer. Within this project some of the calibration methods required for the Scheimpflug experimental setup calibration were also developed. These were successfully implemented to correct for severe field curvature effects in the mobile phone lenses and to correct for experimental setup assembly errors.

Experimental design:

There are few minor improvements can be performed to improve the robustness of the experimental setup. The lens array holder in the current setup has some extra barrel in front of the lens aperture as seen in Figure 6.1 (c) and can cause vignetting in the frequencies sampled. Hence a new lens array design is presented in (a) and (b). This design uses a dome-shaped design instead of the disk-shaped design in the previous setup. The disk-shaped design is easier to 3D print, hence provides better quality print. The dome-shaped design is challenging to 3D print due to the overhangs in the design. However, using a dome-shaped design would improve the experimental setup design. This is currently being tested in the next

iteration of the experimental setup being built. Another key update to the experimental design is the detector case holder. Currently, the detectors are held in the case using friction. When the detectors were not fit properly in these cases, the detector positions were observed to vibrate at low-frequencies (0.2 Hertz). This can be corrected by screwing the detectors into the cases instead of depending on the friction to hold them in position. Currently a commercial XYZ translation stage was used to translate the object. This will be replaced by 3D printed stage to further reduce the cost of the system.

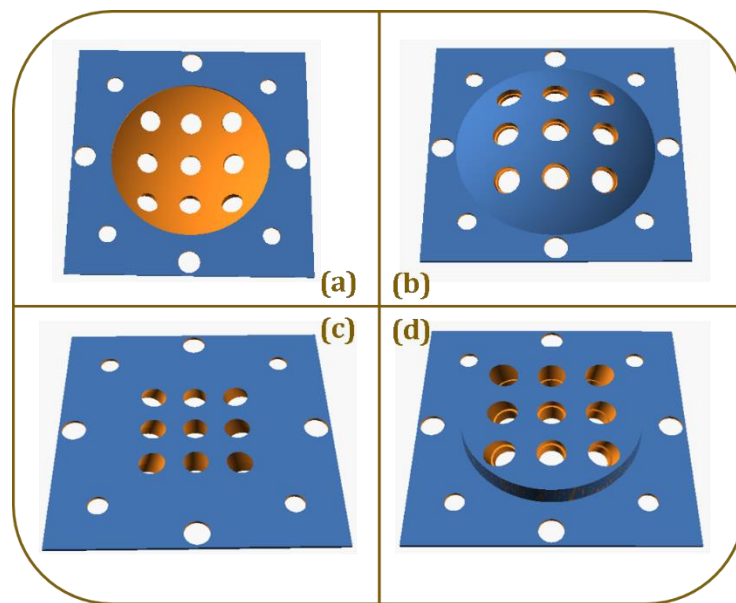


Figure 6.1 Lens array holder designs. (a) and (b) are front and back of the proposed new lens array design. (c) and (d) are front and back of the current lens array design.

S-FPM calibration:

As discussed in the S-FPM results section, the calibration errors in the experimental setup results in artefacts in the reconstructed image. Hence, self-calibration method [91,92] based calibration procedure needs to be developed. This was developed and implemented by us in the Raspberry Pi FPM setup [48]. Once calibration is achieved, the S-FPM reconstruction will be performed for the full FoV of the image.

SMA-FPM validation:

The SMA-FPM experimental setup is presented in this thesis but not validated experimentally. This will be achieved once robust calibration is achieved for S-FPM off-axis setups. To achieve this, the calibration procedure developed for MA-FPM in chapter 4 will be used. The only variation from the procedure described in chapter 4 is in the experimental setup. The image registration is performed to correct both translation and rotation values whereas in chapter 4 only translation values were corrected since that experimental setup did not have any rotational variations.

Other extensions to the proposed work include implementing LED multiplexing with the reported SMA-FPM experimental setup. To achieve this the LED array reported in [92] will be used instead of the planar LED used in the current setup. This LED enables LED multiplexing and has brighter LEDs, hence can provide much faster data acquisition time. This setup can be used to image fast growing cell cultures such as from human mammary epithelial cells [5]. Another application for the SMA-FPM setup would be diffraction tomography. In FPM diffraction tomography was reported using specialized forward models for the image formation process [64,66,109]. These forward models can be extended to the SMA-FPM setup to achieve 3D imaging.

To conclude, MA-FPM is a promising technique to achieve large SBTP systems. Implementing multiple imaging systems increases the complexity of these systems, however, calibration methods can be developed to address these problems. In this thesis the time required for the reconstruction process is not discussed since it was not relevant to the high-speed acquisition process. Currently it takes several minutes to process an individual dataset, however, GPUs can be used to accelerate the processing speed to achieve reconstruction times under few seconds. Real-space ptychography and FPM have been used to study cell cultures of cancer cells [5,150], but at low data acquisition speeds. MA-FPM is envisaged to be used in such applications where large SBTP images are required

to visualize sub-cellular processes and in digital pathology centres where several samples need to be imaged every day. The low-cost nature of the proposed design should also help in increasing the adaptation of this technique.

References

1. K. Guo, J. Liao, Z. Bian, X. Heng, and G. Zheng, "InstantScope: a low-cost whole slide imaging system with instant focal plane detection," *Biomed. Opt. Express* **6**, 3210 (2015).
2. F. B. Legesse, O. Chernavskaya, S. Heuke, T. Bocklitz, T. Meyer, J. Popp, and R. Heintzmann, "Seamless stitching of tile scan microscope images," *J. Microsc.* **258**, 223-232 (2015).
3. G. Zheng, R. Horstmeyer, and C. Yang, "Wide-field, high-resolution Fourier ptychographic microscopy," *Nat. Photonics* **7**, 739-745 (2013).
4. L. Tian, Z. Liu, L.-H. Yeh, M. Chen, J. Zhong, and L. Waller, "Computational illumination for high-speed in vitro Fourier ptychographic microscopy," arXiv (2015).
5. L. Tian, Z. Liu, L.-H. Yeh, M. Chen, J. Zhong, and L. Waller, "Computational illumination for high-speed in vitro Fourier ptychographic microscopy," *Optica* **2**, 904 (2015).
6. L. Tian, X. Li, K. Ramchandran, and L. Waller, "Multiplexed coded illumination for Fourier Ptychography with an LED array microscope," *Biomed. Opt. Express* **5**, 2376-89 (2014).
7. J. W. Goodman, *Introduction to Fourier Optics*, Second ed (1996).
8. "No Title," https://www.thorlabs.com/images/tabimages/TDI_System_A1-1000.jpg.
9. F. Balzarotti, Y. Eilers, K. C. Gwosch, A. H. Gynnå, V. Westphal, F. D. Stefani, J. Elf, and S. W. Hell, "Nanometer resolution imaging and tracking of fluorescent molecules with minimal photon fluxes," *Science* (80-.). **355**, 606 LP-612 (2017).
10. S. W. Hell and J. Wichman, "Breaking the diffraction resolution limit by stimulated emission: stimulated-emission-depletion fluorescence microscopy," *Opt. Lett.* **19**, 780-782 (1994).
11. M. J. Rust, M. Bates, and X. W. Zhuang, "Sub-diffraction-limit imaging by stochastic optical reconstruction microscopy (STORM)," *Nat Methods* **3**, 793-795 (2006).
12. S. T. Hess, T. P. K. Girirajan, and M. D. Mason, "Ultra-High Resolution Imaging by Fluorescence Photoactivation Localization Microscopy," *Biophys. J.* **91**, 4258-4272 (2006).
13. E. Betzig, G. H. Patterson, R. Sougrat, O. W. Lindwasser, S. Olenych, J. S. Bonifacino, M. W. Davidson, J. Lippincott-schwartz, and H. F. Hess, "Imaging Intracellular Fluorescent Proteins at Nanometer Resolution," *Science* (80-.). **313**, 1642-1646 (2006).
14. M. G. Gustafsson, "Surpassing the lateral resolution limit by a factor of two using structured illumination microscopy," *J. Microsc.* **198**, 82-87 (2000).
15. M. G. L. Gustafsson, "Nonlinear structured-illumination microscopy: wide-field fluorescence imaging with theoretically unlimited resolution," *Proc. Natl. Acad. Sci. U. S. A.* **102**, 13081-13086 (2005).
16. E. Mudry, K. Belkebir, J. Girard, J. Savatier, E. Le Moal, C. Nicoletti, M. Allain, and A. Sentenac, "Structured illumination microscopy using unknown speckle patterns," *Nat. Photonics* **6**, 312-315 (2012).
17. S. Dong, P. Nanda, R. Shiradkar, K. Guo, and G. Zheng, "High-resolution fluorescence

- imaging via pattern-illuminated Fourier ptychography," *Opt. Express* **22**, 20856-70 (2014).
18. L.-H. Yeh, L. Tian, and L. Waller, "Structured illumination microscopy with unknown patterns and a statistical prior," *Biomed. Opt. Express* **8**, 695-711 (2017).
 19. G. McConnell, J. Tragardh, R. Amor, J. Dempster, E. Reid, and W. B. Amos, "A novel optical microscope for imaging large embryos and tissue volumes with sub-cellular resolution throughout," *Elife* 1-15 (2016).
 20. G. Zheng, X. Ou, and C. Yang, "0.5 Gigapixel Microscopy Using a Flatbed Scanner," *Biomed. Opt. Express* **5**, 1-8 (2013).
 21. G. Carles, S. Chen, N. Bustin, J. Downing, D. McCall, A. Wood, and A. R. Harvey, "Multi-aperture foveated imaging," *Opt. Lett.* **41**, 1869 (2016).
 22. G. Carles, J. Downing, and A. R. Harvey, "Super-resolution imaging using a camera array," *Opt. Lett.* **39**, 1889-92 (2014).
 23. D. J. Brady and N. Hagen, "Multiscale lens design," *Opt. Express* **17**, 10659-10674 (2009).
 24. G. Carles, G. Muyo, N. Bustin, A. Wood, and A. R. Harvey, "Compact multi-aperture imaging with high angular resolution," *J. Opt. Soc. Am. A* **32**, 411-419 (2015).
 25. S. McCain, S. Feller, and D. J. Brady, "Gigapixel Television," in *Imaging and Applied Optics Congress 2016, OSA Technical Digest (Online) (Optical Society of America), Paper CTh3B.5* (2016).
 26. D. L. Marks, H. S. Son, J. Kim, and D. J. Brady, "Engineering a gigapixel monocentric multiscale camera," *Opt. Eng.* **51**, 83202-1 (2012).
 27. D. J. Brady, M. E. Gehm, R. A. Stack, D. L. Marks, D. S. Kittle, D. R. Golish, E. M. Vera, and S. D. Feller, "Multiscale gigapixel photography," *Nature* **486**, 386-389 (2012).
 28. A. B. Meinel, "Aperture synthesis using independent telescopes," *Appl. Opt.* **9**, 2501 (1970).
 29. A. E. Tippie, A. Kumar, and J. R. Fienup, "High-resolution synthetic-aperture digital holography with digital phase and pupil correction," *Opt. Express* **19**, 12027-12038 (2011).
 30. W. Luo, A. Greenbaum, Y. Zhang, and A. Ozcan, "Synthetic aperture-based on-chip microscopy," *Light Sci. Appl.* **4**, e261 (2015).
 31. I. Navruz, A. F. Coskun, J. Wong, S. Mohammad, D. Tseng, R. Nagi, S. Phillips, and A. Ozcan, "Smart-phone based computational microscopy using multi-frame contact imaging on a fiber-optic array," *Lab Chip* **13**, 4015 (2013).
 32. J. R. Fienup, "Reconstruction of an object from the modulus of its Fourier transform," *Opt. Lett.* **3**, 27-29 (1978).
 33. P. Konda, J. Taylor, and A. R. Harvey, "Multi-aperture Fourier Ptychography imaging in the near field," in *Imaging and Applied Optics 2015, OSA Technical Digest (Online) (Optical Society of America), Paper CM3E.5* (2015).
 34. H. M. L. Faulkner and J. M. Rodenburg, "Movable aperture lensless transmission microscopy: A novel phase retrieval algorithm," *Phys. Rev. Lett.* **93**, 23903-1 (2004).
 35. J. M. Rodenburg and H. M. L. Faulkner, "A phase retrieval algorithm for shifting illumination," *Appl. Phys. Lett.* **85**, 4795-4797 (2004).
 36. J. M. Rodenburg, A. C. Hurst, and A. G. Cullis, "Transmission microscopy without lenses for objects of unlimited size," *Ultramicroscopy* **107**, 227-231 (2007).
 37. A. M. Maiden and J. M. Rodenburg, "An improved ptychographical phase retrieval algorithm for diffractive imaging," *Ultramicroscopy* **109**, 1256-1262 (2009).
 38. A. M. Maiden, M. J. Humphry, and J. M. Rodenburg, "Ptychographic transmission microscopy in three dimensions using a multi-slice approach," *J. Opt. Soc. Am. A* **29**, 1606 (2012).

39. D. J. Vine, G. J. Williams, B. Abbey, M. A. Pfeifer, J. N. Clark, M. D. De Jonge, I. McNulty, A. G. Peele, and K. A. Nugent, "Ptychographic fresnel coherent diffractive imaging," *Phys. Rev. A - At. Mol. Opt. Phys.* **80**, 1-5 (2009).
40. M. D. Seaberg, B. Zhang, D. F. Gardner, E. R. Shanblatt, M. M. Murnane, H. C. Kapteyn, and D. E. Adams, "Tabletop nanometer extreme ultraviolet imaging in an extended reflection mode using coherent Fresnel ptychography," *Optica* **1**, 39 (2014).
41. J. M. Rodenburg, "Ptychography and related diffractive imaging methods," *Adv. Imaging Electron Phys.* **150**, 87-184 (2008).
42. J. R. Fienup, "Reconstruction of a complex-valued object from the modulus of its Fourier transform using a support constraint," *J. Opt. Soc. Am. A* **4**, 118-123 (1986).
43. J. R. Fienup, "Phase retrieval algorithms: a comparison," *Appl. Opt.* **21**, 2758-2769 (1982).
44. J. R. Fienup and C. C. Wackerman, "Phase-retrieval stagnation problems and solutions," *J. Opt. Soc. Am. A* **3**, 1897-1907 (1986).
45. M. A. Fiddy, B. J. Brames, and J. C. Dainty, "Enforcing irreducibility for phase retrieval in two dimensions," *Opt. Lett.* **8**, 96-8 (1983).
46. P. Sidorenko and O. Cohen, "Single-shot ptychography," *Optica* **3**, 9 (2016).
47. P. Thibault, M. Guizar-Sicairos, and A. Menzel, "Coherent imaging at the diffraction limit," *J. Synchrotron Radiat.* **21**, 1011-1018 (2014).
48. P. C. Konda, T. Aidukas, J. M. Taylor, and A. R. Harvey, "Miniature Fourier ptychography microscope using Raspberry Pi camera and hardware," in *Imaging and Applied Optics 2017 (3D, AIO, COSI, IS, MATH, pcAOP)* (2017), Vol. 2017.
49. R. Hegerl and W. Hoppe, "DYNAMIC THEORY OF CRYSTALLINE STRUCTURE ANALYSIS BY ELECTRON DIFFRACTION IN INHOMOGENEOUS PRIMARY WAVE FIELD," *Berichte Der Bunsen-Gesellschaft Fur Phys. Chemie* **74**, 1148 (1970).
50. W. Hoppe, "DIFFRACTION IN INHOMOGENEOUS PRIMARY WAVE FIELDS PRINCIPLE OF PHASE DETERMINATION FROM ELECTRON DIFFRACTION INTERFERENCE," *Acta Crystallogr. Sect. a-Crystal Phys. Diffr. Theor. Gen. Crystallogr.* **A25**, 495 (1969).
51. W. Hoppe and G. Strube, "DIFFRACTION IN INHOMOGENEOUS PRIMARY WAVE FIELDS .2. OPTICAL EXPERIMENTS FOR PHASE DETERMINATION OF LATTICE INTERFERENCES," *Acta Crystallogr. Sect. a-Crystal Phys. Diffr. Theor. Gen. Crystallogr.* **A25**, 502 (1969).
52. W. Hoppe, "DIFFRACTION IN INHOMOGENEOUS PRIMARY WAVE FIELDS AMPLITUDE AND PHASE DETERMINATION FOR NONPERIODIC OBJECTS," *Acta Crystallogr. Sect. a-Crystal Phys. Diffr. Theor. Gen. Crystallogr.* **A25**, 508 (1969).
53. W. Hoppe, "No Title," *Z. Naturforsch.* **26a**, 1155 (1971).
54. A. I. Kirkland, W. O. Saxton, K. L. Chau, K. Tsuno, and M. Kawasaki, "Super-resolution by aperture synthesis: tilt series reconstruction in CTEM," *Ultramicroscopy* **57**, 355-374 (1995).
55. S. J. Haigh, H. Sawada, and A. I. Kirkland, "Atomic Structure Imaging beyond Conventional Resolution Limits in the Transmission Electron Microscope," *Phys. Rev. Lett.* **103**, 16-19 (2009).
56. J. M. Cowley, "IMAGE CONTRAST in a TRANSMISSION SCANNING ELECTRON MICROSCOPE," *Appl. Phys. Lett.* **15**, 58-59 (1969).
57. J. Ruze, "Circular Aperture Synthesis," *IEEE Trans. Antennas Propag.* **12**, 691-694 (1964).
58. W. N. Brouw, "Aperture Synthesis BT - Image Processing Techniques in Astronomy: Proceedings of a Conference Held in Utrecht on March 25-27, 1975," in C. De Jager and H. Nieuwenhuijzen, eds. (Springer Netherlands, 1975), pp. 301-307.

59. A. H. Greenaway, "Optical aperture synthesis," *Meas. Sci. Technol.* **2**, 1 (1991).
60. M. Ryle, F. G. Smith, and B. Elsmore, "A Preliminary Survey of the Radio Stars in the Northern Hemisphere," *Mon. Not. R. Astron. Soc.* **110**, 508-523 (1950).
61. L. G. Shirley and G. R. Hallerman, "Nonconventional 3D Imaging Speckle Using Wavelength-Dependent Speckle," *Lincoln Lab. J.* **9**, 153-186 (1996).
62. K. Wicker and R. Heintzmann, "Resolving a misconception about structured illumination," *Nat. Photonics* **8**, 342-344 (2014).
63. S. Dong, R. Horstmeyer, R. Shiradkar, K. Guo, X. Ou, Z. Bian, H. Xin, and G. Zheng, "Aperture-scanning Fourier ptychography for 3D refocusing and super-resolution macroscopic imaging," *Opt. Express* **22**, 13586-99 (2014).
64. L. Tian and L. Waller, "3D intensity and phase imaging from light field measurements in an LED array microscope," *Optica* **2**, 104-111 (2015).
65. R. Horstmeyer and C. Yang, "Diffraction tomography with Fourier ptychography," 1-22 (2015).
66. P. Li, D. J. Batey, T. B. Edo, and J. M. Rodenburg, "Separation of three-dimensional scattering effects in tilt-series Fourier ptychography," *Ultramicroscopy* **158**, 1-7 (2015).
67. Y. Zhou, J. Wu, Z. Bian, J. Suo, G. Zheng, and Q. Dai, "Fourier ptychographic microscopy using wavelength multiplexing," *J. Biomed. Opt.* **22**, 66006 (2017).
68. S. Dong, R. Shiradkar, P. Nanda, and G. Zheng, "Spectral multiplexing and coherent-state decomposition in Fourier ptychographic imaging," *Biomed. Opt. Express* **5**, 1757-67 (2014).
69. D. J. Batey, D. Claus, and J. M. Rodenburg, "Information multiplexing in ptychography," *Ultramicroscopy* **138**, 13-21 (2014).
70. R. H. T. Bates and J. M. Rodenburg, "Sub-ångström transmission microscopy: A fourier transform algorithm for microdiffraction plane intensity information," *Ultramicroscopy* **31**, 303-307 (1989).
71. J. M. Rodenburg and R. H. T. Bates, "The Theory of Super-Resolution Electron Microscopy Via Wigner-Distribution Deconvolution," *Philos. Trans. R. Soc. A Math. Phys. Eng. Sci.* **339**, 521-553 (1992).
72. S. L. Friedman and J. M. Rodenburg, "Optical demonstration of a new principle of far-field microscopy," *J. Phys. D. Appl. Phys.* **25**, 147-154 (1992).
73. B. C. McCallum and J. M. Rodenburg, "Two-dimensional demonstration of Wigner phase-retrieval microscopy in the STEM configuration," *Ultramicroscopy* **45**, 371-380 (1992).
74. J. M. Rodenburg, B. C. McCallum, and P. D. Nellist, "Experimental tests on double-resolution coherent imaging via STEM," *Ultramicroscopy* **48**, 304-314 (1993).
75. H. N. Chapman, "Phase-retrieval X-ray microscopy by Wigner-distribution deconvolution," *Ultramicroscopy* **66**, 153-172 (1996).
76. M. Landauer, "Indirect Modes of Coherent Imaging in High-Resolution Electron Microscopy," University of Cambridge (1996).
77. G. De Villiers and E. R. Pike, *The Limits of Resolution*, Optics and Optoelectronics (CRC Press LLC, 2016).
78. L.-H. Yeh, L. Tian, Z. Liu, M. Chen, J. Zhong, and L. Waller, "Experimental robustness of Fourier Ptychographic phase retrieval algorithms," *Opt. Express* **23**, (2015).
79. L. Waller, "3D Phase Retrieval with Computational Illumination," in *Imaging and Applied Optics 2015*, OSA Technical Digest (Online) (Optical Society of America, 2015), p. CW4E.1.
80. F. Hübner, J. M. Rodenburg, A. M. Maiden, F. Sweeney, and P. A. Midgley, "Wave-front phase

- retrieval in transmission electron microscopy via ptychography," *Phys. Rev. B - Condens. Matter Mater. Phys.* **82**, (2010).
81. J. M. Rodenburg, A. C. Hurst, A. G. Cullis, B. R. Dobson, F. Pfeiffer, O. Bunk, C. David, K. Jefimovs, and I. Johnson, "Hard-X-ray lensless imaging of extended objects," *Phys. Rev. Lett.* **98**, (2007).
 82. L. Bian, J. Suo, G. Zheng, K. Guo, F. Chen, and Q. Dai, "Fourier ptychographic reconstruction using Wirtinger flow optimization," *Opt. Express* **23**, 4856 (2015).
 83. R. Horstmeyer, R. Y. Chen, X. Ou, B. Ames, J. A. Tropp, and C. Yang, "Solving ptychography with a convex relaxation," *New J. Phys.* **17**, 1-8 (2015).
 84. P. Thibault, M. Dierolf, A. Menzel, O. Bunk, C. David, and F. Pfeiffer, "High-resolution scanning X-ray diffraction microscopy," *Science* (80-.). **321**, 379-382 (2008).
 85. C. Zuo, J. Sun, and Q. Chen, "Adaptive step-size strategy for noise-robust Fourier ptychographic microscopy," *Opt. Express* **24**, 4960-4972 (2016).
 86. P. Thibault and A. Menzel, "Reconstructing state mixtures from diffraction measurements," *Nature* **494**, 68-71 (2013).
 87. X. Ou, G. Zheng, and C. Yang, "Embedded pupil function recovery for Fourier ptychographic microscopy," *Opt. Express* **22**, 4960-72 (2014).
 88. Z. Bian, S. Dong, and G. Zheng, "Adaptive system correction for robust Fourier ptychographic imaging," *Opt. Express* **21**, 32400-10 (2013).
 89. J. Sun, Q. Chen, Y. Zhang, and C. Zuo, "Efficient positional misalignment correction method for Fourier ptychographic microscopy," *Biomed. Opt. Express* **7**, 1336 (2016).
 90. A. M. Maiden, M. J. Humphry, M. C. Sarahan, B. Kraus, and J. M. Rodenburg, "An annealing algorithm to correct positioning errors in ptychography," *Ultramicroscopy* **120**, 64-72 (2012).
 91. R. Eckert, L. Tian, and L. Waller, "Algorithmic self-calibration of illumination angles in Fourier ptychographic microscopy," in *Imaging and Applied Optics 2016, OSA Technical Digest (Online) (Optical Society of America, 2016), Paper CT2D.3.* (2016), pp. 3-5.
 92. Z. F. Phillips, R. Eckert, and L. Waller, "Quasi-Dome : A Self-Calibrated High-NA LED Illuminator for Fourier Ptychography," in *Imaging and Applied Optics 2017 (3D, AIO, COSI, IS, MATH, pcAOP)* (2017), Vol. 2017, pp. 2016-2018.
 93. J. Sun, C. Zuo, L. Zhang, and Q. Chen, "Resolution-enhanced Fourier ptychographic microscopy based on high-numerical-aperture illuminations," *Sci. Rep.* 1-11 (2017).
 94. S. Dong, Z. Bian, R. Shiradkar, and G. Zheng, "Sparsely sampled Fourier ptychography," *Opt. Express* **22**, 5455-64 (2014).
 95. O. Bunk, M. Dierolf, S. Kynde, I. Johnson, O. Marti, and F. Pfeiffer, "Influence of the overlap parameter on the convergence of the ptychographical iterative engine," *Ultramicroscopy* **108**, 481-487 (2008).
 96. X. Ou, R. Horstmeyer, G. Zheng, and C. Yang, "High numerical aperture Fourier ptychography : principle, implementation and characterization," *Opt. Express* **23**, 5473-5480 (2015).
 97. R. John and S. A. Boppart, "Estimation of longitudinal resolution in optical coherence imaging," *Appl. Opt.* **41**, 5256-5262 (2002).
 98. L.-H. Yeh, L. Tian, Z. Liu, M. Chen, J. Zhong, and L. Waller, "Experimental robustness of Fourier Ptychographic phase retrieval algorithms," *Imaging Appl. Opt.* 2015 CW4E.2 (2015).
 99. Y. Fan, J. Sun, Q. Chen, M. Wang, and C. Zuo, "Adaptive denoising method for Fourier ptychographic microscopy," *Opt. Commun.* (2017).

100. P. C. Konda, J. M. Taylor, and A. R. Harvey, "High-resolution microscopy with low-resolution objectives: correcting phase aberrations in Fourier ptychography," in *Proc. SPIE 9630, Optical Systems Design 2015: Computational Optics, 96300X* (2015).
101. K. Guo, S. Dong, P. Nanda, and G. Zheng, "Optimization of sampling pattern and the design of Fourier ptychographic illuminator," *Opt. Express* **23**, 6171-6180 (2014).
102. K. Guo, Z. Bian, S. Dong, P. Nanda, Y. M. Wang, and G. Zheng, "Microscopy illumination engineering using a low-cost liquid crystal display," *Biomed. Opt. Express* **6**, 574-579 (2015).
103. C. Kuang, Y. Ma, R. Zhou, J. Lee, G. Barbastathis, R. R. Dasari, Z. Yaqoob, and P. T. C. So, "Digital micromirror device-based laser-illumination Fourier ptychographic microscopy," *Opt. Express* **23**, 26999 (2015).
104. J. Chung, H. Lu, X. Ou, H. Zhou, and C. Yang, "Wide-field Fourier ptychographic microscopy using laser illumination source," arXiv (2016).
105. S. Pacheco, G. Zheng, and R. Liang, "Reflective Fourier ptychography," *J. Biomed. Opt.* **21**, (2016).
106. K. Guo, S. Dong, and G. Zheng, "Fourier Ptychography for Brightfield, Phase, Darkfield, Reflective, Multi-Slice, and Fluorescence Imaging," *IEEE J. Sel. Top. Quantam Electron.* **22**, 1-12 (2016).
107. S. Pacheco, B. Salahieh, T. Milster, J. J. Rodriguez, and R. Liang, "Transfer function analysis in epi-illumination Fourier ptychography," *Opt. Lett.* **40**, 5343 (2015).
108. J. Chung, R. Horstmeyer, and C. Yang, "FOURIER PTYCHOGRAPHIC RETINAL IMAGING METHODS AND SYSTEMS," U.S. patent US 2017/0273551 A1 (2017).
109. R. Horstmeyer and C. Yang, "Diffraction tomography with Fourier ptychography," *Optica* **3**, 1-22 (2015).
110. J. Holloway, M. S. Asif, M. K. Sharma, N. Matsuda, R. Horstmeyer, O. Cossairt, and A. Veeraraghavan, "Toward Long Distance, Sub-diffraction Imaging Using Coherent Camera Arrays," Arxiv doi:10.1109/TCl.2016.2557067 (2015).
111. Á. D. Rodríguez, Y. Jauregui-sánchez, P. Clemente, M. Mohammad, Seyed Khamoushi, S. H. Tavassoli, E. Tajahuerce, and J. Lancis, "Improving resolution in single-pixel microscopy by using Fourier ptychography," in *SPIE-OSA* (2017), Vol. 10414.
112. D. B. Phillips, M.-J. Sun, J. M. Taylor, M. P. Edgar, S. M. Barnett, G. G. Gibson, and M. J. Padgett, "Adaptive foveated single-pixel imaging with dynamic super-sampling," 1-11 (2016).
113. Z.-L. Xie, H.-T. Ma, B. Qi, G. Ren, Y.-F. Tan, B. He, H.-L. Zeng, and C. Jiang, "Aperture-Scanning Fourier Ptychographic Encoding with Phase Modulation," *Chinese Phys. Lett.* **32**, 124203 (2015).
114. "Ronchi ruling," https://en.wikipedia.org/wiki/Ronchi_ruling.
115. E. Hecht, *Optics* (2001), Vol. 1.
116. "Square wave," https://en.wikipedia.org/wiki/Square_wave.
117. S. Mezouari and A. Harvey, "Validity of Fresnel and Fraunhofer approximations in scalar diffraction," *J. Opt. A Pure Appl. Opt.* **5**, S86-S91 (2003).
118. P. Picart and J. Li, *Digital Holography* (John Wiley & Sons, 2013).
119. K. Matsushima, "Shifted angular spectrum method for off-axis numerical propagation," *Opt. Express* **18**, 18453-63 (2010).
120. S. M. Schultz, "Using MATLAB to help teach Fourier optics," *Proc. SPIE* **6695**, 66950I-66950I-10 (2007).

121. S. Dong, K. Guo, P. Nanda, R. Shiradkar, and G. Zheng, "FPscope: a field-portable high-resolution microscope using a cellphone lens," *Biomed. Opt. Express* **5**, 3305 (2014).
122. "Nikon 0.15NA objective," <https://www.edmundoptics.co.uk/microscopy/infinity-corrected-objectives/5x-nikon-cfi60-tu-plan-epi-infinity-corrected-obj/>.
123. L. G. Brown, "A survey of image registration techniques," *ACM Comput. Surv.* **24**, 325-376 (1992).
124. J. B. Maintz and M. A. Viergever, "A survey of medical image registration," *Med. Image Anal.* **2**, 1-36 (1998).
125. B. Zitová and J. Flusser, "Image registration methods: A survey," *Image Vis. Comput.* **21**, 977-1000 (2003).
126. "Edmund optics Achromatic lens 9mm diameter, 36mm focal length," <https://www.edmundoptics.co.uk/optics/optical-lenses/achromatic-lenses/9mm-dia.-x-36mm-fl-vis-0deg-coated-achromatic-lens/>.
127. "1951 USAF resolution test chart," https://en.wikipedia.org/wiki/1951_USAF_resolution_test_chart.
128. Z. F. Phillips, M. V. D'Ambrosio, L. Tian, J. J. Rulison, H. S. Patel, N. Sadras, A. V. Gande, N. A. Switz, D. A. Fletcher, and L. Waller, "Multi-contrast imaging and digital refocusing on a mobile microscope with a domed LED array," *PLoS One* **10**, 1-13 (2015).
129. W. J. Smith, *Modern Optical Engineering* (2000).
130. "Scheimpflug principle," https://en.wikipedia.org/wiki/Scheimpflug_principle.
131. T. Scheimpflug, "Improved Method and apparatus for the Systematic Alteration or Distortion of Plane Pictures and Images by Means of Lenses and Mirrors for Photography and for other purposes," **52** (1904).
132. A. K. Prasad, "Stereoscopic particle image velocimetry," *Exp. Fluids* **29**, 130-116 (2000).
133. W. Zang and A. K. Prasad, "Performance evaluation of a Scheimpflug stereocamera for particle image velocimetry," *Appl. Opt.* **36**, 8738 (1997).
134. T. Piv, "A Scheimpflug Camera Model for Stereoscopic," (2015).
135. "Corneal Pachymetry," https://en.wikipedia.org/wiki/Corneal_pachymetry.
136. Y. Barkana, Y. Gerber, U. Elbaz, S. Schwartz, G. Ken-Dror, I. Avni, and D. Zadok, "Central corneal thickness measurement with the Pentacam Scheimpflug system, optical low-coherence reflectometry pachymeter, and ultrasound pachymetry," *J. Cataract Refract. Surg.* **31**, 1729-1735 (2005).
137. T. Koller, H. P. Iseli, F. Hafezi, P. Vinciguerra, and T. Seiler, "Scheimpflug Imaging of Corneas After Collagen Cross-Linking," *Cornea* **28**, 510-515 (2009).
138. R. Jain and S. Grewal, "Pentacam: Principle and Clinical Applications," *Curr. J. Glaucoma Pract. with DVD* **20-32** (2009).
139. P. C. Konda, J. M. Taylor, and A. R. Harvey, "Scheimpflug multi-aperture Fourier ptychography: coherent computational microscope with gigapixels / s data acquisition rates using 3D printed components," in *Proc. SPIE 10076, High-Speed Biomedical Imaging and Spectroscopy: Toward Big Data Instrumentation and Management II, 100760R (February 22, 2017)* (n.d.).
140. J. Carpentier, "Improvements in Enlarging or like Cameras," (1901).
141. J. P. Sharkey, D. C. W. Foo, A. Kabla, J. J. Baumberg, and R. W. Bowman, "A one-piece 3D printed flexure translation stage for open-source microscopy," *Rev. Sci. Instrum.* **87**, (2016).

142. "Thorlabs 3-axis kinematic stages," https://www.thorlabs.com/newgrouppage9.cfm?objectgroup_id=185&pn=KC1/M.
143. J. Chung, H. Lu, X. Ou, H. Zhou, and C. Yang, "Wide-field Fourier ptychographic microscopy using laser illumination source," *Biomed. Opt. Express* **7**, 4787-4802 (2016).
144. "OpenSCAD software," <http://www.openscad.org/>.
145. "Cura 3D printing software," <https://ultimaker.com/en/products/ultimaker-cura>.
146. "Ultimaker printing tips," <https://ultimaker.com/en/resources/tips-tricks>.
147. Q. Mei, J. Gao, H. Lin, Y. Chen, H. Yunbo, W. Wang, G. Zhang, and X. Chen, "Structure light telecentric stereoscopic vision 3D measurement system based on Scheimpflug condition," *Opt. Lasers Eng.* **86**, 83-91 (2016).
148. "Scheimpflug DoF image source," <https://en.wikipedia.org/wiki/File:ScheimpflugDoF.png>.
149. L. Bian, G. Zheng, K. Guo, J. Suo, C. Yang, F. Chen, and Q. Dai, "Motion-corrected Fourier ptychography," *Biomed. Opt. Express* **7**, (2016).
150. R. Suman, G. Smith, K. E. A. Hazel, R. Kasprowicz, M. Coles, P. O'Toole, and S. Chawla, "Label-free imaging to study phenotypic behavioural traits of cells in complex co-cultures," *Sci. Rep.* **6**, 1-6 (2016).